

Efficient sub-Doppler Transverse Laser Cooling of an Indium Atomic Beam

Dissertation

angefertigt im

Institut für Angewandte Physik

vorgelegt der

Mathematisch-Naturwissenschaftlichen Fakultät

der

Rheinischen Friedrich-Wilhelms-Universität Bonn

von

Jae-Ihn Kim

aus

Icheon, Südkorea

Bonn 2009



Angefertigt mit Genehmigung der Mathematisch-Naturwissenschaftlichen Fakultät

der Rheinischen Friedrich-Wilhelms-Universität Bonn

1. Referent: Prof. Dr. Dieter Meschede
2. Referent: Prof. Dr. Karl Maier

Tag der Promotion: 23.07.2009

Abstract

Laser cooled atomic gases and atomic beams are widely studied samples in experimental research in atomic and optical physics. For the application of ultra cold gases as model systems for e.g. quantum many particle systems, the atomic species is not very important. Thus this field is dominated by alkaline, earthalkaline elements which are easily accessible with conventional laser sources and have convenient closed cooling transition. On the other hand, laser cooled atoms may also be interesting for technological applications, for instance for the creation of novel materials by atomic nanofabrication (ANF). There it will be important to use technologically relevant materials. As an example, using group III atoms of the periodical table in ANF may open a route to generate fully 3D structured composite materials. The minimal requirement in such an ANF experiment is the collimation of an atomic beam which is accessible by one dimensional laser cooling.

In this dissertation, I describe transverse laser cooling of an Indium atomic beam. For efficient laser cooling on a cycling transition, I have built a tunable, continuous-wave coherent ultraviolet source at 326 nm based on frequency tripling. For this purpose, two independent high power Yb-doped fiber amplifiers for the generation of the fundamental radiation at $\lambda_{\omega} = 977$ nm have been constructed. I have observed sub-Doppler transverse laser cooling of an Indium atomic beam on a cycling transition of In by introducing a polarization gradient in the linear-perpendicular-linear configuration. The transverse velocity spread of a laser-cooled In atomic beam at full width at half maximum was achieved to be 13.5 ± 3.8 cm/s yielding a full divergence of only 0.48 ± 0.13 mrad. In addition, nonlinear spectroscopy of a 3-level, Λ -type level system driven by a pump and a probe beam has been investigated in order to understand the absorption line shapes used as a frequency reference in a previous two-color spectroscopy experiment. For the analysis of this atomic system, I have applied a density matrix theory providing an excellent basis for understanding the observed line shapes.

Publications in the part of this thesis:

1. J. I. KIM AND D. MESCHEDE, *Continuous-wave coherent ultraviolet source at 326 nm based on frequency tripling of fiber amplifiers*, Opt. Express **16**, 10803, (2008)
2. J. I. KIM, D. HAUBRICH, B. KLÖTER, AND D. MESCHEDE, *Non-linear Spectroscopy with Indium Vapor Cells*, submitted to Phys. Rev. A for publication (2009)
3. J. I. KIM, D. HAUBRICH, AND D. MESCHEDE, *Efficient sub-Doppler laser cooling of an Indium atomic beam*, submitted to Opt. Express for publication (2009)

Contents

1	Introduction	1
2	Interaction between Indium atoms and light fields	3
2.1	Indium	3
2.2	Density matrix equation	4
2.3	Laser cooling	7
2.4	Atom lens	10
3	Non-linear spectroscopy with Indium vapor cells	13
3.1	Saturation spectroscopy in blue transitions	13
3.2	Saturation spectroscopy in violet transitions	15
3.3	Spectroscopy of In with a hollow cathode lamp	23
3.4	Conclusion	28
4	A UV laser source based on fiber amplifiers	29
4.1	Fiber light source	29
4.1.1	Introduction	29
4.1.2	Yb-doped double clad fiber	30
4.1.3	Theoretical model	34
4.1.4	Fiber amplifier operating at 977 nm	35
4.2	Nonlinear frequency conversion	39
4.2.1	Theory on nonlinear optics	40
4.2.2	Nonlinear crystals for frequency upconversions	45
4.2.3	Second harmonic generation in external cavities	46
4.2.4	Sum frequency generation in an external cavity	50
4.3	Third harmonic generation in a doubly resonant cavity	52
4.3.1	Linear spectroscopy of the $5P_{3/2} \rightarrow 5D_{5/2}$ transition of Indium in a hollow cathode lamp	53
4.4	Conclusion	54
5	Efficient laser cooling of an Indium atomic beam	57
5.1	Experimental apparatus	57
5.2	Efficient sub-Doppler laser cooling	61
5.3	Calculation of the average force by polarization gradient for Indium	66
5.4	Conclusions and further improvements	68
6	Summary and outlook	71
A	Matrix elements	73
B	Saturation intensity	79

C Building a fiber amplifier

81

References

83

List of Figures

1.1	Basic concept of ANF.	1
2.1	Energy level scheme of ^{115}In	4
2.2	Theoretical level scheme of Indium as 6 levels. The states $ 1\rangle$, $ 2\rangle$, $ 3\rangle$, $ 4\rangle$, $ 5\rangle$, $ 6\rangle$ are corresponding to $ 5^2P_{1/2}, F = 4\rangle$, $ 5^2P_{1/2}, F = 5\rangle$, $ 5^2P_{3/2}, F = 4\rangle$, $ 5^2P_{3/2}, F = 5\rangle$, $ 5^2P_{3/2}, F = 6\rangle$, $ 6^2S_{1/2}, F = 5\rangle$ states. Ω_{ij} is the Rabi frequency.	5
2.3	(a) Concept of Doppler cooling. The counter propagating red-detuned laser beams interact with an atom moving to the left with a velocity v . (b) Calculated Doppler force using Eq. (2.17) and Eq. (2.18). The solid line for F_{OM} , the dotted and dot-dashed line for F_{SP}^+ and F_{SP}^- , respectively, and the dashed line for $F_{\text{OM}}^{\text{AP}}$. $\Omega = 2 \gamma$ and $\delta = 0.5 \gamma$	8
2.4	Sisyphus cooling mechanism in the lin \perp lin configuration.	9
2.5	Atoms in a dipole potential. Two atoms are traveling through one period of a dipole potential in z direction formed by a standing wave along the x direction. Due to the dipole force exerted along the transverse direction, atoms are focused to the focal point.	10
2.6	(a) The calculated trajectories of a perfectly (upper trace) and a partially (lower trace) collimated Indium atomic beam in an atom lens. The divergence of the partially collimated atomic beam is set to be the experimentally achieved value, 0.48 mrad. (b) The atomic flux along the x -axis for the ideally laser-cooled (upper profile) and the partially laser-cooled (lower profile) In atoms at the focal point. The full-width at half maxima (FWHMs) of the widths of each cases are calculated to be 3 nm and 45 nm. The parameters used in the simulation are $N_{\text{atom}} = 20000$, $I_{\text{sat}} = 10 s_0$, and $\delta = 10 \Gamma$	11
3.1	(a) Energy level scheme of ^{115}In . (b) Experimental setup for two color spectroscopy. The frequency of the pump laser at 410 nm is locked to the $4 \rightarrow 5$ transition. The frequency of the probe light at 451 nm is scanned around the blue transitions. DM: dichroic mirror; PD: photodiode; IF: interference filter.	13

3.2	(a) Lock-in signal. All hyperfine lines are well resolved. The powers (intensities) of the probe and pump beams are $645 \mu\text{W}$ (48 mW/cm^2) and $241 \mu\text{W}$ (18 mW/cm^2), respectively. (b) The magnification of the lock-in signal near to $6 \rightarrow 5$ transition. Contrary to the expectation, the FWHM of the observed spectrum is measured to be 580 MHz , far beyond the natural linewidth 25 MHz	14
3.3	Experimental setup for electromagnetically induced transparency (EIT) experiment. HWP: $\lambda/2$ plate; PBS: polarization beam splitter; PD: photo diode; LIA: lock-in amplifier; ASC: all sapphire cell.	15
3.4	(a) Absorption spectra of the probe beam with (solid line) and without (dashed line) the pump beam tuned to the center of the Doppler broadened spectrum. The slanted intensity is due to diode laser power variation. (b) Difference (solid line) of the two spectra from (a) compared with the directly measured absorption signal demodulated by a lock-in amplifier (dotted line). 16	16
3.5	Simplified energy level scheme of Indium with pump and probe transitions; γ_i , effective decay rate of the ground states; Γ, Γ_i , total and partial decay rate of the excited state; Ω_i , Rabi frequencies.	16
3.6	Perturbation chains to order $(\Omega_1\Omega_2)^2$ [30]. The stepwise (SW) contribution contains the intermediate population. The two quanta (TQ) terms involve the coherence between the intermediate and ground state of the probe transition.	18
3.7	(a) A typical EIT signal in a Rb vapor cell [31]. (b) Simulation result. Black and red curves correspond to the probe absorption with (black) and without (red) the pump field. In this calculation, the fourth term in Eq. (3.6) is not subtracted because no LIA was involved to their experiment.	19
3.8	The calculated probe beam absorption spectrum with (solid line) and without pump beam (dashed line). Also, the contributions of the coherent two-photon processes (TQ, dashed-dotted lines) and the stepwise contribution (SW, dotted line) are shown.	20
3.9	Theoretical EIT spectra at various coupling intensities.	21
3.10	The FWHM of SW as a function of the Rabi frequency of the pump beam. The data are fitted (solid line) by Eq. (3.9) yielding $\gamma = 1.6(0.1) \times 10^{-3}\Gamma$. The dotted line is the FWHM deduced by $s_{\text{eff}}^{\text{RE}}$ in a rate equation model for the same γ	21
3.11	The effective saturation parameter deduced by the density matrix model (solid line) and the rate equation model (dotted line). See also Fig. 3.10.	22
3.12	Schematic drawing of the hollow cathode lamp. The cathode is made of pure Indium which is inserted into a crucible made of nonconducting ceramic (dark grey). The Indium pool is grounded by a copper inlet (light grey) at the bottom of the crucible. The crucible has a length of 30 mm and a clearance of 5 mm above the Indium pool.	24

3.13	Setup for spectroscopy with the HCL. The incoming laser beam is split in half by a polarising beam splitter cube (PBSC) and guided through the hollow cathode lamp (HCL). The pump beam is circular polarized and can be amplitude modulated with a chopper wheel. The polarisation of the probe beam behind the HCL is analyzed with photodiodes PD1 and PD2 and demodulated with a lock-in amplifier. An interference filter (IF) blocks light caused by the discharge.	25
3.14	HCL: Doppler broadened transmission spectrum of the 451 nm probe laser for the $5P_{3/2}, F'' = 6, 5 \rightarrow 6S_{1/2}, F' = 5$ transitions. Discharge current is 40 mA.	25
3.15	Narrow line width signal obtained by polarization spectroscopy. The small dispersive signal is the $F'' = 6 \rightarrow F' = 5$ transition of ^{113}In	26
3.16	(a) The observed dispersive signal for polarization spectroscopy. The width of the peak-to-peak in the dispersive signals for $4 \rightarrow 5$ and $5 \rightarrow 4$ transitions is measured to be 70 MHz. (b) The transmission signal at 410 nm for saturation spectroscopy with an ASC [26].	27
3.17	(a) The inferred temperature and (b) the In vapor density as a function of discharge current. The discharge is not stable below 20 mA. Temperature and density differ slightly because the density is a function of not only the measured width, $\Delta\nu$, but also of the transmission, I/I_0	28
4.1	Schematic of a double-clad fiber amplifier. A multi-mode pump beam and a single mode seed beam are combined by a dichroic mirror, and the pair of pump and seed beam is coupled to the multi-mode inner cladding ($\phi \sim 10^2 \mu\text{m}$) and the single mode core ($\phi \sim \mu\text{m}$), respectively. The rare-earth ions doped in the core are pumped by the pump beam, and the seed beam is amplified through the stimulated emission process. The amplified seed beam is out-coupled by a lens.	30
4.2	The energy level diagram of Yb^{3+} in silica [39]	31
4.3	Emission (dotted line) and absorption (solid line) cross sections of Yb^{3+} in a germanosilicate glass [40]. The technical difficulty in a Yb-doped double cladding fiber (YDCF) source operating at 977 nm results from the fact that the absorption and the emission cross-sections are maximum at 977 nm.	32
4.4	The cross-section of the YDCF manufactured by Crystal Fibre. The core diameter is $6 \mu\text{m}$ while the multi-mode inner cladding has a diameter of $27 \mu\text{m}$. The main difference between this fiber and other conventional double cladding fibers is the small diameter of the inner cladding allowing a high overlap factor. For the efficient coupling of a pump beam, the numerical aperture is enhanced up to 0.55 by air holes around the inner cladding.	33
4.5	The microscopic pictures of Yb-doped jacketed air-clad fiber (YJACF) manufactured by Optoelectronics Research Center at the University of Southampton.	34

4.6	Experimental setup. Our system uses a diode laser system (ECDL), two fiber amplifiers (FA) and two external cavities (EC) for upconversion, $\lambda_\omega \rightarrow \{\lambda_\omega, \lambda_{2\omega}\} \rightarrow \lambda_{3\omega}$. ECDL: external cavity diode laser; EC: external cavity; YDCF: Yb-doped double clad fiber; HC: Hänsch-Couillaud method; OI: optical isolator; DM: dichroic mirror; M: mirror; CL: cylindrical lens; ML: mode-matching lens; IF: interference filter; PZT: piezo-electric transducer; BS: beam splitter; P: polarizer; QP: quartz plate.	36
4.7	Experimental output powers of FA1 (rectangles) and FA2 (circles) at 977 nm as a function of the launched pump power at ~ 920 nm. The solid lines show the theoretical output powers.	37
4.8	(a) The spectrum of the seed laser (ECDL) and the FA operating at full power. Suppression of ASE is more than 33 dB below the carriers as measured with an optical spectrum analyzer. (b) The beating signal between seed laser and FA operating at full power. 3 dB bandwidth is 18 kHz.	38
4.9	Long term power stability of a YDCFA. After a slight adjustment of the alignment at ~ 2 hours, the power of the fiber amplifier becomes stable because the mechanical system enters the thermal equilibrium. In the equilibrium region, the instability of the output power is measured to be $\pm 0.5\%$ of the averaged power.	38
4.10	A Lorentz oscillator in an anharmonic potential. $P(t)$ is the induced polarization which exhibits nonlinear response to the driving field, $E(t)$	39
4.11	Concept of nonlinear frequency conversions.	40
4.12	Gaussian beam in a nonlinear crystal. The fundamental wave (red trace) generates the second harmonic beam (blue trace). Due to the walk-off, the propagation of the blue and the red beam is not corresponding. L_c : the length of a nonlinear crystal; z_0 : Rayleigh length; b : confocal parameter; w_0 : beam waist in the crystal; ρ : walk-off angle; f_c : focal length.	43
4.13	Calculated Boyd-Kleinmann factors depending on various double refraction parameters.	44
4.14	The calculated optimum focusing parameter as a function of the double refraction parameter.	45
4.15	Cavity geometry used in the calculation of ABCD matrix. Two waists exist, one (w_{01}) is between the two curved mirrors, another (w_{02}) is between the two flat mirrors.	47
4.16	Waists of the cavities including a BIBO, a Brewster cut LBO, and a KNbO ₃ crystal.	48
4.17	Second harmonic power from the cavities including (a) a BIBO and (b) a Brewster cut LBO as a function of the input power at λ_ω	50
4.18	The beam profiles of the blue beam from (a) BIBO, (b) Brewster cut LBO, (d) KNbO ₃ cavities and (c) the beam profile of the infrared beam from the astigmatism-compensated cavity. The elongated shape in the blue beam profile results from walk-off. In the profile (c), the astigmatism for the infrared light is substantially suppressed.	51

4.19	Experimental (rectangles) and theoretical (solid line) third harmonic power at 325 nm as a function of the input power at 977 nm. Blue light power at 488 nm is fixed at 120 mW.	53
4.20	Experimental setup for the linear absorption spectroscopy of Indium using UV light at λ_{cool} . The dotted lines indicate the electrical connections.	54
4.21	An example of the absorption of the UV beam at $\lambda_{3\omega}$	54
4.22	(a) An example of fitted spectra. (b) The deduced temperature of the HCL as a function of the applied current.	55
5.1	An oven for the generation of an Indium atomic beam.	58
5.2	Schematics of the vacuum system.	59
5.3	Images of the atomic beam and their integrated transverse profile (a) in the cooling and (b) the probe region. The FWHMs of the profile of the cooling and the probe region are measured to be 0.57 ± 0.01 and 2.36 mm, respectively.	60
5.4	Schematic of the experimental setup. The atoms are optically pumped to the $^2P_{3/2}$ levels by two violet lasers at λ_{pump} in the pumping region. In the cooling region, UV light at λ_{cool} is applied with a polarization gradient configuration (lin \perp lin) for laser cooling. The spatial distribution of the atomic flux density is measured by exciting the atoms at λ_{probe} and imaging the fluorescence distribution at λ_{pump} in the probe region.	61
5.5	(a) Solid line: Fluorescence spectrum of the In $^2P_{3/2} \rightarrow ^2D_{5/2}$ transitions induced by the UV laser at λ_{cool} . Dotted line: Doppler limited absorption spectrum of a hollow cathode lamp. The frequency of the laser is calibrated by the separation between the $6 \rightarrow 5$ and the $6 \rightarrow 7$ transitions (1948 MHz). The FWHM of the peak of the $6 \rightarrow 7$ transition is 44 MHz. (b) Theoretical spectrum indicating position and oscillator strengths of hyperfine transitions. In the observed spectrum, optical cycling leads to strong enhancement on the closed $6 \rightarrow 7$ transition.	62
5.6	(a) Fluorescence peaks of the $6 \rightarrow 7$ transition depending on the optical pumping scheme. The green line is the ramp signal. (b) Time evolution of the population of $5P_{3/2}, F = 6$ with the various pumping scheme.	63
5.7	The images (a) and integrated transverse profiles (b) of the atomic beam in the probe region with and without the pushing beam at λ_{cool} . The displacement of the atomic beam due to the pushing effect is measured to be 1.8 mm which is corresponding to the transverse velocity change of $152 v_T$. 64	
5.8	Integrated transverse profiles of the atomic beam in the probe region: (solid line) cooling with the lin \perp lin polarization gradient ($\Delta \sim -\Gamma$), (dotted line) no laser cooling, (dashed line) heating with lin \perp lin polarization gradient ($\Delta \sim +\Gamma$). Insets: Images of a cooled (left) and a heated (right) In atomic beam.	65

5.9	(a) The time evolution of the ground state populations, $\rho(g_{-6})(t)$ (black), $\rho(g_6)(t)$ (red), and $\rho(g_{-6})(t) - \rho(g_6)(t) = \Delta\rho(g_{-6}, g_6)(t)$ (blue). (b) The time evolution of the reactive force in the unit of $\hbar k\Gamma$. The parameters used in the calculation are $\Omega_0 = 1.5 \Gamma$ ($s = 4.5$), $\delta = -0.5 \Gamma$. The velocity is selected to be $0.0015 \Gamma/k = 1 \text{ cm/s}$	67
5.10	The average force for Indium in the lin \perp lin configuration. The parameters used in the calculation are $\Omega_0 = 1.5 \Gamma$ ($s = 4.5$), $\delta = -0.5 \Gamma$	68
5.11	The calculated transverse profile of a cooled (black solid line) and an uncooled (red dotted line) Indium atomic beam. The fraction of the laser-cooled atoms is calculated to be 5 %. The parameters used in the calculation are $\Omega_0 = 1.5 \Gamma$ ($s = 4.5$), $\delta = -0.5 \Gamma$ and $L_{\text{int}} = 3 \text{ mm}$	69
5.12	The calculated transverse profile of a cooled (black solid line) and an uncooled (red dotted line) Indium atomic beam in the improved case. The fraction of the laser-cooled atoms is calculated to be 32 %. The parameters used in the calculation are $\Omega_0 = 1.5 \Gamma$ ($s = 4.5$), $\delta = -0.5 \Gamma$ and $L_{\text{int}} = 10 \text{ mm}$	69
6.1	Ultimate goal of ANF experiment: Co-deposition of Indium with other elements, e.g. Al or As for structured doping.	72
A.1	The Clebsch-Gordan coefficients of a cycling transition of Indium at 326 nm.	78
B.1	A multi-level, Λ -type level scheme of ^{115}In for the calculation of saturation intensities.	79
B.2	The population of the excited state as a function of the saturation intensity for a two level system (black) and for Indium (red), respectively.	80
C.1	A schematic of a fiber amplifier.	81
C.2	A picture of the ECDL for the seed beam at λ_ω	81
C.3	(a) A fiber holder under the test. The temperature near the fiber chuck is measured. (b)The temperature of a fiber holder as a function of time. The fiber chuck is heated up to more than 35°C	82
C.4	(a) A kidney shape for coiling a double cladding fiber. The thick red line represents the coiled fiber. (b) A special fiber with the rectangular-shape inner cladding.	83

List of Tables

2.1	Transition probability in Indium atom	4
3.1	The parameters used in the calculations in Fig. 3.7. The frequencies are expressed in units of γ_{Rb} ($2\pi \times 6$ MHz), the decay rate of the excited state of ^{87}Rb	19
3.2	Parameters of ^{115}In for the calculation.	20
4.1	The spectroscopic parameters of Yb^{3+} in silica [39].	31
4.2	Summary of the important parameters of nonlinear crystals for SHG. θ is the angle between the \vec{k}_ω and the optical axis (Z) of the crystal, and ϕ is the azimuthal angle of the wavevector on the XY plane of the crystal.	46
4.3	Summary of the important parameters of BBO for SFG.	46
4.4	Summary of the cavity parameters for SHG. L_T is a total length of resonators.	47
4.5	Summary of the SH cavity parameters.	50
5.1	Atomic parameters of the cooling transition $^2P_{3/2}$, $F'' = 6 \rightarrow ^2D_{5/2}$, $F''' = 7$	60
A.1	F=3 to F'=4, π -polarisation	75
A.2	F=3 to F'=4, σ^+ -polarisation	75
A.3	F=4 to F'=4, π -polarisation	75
A.4	F=4 to F'=4, σ^+ -polarisation	75
A.5	F=5 to F'=4, π -polarisation	75
A.6	F=5 to F'=4, σ^+ -polarisation	75
A.7	F=4 to F'=5, π -polarisation	76
A.8	F=4 to F'=5, σ^+ -polarisation	76
A.9	F=5 to F'=5, π -polarisation	76
A.10	F=5 to F'=5, σ^+ -polarisation	76
A.11	F=6 to F'=5, π -polarisation	76
A.12	F=6 to F'=5, σ^+ -polarisation	76
A.13	F=4 to F'=4, π -polarisation	77
A.14	F=4 to F'=4, σ^+ -polarisation	77
A.15	F=5 to F'=4, π -polarisation	77
A.16	F=5 to F'=4, σ^+ -polarisation	77

A.17 $F=4$ to $F'=5$, π -polarisation	77
A.18 $F=4$ to $F'=5$, σ^+ -polarisation	77
A.19 $F=5$ to $F'=5$, π -polarisation	77
A.20 $F=5$ to $F'=5$, σ^+ -polarisation	77

Chapter 1

Introduction

Scientists have wanted to control the motion of atoms by means of forces induced by atom-magnetic field or atom-light field interaction. This research field is called atom optics. Such experiments date back to the famous experiment by Otto Stern and Walther Gerlach [1, 2], in which Silver atoms were deflected by an inhomogeneous magnetic field depending on their spin state. A few years later, Otto Frisch deflected an atomic Na beam using light pressure [3]. In the last two decades intense investigations on atom optics have been performed, driven by the advent of laser cooling techniques enabling precise control of the atomic motion with near-resonant laser light [4, 5, 6].

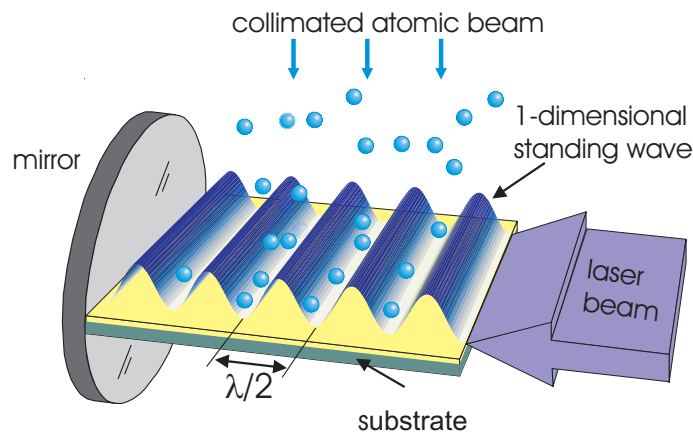


Figure 1.1: Basic concept of ANF.

While laser cooling techniques are in widespread use for the generation of e.g. cold alkali gases for fundamental research, they are also of interest for applications, e.g. atomic nanofabrication (ANF) [7]. Figure 1.1 shows the basic concept of ANF employing a standing wave, the simplest light mask. A collimated atomic beam passes through a near-resonant standing wave generating a dipole potential. Then, due to the dipole force in the transverse direction, atoms under the blue-detuned standing wave are pulled to the intensity minima where the interaction energy is minimal. When a substrate is placed in an appropriate position (focal point), the atoms are focused and accumulated on the

substrate leading to local deposition. The fabricated pattern by this method is the projection of the standing wave. In the case of a 1D standing wave, a line structure can be generated and more complicated structures can be produced by ANF methods using e.g. a holographically generated light mask [8]. So far, ANF methods using various geometries in light masks have been demonstrated in Na [9], Cs [10], Cr [11, 12], Yb [13], and Fe [14]. The ANF method has its own advantages compared to conventional lithography. E-beam lithography can generate very fine structures, but the writing speed is slow due to the serial writing process, and the substrate or mechanical masks can be damaged because of the high energy of electrons. In the ANF method, however, the writing process is parallel and the damage of components can be avoided because neutral atoms with low kinetic energy are used. Another advantage of ANF is its material selectivity. Dopants can be selected by the near-resonant light masks enabling structured doping. For this reason, ANF with technologically relevant atoms has been of interest [7].

Especially, ANF using group III atoms in the periodical table may open a possibility to generate fully 3D structured composite materials [15]. For a successful ANF experiment a transversely laser-cooled atomic beam is essential because the beam divergence plays a critical role in the quality of structures produced, e.g. contrast, sharpness. The transverse laser cooling of atomic beams of group III atoms such as Al, Ga on a cycling transition was demonstrated [16, 17]. Laser cooling on a multi-level, Λ -type transition has been applied to ^{115}In by irradiating five laser frequencies simultaneously [18]. In this case laser cooling on such a transition of In was not efficient because of the intrinsically small scattering rate, the formation of dark states in $F, F + 1 \rightarrow F'$ transitions, and the small velocity capture range of the transient cooling mechanism [19].

In this dissertation, I describe efficient transverse laser cooling of an Indium atomic beam. In Chapter 2 the basic theory of the interaction between Indium atoms and light fields is introduced. In Chapter 3 nonlinear spectroscopy of a 3-level, Λ type level system driven by a pump and a probe beam is investigated in order to understand the absorption line shapes used as a frequency reference in a previous two-color spectroscopy experiment. In Chapter 4, I present a continuous-wave coherent ultraviolet source at 326 nm based on frequency tripling for efficient laser cooling on a cycling transition. Finally, in Chapter 5, I describe sub-Doppler transverse laser cooling of an Indium atomic beam on a cycling transition in the presence of a polarization gradient in a linear-perpendicular-linear polarization configuration.

Chapter 2

Interaction between Indium atoms and light fields

2.1 Indium

Indium is an element of group III with the atomic number of 49 and its atomic weight is 114.82. There are two stable isotopes ^{113}In and ^{115}In with an abundance of 4.3 % and 95.7 %, respectively. The melting point and boiling point are 151.61 °C and 2080 °C, respectively. The vapor pressure of Indium is given by [20]

$$\lg \frac{p}{\text{Torr}} = 8.003 - \frac{12180\text{K}}{T + 273\text{K}}, \quad (2.1)$$

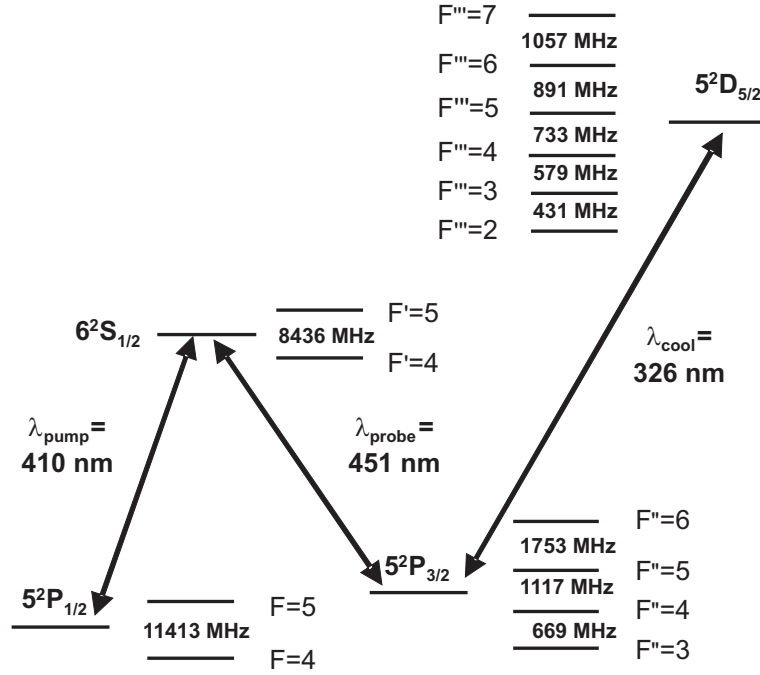
where p is the pressure in Torr, T is the temperature in Kelvin. The vapour pressure is deduced to be 540 mTorr at 1200 °C, the typical operating temperature of an In oven, and 1 μTorr at 600 °C for an all-sapphire cell.

The electronic configuration of Indium is $[\text{Kr}]4d^{10}5s^25p$, and the number of electrons in the outermost shell is 3. Figure 2.1 shows the energy level scheme of ^{115}In which is used in the experiment. The $5P_{1/2}$, $5P_{3/2}$ ground state doublet is connected to the first excited $6S_{1/2}$ state in terms of a 3-level, Λ -type configuration. The $5P_{3/2} \rightarrow 6S_{1/2}$ transition is resonant with blue light at 451 nm, and $5P_{1/2} \rightarrow 6S_{1/2}$ with violet light at 410 nm. The branching ratio of the $6S_{1/2} \rightarrow 5P_{1/2} : 6S_{1/2} \rightarrow 5P_{3/2}$ is about 2 : 3. The $5P_{3/2}$ state is connected to the second excited $5D_{5/2}$ state which is resonant with UV light at 326 nm. This UV transition contains a cycling transition $5P_{3/2}, F'' = 6 \rightarrow 5D_{5/2}, F''' = 7$ which is very suitable for efficient laser cooling. The selected parameters for optical transitions for ^{115}In are shown in Tab. 2.1.

The thermal population of both ground states is given by

$$\frac{N(P_{3/2})}{N(P_{1/2})} = \frac{g_{3/2}}{g_{1/2}} \exp\left(-\frac{\delta E}{k_{\text{B}}T}\right), \quad (2.2)$$

where g_i is the degeneracy of state $|i\rangle$, δE is the energy difference between the two ground states, k_{B} is the Boltzmann constant, T is the temperature. At the operating temperature

Figure 2.1: Energy level scheme of ^{115}In

Property	Symbol	Value
Life time of $6S_{1/2}$	τ_{5S}	6.3 ns
Life time of $5D_{5/2}$	τ_{5D}	7.7 ns
Decay rate of $6S_{1/2}$	$\Gamma/2\pi$	25.1 MHz
Decay rate of $5D_{5/2}$	$\gamma/2\pi$	20.7 MHz
Branching rate $6S_{1/2} \rightarrow 5P_{3/2}$	$\Gamma_{451}/2\pi$	16.2 MHz
Branching rate $6S_{1/2} \rightarrow 5P_{1/2}$	$\Gamma_{410}/2\pi$	8.9 MHz
Saturation intensity in $5P_{1/2} \rightarrow 6S_{1/2}$	I_{sat}^{410}	15.9 mW/cm ²
Saturation intensity in $5P_{3/2} \rightarrow 6S_{1/2}$	I_{sat}^{451}	11.9 mW/cm ²
Saturation intensity in $5P_{3/2} \rightarrow 5D_{5/2}$	I_{sat}^{326}	78.3 mW/cm ²

Table 2.1: Selected parameters for optical transitions of ^{115}In .

of the In oven, a fraction of 20 % of the In atoms are in the $5P_{3/2}$ state. The saturation intensity of the blue and the violet transitions are calculated in Appendix B.

2.2 Density matrix equation

Time evolution of density matrix equations

The density matrix formalism is a reasonable tool to describe the atom-photon interaction, and the time evolution of the density matrix can be expressed by

$$\frac{\partial \hat{\rho}}{\partial t} = \frac{1}{i\hbar} [\hat{H}, \hat{\rho}] + \hat{L}(\rho), \quad (2.3)$$

where \hat{H} is the Hamiltonian, $\hat{\rho}$ the density matrix, and $\hat{L}(\rho)$ is the dissipative part of the evolution. The Hamiltonian can be written in a well-known way as [21]

$$H = H_A + H_I = \sum_i \hbar\omega_i |i\rangle\langle i| + \sum_{i,j} \hbar\Omega_{ij} |i\rangle\langle j| \cos(\nu_{ij}t) + c.c., \quad (2.4)$$

where H_A is the unperturbed atomic Hamiltonian, H_I is the interaction Hamiltonian, ω_i is the eigen frequency of level i , $|i\rangle$ and $\langle i|$ are ket and bra vectors of quantum state i , $\Omega_{ij} = d_{ij}E/\hbar$ is the rabi frequency where d_{ij} is a dipole moment, and ν_{ij} is the angular frequency of the laser coupled to the $|i\rangle$ to $|j\rangle$ transition. If the spontaneous decay is the only relaxation mechanism, the relaxation term in Linblad form is defined as [22]

$$\hat{L}(\rho) = \sum_{i,j} F_{ij} \rho F_{ij}^* - \frac{1}{2} \{F_{ij}^* F_{ij}, \rho\}, \quad (2.5)$$

where $F_{ij} = (\Gamma_{ij})^{1/2} |i\rangle\langle j|$, Γ_{ij} is the rate of spontaneous emission from level i to j . The Hamiltonian can be transformed to the rotating frame by a unitary transformation. The effective Hamiltonian in the new basis is expressed by [23]

$$\tilde{H} = U^\dagger H U - iU^\dagger \frac{\partial U}{\partial t}, \quad (2.6)$$

where U is the transformation operator. One can apply the rotating wave approximation in which the fast oscillating terms ($e^{i2\nu_{ij}t}$) of the Hamiltonian are ignored. The density

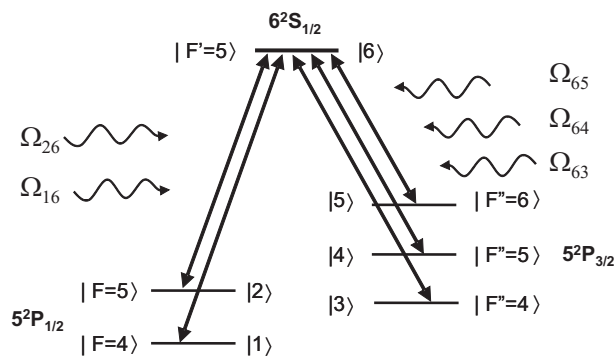


Figure 2.2: Theoretical level scheme of Indium as 6 levels. The states $|1\rangle$, $|2\rangle$, $|3\rangle$, $|4\rangle$, $|5\rangle$, $|6\rangle$ are corresponding to $|5^2P_{1/2}, F=4\rangle$, $|5^2P_{1/2}, F=5\rangle$, $|5^2P_{3/2}, F=4\rangle$, $|5^2P_{3/2}, F=5\rangle$, $|5^2P_{3/2}, F=6\rangle$, $|6^2S_{1/2}, F=5\rangle$ states. Ω_{ij} is the Rabi frequency.

matrix formalism described above can be applied to the Indium system to estimate the time evolution and steady state behavior of Indium atoms in the presence of external fields. For example, one can derive the density matrix equations for a multi-level, Λ -type system

for Indium based on a simplified level scheme as sketched in Fig. 2.2. In this case, using the program *Mathematica*, I could derive 36 density matrix equations where the magnetic sub-levels were not considered. The detailed equations will not be displayed because they are too messy to be written here.

Steady state expressions of density matrix equations

When Indium is coupled with a pump (ν_{16}) and a probe laser (ν_{56}), the Indium can be understood in terms of an open 3-level, Λ -type system, which will be shown in this subsection. One can derive the density matrix equations using Eq. (2.3). Then, the equations can be compactly rewritten in the matrix form as [24]

$$\dot{R} + \Sigma = MR, \quad (2.7)$$

where R are the elements of the density matrix, and Σ is a constant vector. The matrix M and vector Σ can be decomposed into terms as

$$M = M_0 + \Omega_s M_1 + \Omega_s^* M_{-1}, \quad (2.8)$$

and

$$\Sigma = \Sigma_0 + \Omega_s \Sigma_1 + \Omega_s^* \Sigma_{-1}, \quad (2.9)$$

where Ω_s is the rabi frequency of a weak probe field in the system. Substituting the Eqs. (2.8) and (2.9) into (2.7), one can obtain

$$\dot{R} + \Sigma_0 + \Omega_s \Sigma_1 + \Omega_s^* \Sigma_{-1} = (M_0 + \Omega_s M_1 + \Omega_s^* M_{-1})R. \quad (2.10)$$

According to Floquet's theorem, the steady state solution R can be expressed by

$$R = R_0 + \Omega_s R_1 + \Omega_s^* R_{-1} + O(\Omega_s^n), \quad (2.11)$$

where $O(\Omega_s^n)$ represents the high order terms. Substituting Eq. (2.11) into (2.10) and comparing the coefficients of the power of Ω_s , the first order solution of R_1 can be obtained as

$$R_1 = (M_0)^{-1}(\Sigma_1 - M_1 R_0). \quad (2.12)$$

The linear absorption of the probe field is available from the vector R_1 which is corresponding to the linear susceptibility, and the optical force can be deduced by the components of R_1 vector.

From Eq. (2.12) the steady state behavior of Indium coupled with a pump (Ω_{16}) and a probe beam (Ω_{65}) can be deduced as

$$\rho_{65}^{(s)}(\delta_{61}, \delta_{65}) = \frac{i\Omega_{65} [\gamma_{\text{dep}} + i(\delta_{61} - \delta_{65})]}{(\Gamma - 2i\delta_{65}) [\gamma_{\text{dep}} + i(\delta_{61} - \delta_{65})] + \frac{|\Omega_{16}|^2}{2}}, \quad (2.13)$$

where γ_{dep} is the dephasing rate between two ground states. Eq. (2.13) has a similar form as that of a typical 3 level system, except for the population decay rate Γ in which all other losses, e.g. Γ_{62} , Γ_{63} , Γ_{64} , are included. The simplification of the Indium system to an open 3-level scheme is based on this result, and the more detailed calculation of the absorption spectrum including the incoherent pumping and the effective pump and decay rate of the ground states will be described in Chapter 3.

2.3 Laser cooling

Laser cooling plays an essential role in collimating the Indium atomic beam to tightly focus Indium atoms in ANF methods. In this section, the theory of laser cooling is briefly presented, allowing some numbers in the cooling process, e.g. Doppler limited velocity.

Doppler cooling

The reduction of the divergence of an Indium atomic beam, a requirement of the ANF experiment, can be carried out by transverse laser cooling. So I will briefly describe the laser cooling mechanism in this subsection. Light force can be easily understood using the photon picture. When an atom absorbs a photon, the momentum of the photon is transferred to the atom in the propagation direction of the photon. After a certain time (decay time), the atom emits the photon due to spontaneous emission and recoils. The recoil effect induced by spontaneous emission will be averaged out after several cycles of absorption and emission. Thus the atom feels the light force in the propagation direction of the photons. The scattering force can be expressed by

$$F_{\text{SP}} = \hbar k \gamma \rho_{\text{ee}}, \quad (2.14)$$

where $\hbar k$ is the momentum of photons, $\gamma \rho_{\text{ee}}$ is the scattering rate. The steady state solution of ρ_{ee} can be easily obtained by Eq. (2.12) to be

$$\rho_{\text{ee}}^{\text{ss}} = \frac{s_0/2}{1 + s_0 + (2\delta/\gamma)^2}, \quad (2.15)$$

where $s_0 = 2|\Omega|^2/\gamma^2 = I/I_s$ is the saturation parameter. Thus the optical force induced by the scattering process can be obtained by

$$F_{\text{SP}} = \frac{\hbar k \gamma}{2} \frac{s_0}{1 + s_0 + (2\delta/\gamma)^2}. \quad (2.16)$$

For transverse laser cooling, two counter propagating laser beams are introduced to the In atomic beam as shown in Fig. 2.3(a). This configuration is called optical molasses. The force in this case can be expressed by

$$\begin{aligned} F_{\text{OM}} &= F_{\text{SP}}^+ + F_{\text{SP}}^- \\ &= \frac{\hbar k \gamma}{2} \frac{s_0}{1 + s_0 + [2(\delta - kv)/\gamma]^2} - \frac{\hbar k \gamma}{2} \frac{s_0}{1 + s_0 + [2(\delta + kv)/\gamma]^2}, \end{aligned} \quad (2.17)$$

where kv is the detuning caused by the Doppler shift. In the low intensity limit, the force of the optical molasses in Eq. (2.17) can be approximated to be

$$F_{\text{OM}} \cong \frac{8\hbar k^2 \delta s_0 v}{\gamma(1 + s_0 + (2\delta/\gamma)^2)^2} \equiv -\beta v = F_{\text{OM}}^{\text{AP}}, \quad (2.18)$$

where β is the friction coefficient. Figure 2.3(b) shows the calculated force of an optical molasses for the Indium atom. The solid, the dotted, the dot-dashed, and the dashed lines

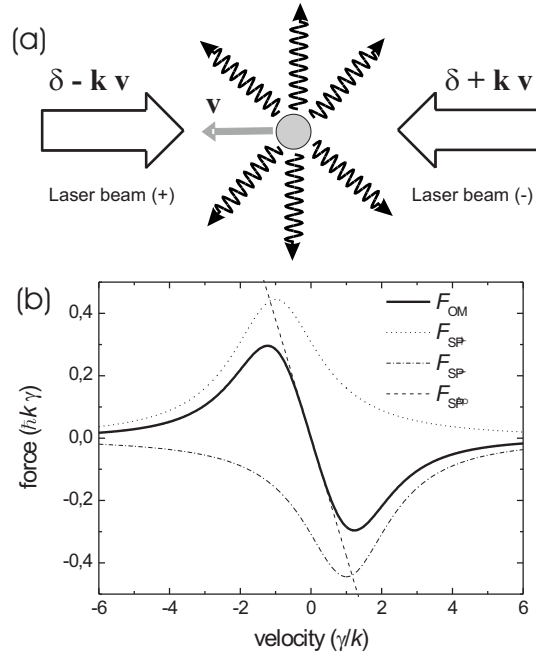


Figure 2.3: (a) Concept of Doppler cooling. The counter propagating red-detuned laser beams interact with an atom moving to the left with a velocity v . (b) Calculated Doppler force using Eq. (2.17) and Eq. (2.18). The solid line for F_{OM} , the dotted and dot-dashed line for F_{SP}^+ and F_{SP}^- , respectively, and the dashed line for F_{OM}^{AP} . $\Omega = 2 \gamma$ and $\delta = 0.5 \gamma$.

are F_{OM} , F_{SP}^+ , F_{SP}^- , and F_{OM}^{AP} , respectively. The force in the Eq. (2.17) has maxima near $\pm v_c^D = \gamma/k$, and the corresponding velocity is called the capture velocity.

In this type of force, there is a heating effect caused by the photon recoil in the spontaneous emission process in analogy with the Brownian motion of molecules. In equilibrium, the heating and the cooling processes are compensated with each other, and the corresponding equilibrium temperature of the atoms under the Doppler-limited force is

$$T_D = \frac{\hbar\gamma}{2k_B}, \quad (2.19)$$

where T_D is the Doppler temperature, k_B is the Boltzmann constant. A typical value of the Doppler temperature is in the order of μK . In the case of Indium, the T_D for the UV transition is calculated to be $500 \mu K$.

Polarization gradient cooling

To overcome the Doppler velocity limit, an efficient friction force can be applied to an atom by introducing a polarization gradient along the direction of the motion of the moving atom, so-called polarization gradient cooling [60]. Figure 2.4 shows the Sisyphus cooling mechanism in the linear-perpendicular-linear (lin \perp lin) configuration in a simple atomic

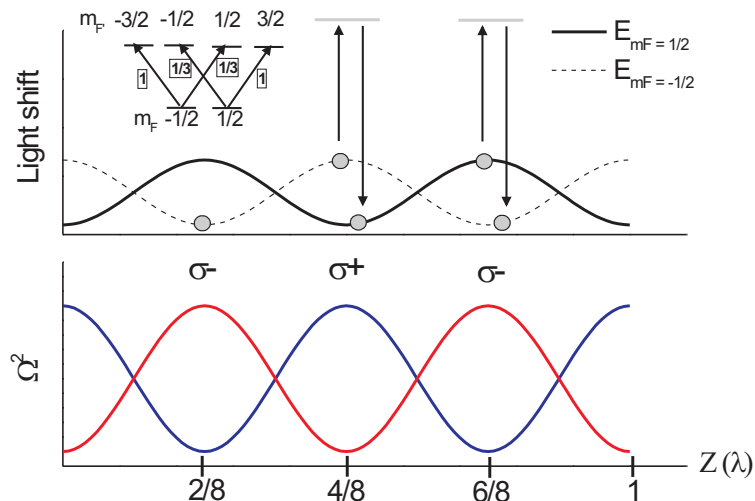


Figure 2.4: Sisyphus cooling mechanism in the lin \perp lin configuration.

level scheme, $J = 1/2 \rightarrow J' = 3/2$ transition. In far red detuned ($\delta \ll -\gamma$) counter-propagating laser beams with the orthogonal linear-polarization, the atom experiences an AC Stark shift which is different for the two ground states as shown in the upper part of Fig. 2.4. Let's assume that an atom starts to move at $z = 2\lambda/8$. During a finite time of τ_p , the atom in the $m_F = -1/2$ state climbs the potential hill to reach the top of the potential hill at $z = 4\lambda/8$ until it is optically pumped into the another ground state, $m_F = 1/2$. In the optical pumping process, the gain of the potential energy corresponding to the light shift Δ_s at the expense of the kinetic energy of the atom is dissipated by spontaneous Raman anti-Stokes photons. The optically pumped atom in the $m_F = 1/2$ state climbs the potential hill again and repeats this sequence. For blue detuned light, the sign of the light shift is inversed so that the atom gains kinetic energy by Stokes photons.

The friction coefficient in the polarization gradient cooling in the lin \perp lin configuration can be roughly derived. The friction force is $F = -\alpha v$ which is maximized at $z = 2n\lambda/8 \sim v\tau_p$ or $kv \sim 1/\tau_p = \gamma_p$. The dissipated energy per unit time is

$$\frac{dW}{dt} \sim -\frac{\hbar\Delta_s}{\tau_p} \sim -Fv = -\alpha v^2, \quad (2.20)$$

so that

$$\alpha \sim -\hbar k^2 \frac{\Delta_s}{\gamma_p} \sim -\hbar k^2 \frac{\delta}{\gamma}, \quad (2.21)$$

where the large detuning ($|\delta| \gg \gamma$) and the low intensity ($\Omega \ll \gamma$) are assumed in the last expression in Eq. (2.21). In spite of the large detuning, the friction coefficient in Eq. (2.21) is larger than that for the Doppler cooling ($\sim \hbar k^2$) [61] while the capture velocity

for the polarization gradient cooling ($v_c \sim \gamma_p/k$) is much smaller than that of the Doppler cooling process ($v_c^D \sim \gamma/k$). The detailed calculations of the optical force for Indium will be given in Chapter 5.

2.4 Atom lens

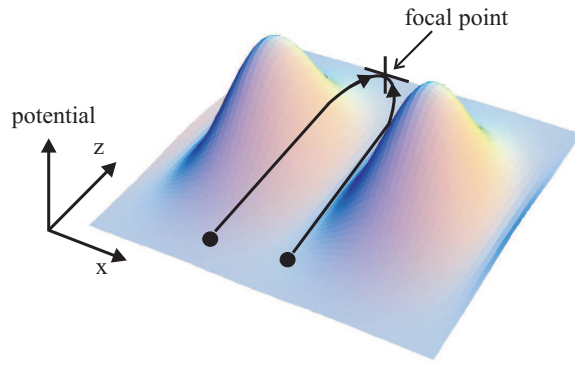


Figure 2.5: Atoms in a dipole potential. Two atoms are traveling through one period of a dipole potential in z direction formed by a standing wave along the x direction. Due to the dipole force exerted along the transverse direction, atoms are focused to the focal point.

In this section, the motion of In atoms in a dipole potential is described. Figure 2.5 illustrates two atoms in a period of an atom lens. Due to the dipole potential induced by a standing wave, the atoms are deflected and focused at the focal point. The potential formed by a standing wave as shown in Fig. 2.5 is written as

$$U(x, y, z) = \frac{\hbar\delta}{2} \ln [1 + p(x, y, z)], \quad (2.22)$$

where

$$p = \frac{I_0}{I_{\text{sat}}^\lambda} \frac{\Gamma^2}{\Gamma^2 + 4\delta^2} g(z) \sin^2 kx = p_0 G(x, y, z), \quad (2.23)$$

where $g(z)$ is the profile of the laser beam along the z direction. It usually has the Gaussian profile, e^{-2z^2/w_z^2} , where w_z is the beam waist in the z direction. Neglecting the y component, the equation of motion of atoms in the dipole potential is given by

$$\begin{aligned} \ddot{x} + \frac{1}{m} \frac{\partial U(x, z)}{\partial x} &= 0, \\ \ddot{z} + \frac{1}{m} \frac{\partial U(x, z)}{\partial z} &= 0, \end{aligned} \quad (2.24)$$

where m is the mass of the atom considered. Using Eq. (2.24), the atomic trajectories in the presence of a dipole potential can be calculated. Figure 2.6(a) shows the calculated trajectories of a perfectly (upper trace) and partially (lower trace) collimated Indium atomic beam in an atom lens. The divergence of the partially collimated atomic beam is set to be 0.48 mrad, which will be determined by the laser cooling experiment. The atomic flux distributions along the x -axis at the focal point for the perfectly and the partially collimated In atoms is calculated yielding the FWHMs of 3 nm and 45 nm, respectively as shown in Fig. 2.6(b). From this simulation, one can expect that the width of the atomic flux will get broader and eventually atoms with large divergence will be homogeneously distributed.

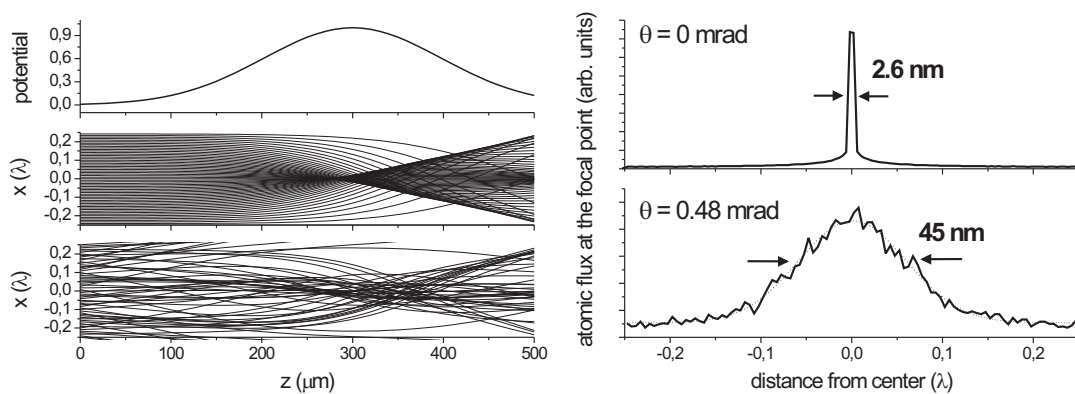


Figure 2.6: (a) The calculated trajectories of a perfectly (upper trace) and a partially (lower trace) collimated Indium atomic beam in an atom lens. The divergence of the partially collimated atomic beam is set to be the experimentally achieved value, 0.48 mrad. (b) The atomic flux along the x -axis for the ideally laser-cooled (upper profile) and the partially laser-cooled (lower profile) In atoms at the focal point. The full-width at half maxima (FWHMs) of the widths of each cases are calculated to be 3 nm and 45 nm. The parameters used in the simulation are $N_{\text{atom}} = 20000$, $I_{\text{sat}} = 10 s_0$, and $\delta = 10 \Gamma$.

Chapter 3

Non-linear spectroscopy with Indium vapor cells

I have studied nonlinear absorption from the In $P_{1/2,3/2}$ ground state doublet in a resistively heated high temperature cell and a hollow cathode lamp. Using probe and pump lasers at 410 nm and 451 nm, respectively, absorption spectra with non-linear properties caused by saturated absorption, coherent dark resonances and by optical pumping are observed. The measured spectra agree very well with a theoretical description in terms of a density matrix theory. The hollow cathode lamp offers a robust device to generate enough density without the need for high temperature cells. High resolution spectra with good signal to noise ratio for laser stabilization e.g. for laser cooling of In have been obtained.

3.1 Saturation spectroscopy in blue transitions

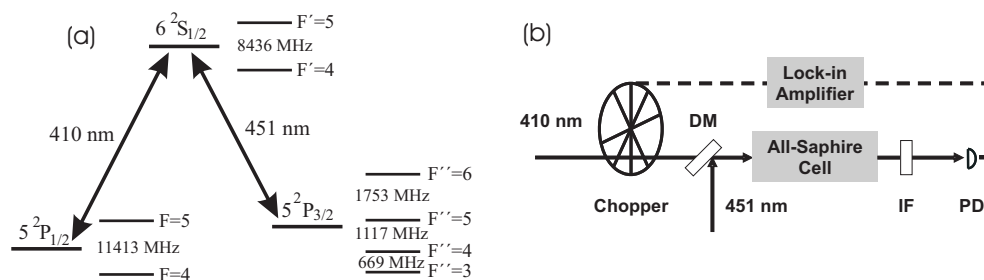


Figure 3.1: (a) Energy level scheme of ^{115}In . (b) Experimental setup for two color spectroscopy. The frequency of the pump laser at 410 nm is locked to the $4 \rightarrow 5$ transition. The frequency of the probe light at 451 nm is scanned around the blue transitions. DM: dichroic mirror; PD: photodiode; IF: interference filter.

Figure 3.1(a) shows the energy level scheme of ^{115}In and Fig. 3.1(b) shows the experimental setup for the two color spectroscopy. An all-sapphire cell (ASC) is heated up to 600°C to provide a reasonable atomic density of $\sim 10^{10} \text{ cm}^{-3}$ [25]. The corresponding Indium vapor pressure is estimated to be $4 \mu\text{Torr}$. An external cavity diode laser at 410 nm and a

frequency doubled Ti:Sa laser at 451 nm are used as pump and probe lasers, respectively. The frequency of the pump laser is locked to the $|5P_{1/2}, F = 4\rangle \rightarrow |6S_{1/2}, F = 5\rangle$ transition, and the probe laser frequency is scanned across the $5^2P_{3/2} \rightarrow 5^2S_{1/2}$ transitions. The powers (intensities) of the pump and probe beams are $645 \mu\text{W}$ ($48 \text{ mW}/\text{cm}^2$) and $241 \mu\text{W}$ ($18 \text{ mW}/\text{cm}^2$), respectively.

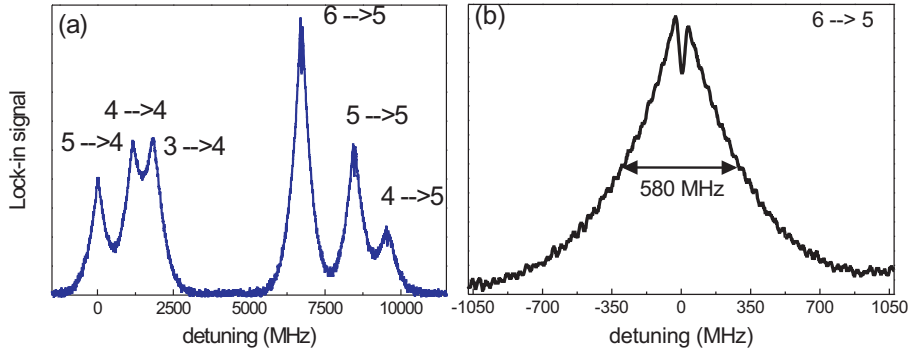


Figure 3.2: (a) Lock-in signal. All hyperfine lines are well resolved. The powers (intensities) of the probe and pump beams are $645 \mu\text{W}$ ($48 \text{ mW}/\text{cm}^2$) and $241 \mu\text{W}$ ($18 \text{ mW}/\text{cm}^2$), respectively. (b) The magnification of the lock-in signal near to $6 \rightarrow 5$ transition. Contrary to the expectation, the FWHM of the observed spectrum is measured to be 580 MHz, far beyond the natural linewidth 25 MHz.

The probe beam and the amplitude modulated pump beam are combined by a dichroic mirror and a pump-probe pair passes through the ASC. After the pump light is filtered out by an interference filter, the absorption of the probe beam is detected by a photo-diode (PD) and is demodulated by a lock-in amplifier (LIA) yielding a Doppler background free absorption signal. Fig. 3.2(a) shows the demodulated absorption spectrum. Small absorption dips can be observed in the $(4,5,6) \rightarrow 5$ transitions, but not in the $(3,4,5) \rightarrow 4$ transitions. An interesting point in the Fig. 3.2(a) is the observation of the $3 \rightarrow 4$ transition. The $F'' = 3$ state cannot be populated by the optical pumping because $F' = 5 \rightarrow F'' = 3$ is a forbidden transition. A possible explanation might be a collision-induced population of the $F'' = 3$ state.

Figure 3.2(b) shows the demodulated absorption spectrum of the probe beam in the presence of the pump beam as a function of the detuning of the probe laser frequency. Because a very weak pump beam is applied, an unsaturated narrow line-shape whose width is comparable to the natural linewidth (25 MHz) is expected. But the width of the observed spectrum is far beyond the expectation. What is the origin of the broadening in the line-shape? In Ref. [26], authors interpreted a broad but sub-Doppler lineshape in terms of velocity changing collisions (VCCs). Instead, I will show that it can be understood as a result of efficient optical pumping by stepwise two photon processes which lead to an unusually low effective saturation intensity and correspondingly broad lineshapes.

3.2 Saturation spectroscopy in violet transitions

Another 3-level, Λ -type system is the $|5^2P_{1/2}, F = 5\rangle \rightarrow |6^2S_{1/2}, F' = 5\rangle \rightarrow |5^2P_{1/2}, F = 4\rangle$ transition preserving the physical concept in the two color spectroscopy as shown in Fig. 3.5. The two hyperfine levels $F = 4$ and $F = 5$ of $5^2P_{1/2}$ serve as the ground states, and $F' = 5$ of $6^2S_{1/2}$ serves as the excited state. Both of the arms in this Λ transition can be driven by the violet diode lasers at 410 nm. Furthermore the absorption in these violet transitions ($\sim 28\%$) is higher than that of the blue transitions. In this section, an electromagnetically induced transparency (EIT) experiment in the violet transitions is discussed.

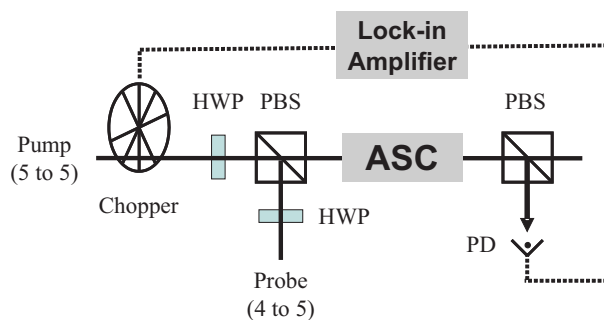


Figure 3.3: Experimental setup for electromagnetically induced transparency (EIT) experiment. HWP: $\lambda/2$ plate; PBS: polarization beam splitter; PD: photo diode; LIA: lock-in amplifier; ASC: all sapphire cell.

Figure 3.3 sketches the experimental setup. Pump and probe beams are coupled by a polarization beam splitter (PBS) to form a pump-probe pair and pass through the ASC. The pair is decoupled by a second PBS, and the absorption of the probe is detected by a PD. Depending on the detection scheme, the pump beam can be amplitude modulated. The frequency of the pump laser is always fixed to the $5 \rightarrow 5$ transition.

An absorption spectrum of the probe beam (0.1 mW) with and without pump beam (1.5 mW) is shown in Fig. 3.4. The absorption spectrum in the presence of the pump beam can be associated with 3 different contributions: the Doppler limited background (FWHM ~ 1270 MHz), an additional broad Lorentzian-like contribution (FWHM ~ 311 MHz), and a narrow Lorentzian (FWHM ~ 4 MHz) substantially below the natural linewidth of 25 MHz at the center of the broader lines.

In Fig. 3.4(b) I show the difference of the absorption spectrum for the $5P_{1/2}(F = 4, 5) \rightarrow 6S_{1/2}(F' = 5)$ transition without and with pump beam. The LIA-signal was obtained by demodulation with a lock-in amplifier. The spectrum shows the same prominent features observed in Fig. 3.2(b), the broad, Lorentzian-like line shape with sub-Doppler width and the narrow dip which is straightforwardly interpreted as a consequence of coherent population trapping leading to electromagnetically induced transparency (EIT).

In this chapter, I analyze the observed line shapes in Sect. 3.2 with special emphasis on the broad but sub-Doppler contribution (LIA-signal) prominent in Figs. 3.4(b) and 3.2(b). I apply a first principles theoretical model to the Λ -system involving the hyperfine levels $F =$

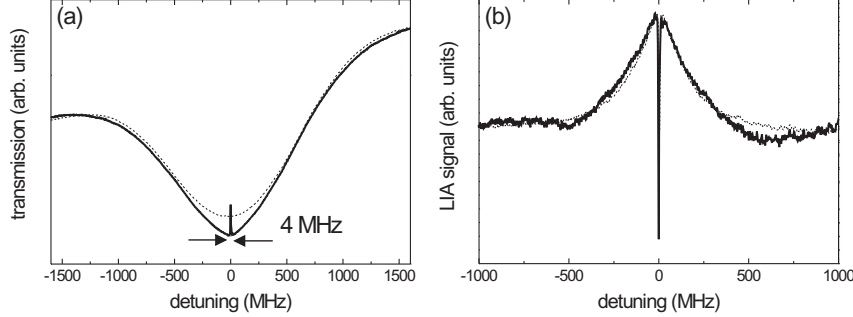


Figure 3.4: (a) Absorption spectra of the probe beam with (solid line) and without (dashed line) the pump beam tuned to the center of the Doppler broadened spectrum. The slanted intensity is due to diode laser power variation. (b) Difference (solid line) of the two spectra from (a) compared with the directly measured absorption signal demodulated by a lock-in amplifier (dotted line).

4, 5 of the $5P_{1/2}$ state but equally applicable to the system involving the two finestructure states $5P_{1/2,3/2}$. The time scale is set by the atomic lifetime which is short compared to the time spent within the laser beams (average transit times $2.8 \mu\text{s}$ vs. $\tau = 6.6 \text{ ns}$). Thus a steady state model is sufficient.

Theoretical model

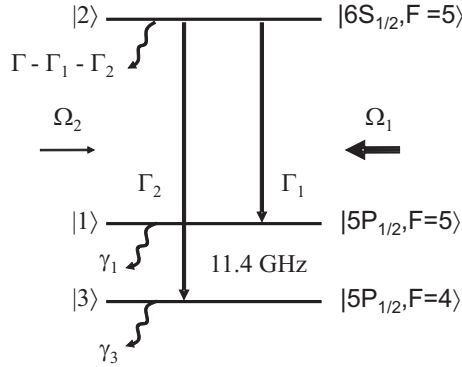


Figure 3.5: Simplified energy level scheme of Indium with pump and probe transitions; γ_i , effective decay rate of the ground states; Γ, Γ_i , total and partial decay rate of the excited state; Ω_i , Rabi frequencies.

In this section, I consider a model treating the Indium atoms as a 3-level, Λ -type system coupled by the pump and probe beam. The pump (Rabi frequency Ω_1) and probe (Rabi frequency Ω_2) are coupled to the $5 \rightarrow 5$ and $4 \rightarrow 5$ transitions, respectively. Further hyperfine levels do not influence the absorption of the probe beam. However they are responsible for additional loss channels in the excited state. These losses lead to significant

depopulation by optical pumping resulting in a large effective saturation parameter and playing a crucial role for understanding the broad sub-Doppler contribution. In Fig. 3.5 I show the simplified energy level scheme. The excited state decays to the coupled ground state with rates Γ_i ($i = 1, 2$), and to other uncoupled ground states with rates $\Gamma - \Gamma_1 - \Gamma_2$, where Γ is the total decay rate of the excited state. Atoms from uncoupled states eventually leave the laser beam, and in turn "fresh atoms" with statistical population of ground state levels replenish the reservoir of atoms. In a simplified model we account for this process through effective ground state decay and pump rates $\gamma = \gamma_1 = \gamma_3$.

The steady state expression of the density matrix equations for the simplified 3-level, Λ -type system in Fig. 3.5 neglecting velocity changing collisions can be written as [27]

$$\begin{aligned}
\gamma\rho_{11}(\vec{v}) &= \lambda_1(\vec{v}) + i\frac{\Omega_1}{2}[\rho_{21}(\vec{v}) - \rho_{12}(\vec{v})] \\
&\quad + \Gamma_1\rho_{22}(\vec{v}), \\
\Gamma\rho_{22}(\vec{v}) &= \lambda_2(\vec{v}) - i\frac{\Omega_1}{2}[\rho_{21}(\vec{v}) - \rho_{12}(\vec{v})] \\
&\quad - i\frac{\Omega_2}{2}[\rho_{23}(\vec{v}) - \rho_{32}(\vec{v})], \\
\gamma\rho_{33}(\vec{v}) &= \lambda_3(\vec{v}) + i\frac{\Omega_2}{2}[\rho_{23}(\vec{v}) - \rho_{32}(\vec{v})] \\
&\quad + \Gamma_2\rho_{22}(\vec{v}),
\end{aligned} \tag{3.1}$$

$$\begin{aligned}
\mu_{12}(\vec{v})\rho_{12}(\vec{v}) &= i\frac{\Omega_1}{2}[\rho_{22}(\vec{v}) - \rho_{11}(\vec{v})] - i\frac{\Omega_2}{2}\rho_{13}(\vec{v}), \\
\mu_{23}(\vec{v})\rho_{23}(\vec{v}) &= i\frac{\Omega_2}{2}[\rho_{33}(\vec{v}) - \rho_{22}(\vec{v})] + i\frac{\Omega_1}{2}\rho_{13}(\vec{v}), \\
\mu_{13}(\vec{v})\rho_{13}(\vec{v}) &= i\frac{\Omega_1}{2}\rho_{23}(\vec{v}) - i\frac{\Omega_2}{2}\rho_{12}(\vec{v}),
\end{aligned} \tag{3.2}$$

where $\lambda_i(\vec{v})$ is the incoherent pumping rate related to the population and

$$\begin{aligned}
\mu_{12}(\vec{v}) &= \Gamma/2 - i(\Delta_1 - k_1v_z), \\
\mu_{23}(\vec{v}) &= \Gamma/2 + i(\Delta_2 - k_2v_z), \\
\mu_{13}(\vec{v}) &= \gamma_{13} + i[(\Delta_2 - \Delta_1) - (k_2 - k_1)v_z]
\end{aligned} \tag{3.3}$$

where Δ_i is the detuning, k_i is the wave number.

The value which is equivalent to the absorption is given by [27]

$$\begin{aligned}
I(\Delta_1, \Delta_2) &= \text{Im} \int d\vec{v} \left(\rho_{33}(\vec{v}) - \frac{\lambda_3(\vec{v})}{\gamma} \right) \\
&= \frac{\Omega_2}{\gamma} \text{Im} \int d\vec{v} \rho_{23}(\vec{v}).
\end{aligned} \tag{3.4}$$

The term $\rho_{23}(\vec{v})$ can be obtained by perturbation theory as [29]

$$\rho_{23}(\vec{v}) = \frac{-i\Omega_2/2}{\mu_{13}(\vec{v})\mu_{23}(\vec{v}) + (\Omega_1/2)^2} \left\{ \mu_{13}(\vec{v})[\rho_{22}^{(0)}(\vec{v}) - \rho_{33}^{(0)}(\vec{v})] + i\Omega_1\rho_{12}^{(0)}(\vec{v})/2 \right\}, \quad (3.5)$$

where the $\rho_{ij}^{(0)}(\vec{v})$ are the zeroth order ($\Omega_2 = 0$) solutions to Eq. (3.1) ~ (3.2) respectively. After integrating Eq. (3.4) over the whole velocity group, one can obtain the expressions as

$$I(\Delta_1, \Delta_2) = I_{12}^{\text{TQ}} + I_{23}^{\text{TQ}} + I^{\text{SW}} + I^{\text{DP}}, \quad (3.6)$$

where Δ_1 and Δ_2 are the pump and probe detunings, respectively, and

$$\begin{aligned} I_{12}^{\text{TQ}} &= \frac{N_{21}(\Omega_1\Omega_2)^2}{8\gamma(k_1u)((k_2 - k_1)u)(k_2u)} \text{Im} \sum_{i=1}^4 A_i Z(r_i), \\ I_{23}^{\text{TQ}} &= N_{32} \frac{\Omega_2^2}{2\gamma(k_2u)} \text{Im} \sum_{i=1}^2 (B_i Z(r_i) - Z(r_7)), \\ I^{\text{SW}} &= \left(1 - \frac{\Gamma_2}{\gamma}\right) \frac{N_{21}(\Omega_1\Omega_2)^2}{8\gamma(k_1u)^2(k_2u)} \text{Im} \sum_{i=1}^4 D_i Z(r_i) \\ I^{\text{DP}} &= N_{32} \frac{\Omega_2^2}{2\gamma(k_2u)} \text{Im} Z(r_7), \end{aligned} \quad (3.7)$$

where k_i is the wave number, $Z(r_i)$ is the plasma dispersion function, and u is the most probable velocity of the atoms. All constants used in Eq. (3.7), (A_i, B_i, D_i, r_i), are identical to those used in Ref. [27].

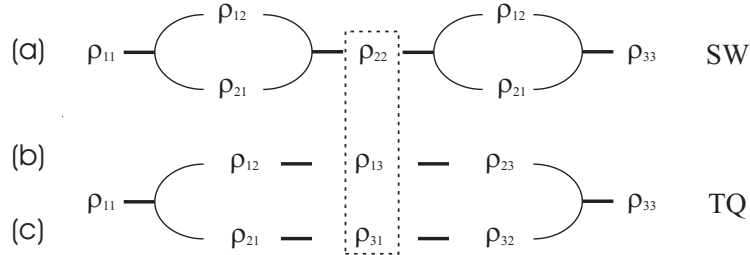


Figure 3.6: Perturbation chains to order $(\Omega_1\Omega_2)^2$ [30]. The stepwise (SW) contribution contains the intermediate population. The two quanta (TQ) terms involve the coherence between the intermediate and ground state of the probe transition.

There are three contributions to the population ρ_{33} in Eq. (3.4) [30]. The zeroth order is corresponding to the thermal population in the absence of the fields. The $(\Omega_2)^2$ order is the linear absorption appearing as the fourth term of Eq. (3.7). The nonlinear absorption term, which we are interested in, is the population in order $(\Omega_1\Omega_2)^2$. Figure 3.6 shows all possible perturbation chains to obtain ρ_{33} to order $(\Omega_1\Omega_2)^2$. The contribution of each chain can be easily calculated in perturbation theory, and all contributions are proportional to

$(\Omega_1\Omega_2)^2$. The chain (a) is corresponding to the stepwise (SW) contribution, because it is related to the intermediate state, ρ_{22} . The second (b) and third (c) chains are called two-quanta (TQ) or coherence contributions because they are related to a coherence term, ρ_{13} , rather than the population of an intermediate state. Depending on the proportionality to thermal populations (N_{21}, N_{32}), they are distinguished by I_{12}^{TQ} and I_{23}^{TQ} , respectively. To check the validity of the calculations above, a typical EIT signal in Rb atoms in reference [31] is reproduced with Eq. (3.6). Fig. 3.7(a) shows the experimental and theoretical results in [31]. The reproduced line shape by Eq. (3.6) is shown in Fig. 3.7(b). The parameters are the same as those used in [31] as shown in Tab. 3.1, and EIT (black) and doppler limited line (red) shapes excellently agree with the reference.

N_{21}	N_{32}	Ω_{12}	γ_{13}	$\gamma_i, \Gamma_{ii}^c, \Gamma_{ij}^{\text{ph}}, S_{ij}^{\text{ph}}$
-5/8	3/8	$17.5 \gamma_{\text{Rb}}$	$0.017 \gamma_{\text{Rb}}$	$10^{-4} \gamma_{\text{Rb}}$

Table 3.1: The parameters used in the calculations in Fig. 3.7. The frequencies are expressed in units of γ_{Rb} ($2\pi \times 6$ MHz), the decay rate of the excited state of ^{87}Rb .

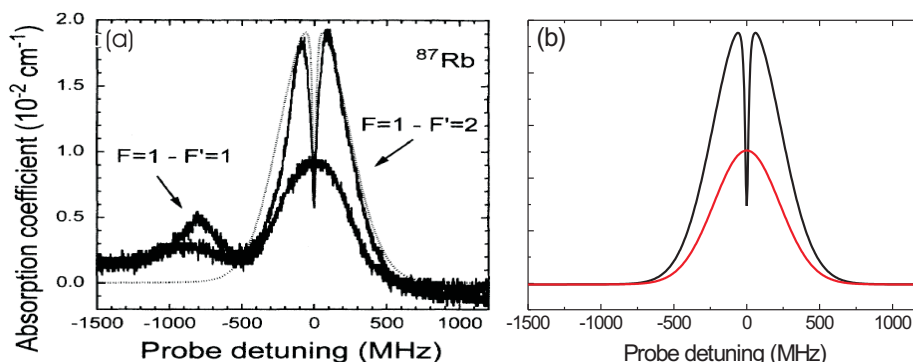


Figure 3.7: (a) A typical EIT signal in a Rb vapor cell [31]. (b) Simulation result. Black and red curves correspond to the probe absorption with (black) and without (red) the pump field. In this calculation, the fourth term in Eq. (3.6) is not subtracted because no LIA was involved to their experiment.

Figure 3.8 shows the 4 individually calculated contributions along with the total absorption line shapes with and without pump beam for Indium. The used parameters are shown in Tab. 3.2. The theoretical results explain convincingly all aspects of the experimental results.

Figure 3.9 shows the theoretical EIT spectra at various pumping intensities. As the intensity of the pump beam is increased, the depth of the EIT dip becomes deeper and the width of the whole feature of EIT becomes broader.

While the interpretation of the Doppler line as well as the coherent dark resonance (TQ) is straightforward, the SW term remains somewhat puzzling. It is of approximately

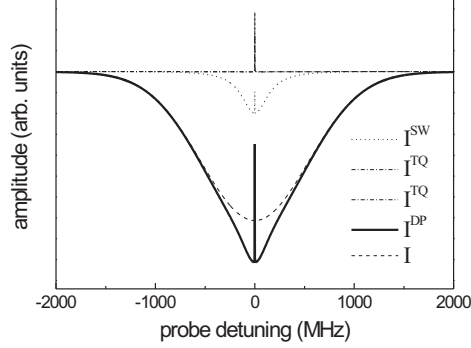


Figure 3.8: The calculated probe beam absorption spectrum with (solid line) and without pump beam (dashed line). Also, the contributions of the coherent two-photon processes (TQ, dashed-dotted lines) and the stepwise contribution (SW, dotted line) are shown.

Property	Symbol	Value
$N(F' = 5) - N(F = 5)$ at 600 °C	N_{21}	-0.5
$N(F = 4) - N(F' = 5)$ at 600 °C	N_{32}	0.4
Rabi frequency of the pump beam	Ω_1	0.5 Γ
Rabi frequency of the probe beam	Ω_2	0.15 Γ
Decay rate between ground states	γ_{13}	0.01 Γ
Decay rate of ground states	γ	$1.6(0.1) \times 10^{-3} \Gamma$

Table 3.2: Parameters of ^{115}In for the calculation.

Lorentzian-line shape and has a width in between typical narrow high resolution features and the Doppler line width. Theoretically the FWHM of the SW term is determined by a parameter [27]

$$\text{FWHM}_{\text{SW}} = \Gamma \sqrt{1 + s_{\text{eff}}^{\text{DM}}}, \quad (3.8)$$

where the effective saturation parameter $s_{\text{eff}}^{\text{DM}}$ of the 3-level, Λ -type system is defined by

$$s_{\text{eff}}^{\text{DM}} = \frac{\Omega_1^2}{\Gamma} \left[\frac{1}{\Gamma} + \frac{1}{\gamma} \left(1 - \frac{\Gamma_1}{\Gamma} \right) \right]. \quad (3.9)$$

For a very weak pump field ($s_{\text{eff}}^{\text{DM}} \ll 1$) the saturation parameter can be neglected so that $\text{FWHM}_{\text{SW}} \sim \Gamma$.

The effective pump and decay rate of the ground state γ in Eq. (3.9) is not known beforehand but can be deduced by measuring the FWHM of the SW component as shown in Fig. 3.4(b) and as a function of the pump intensity. We extract the FWHM of the SW term by fitting two Lorentzian functions (one for the SW, another one for the TQ term).

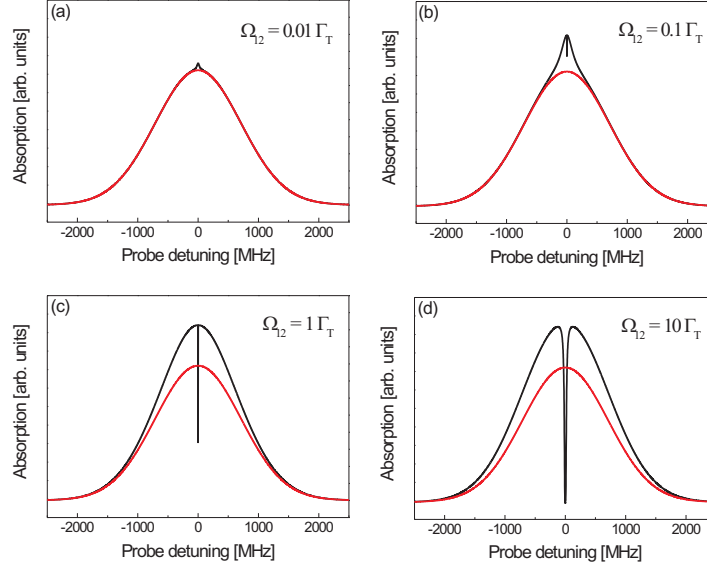


Figure 3.9: Theoretical EIT spectra at various coupling intensities.

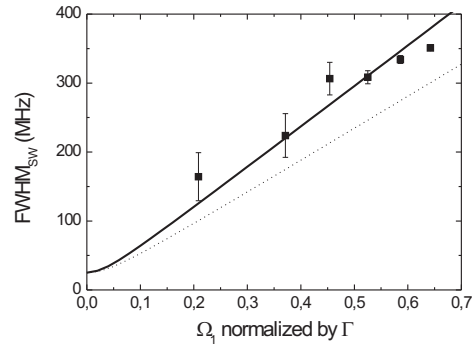


Figure 3.10: The FWHM of SW as a function of the Rabi frequency of the pump beam. The data are fitted (solid line) by Eq. (3.9) yielding $\gamma = 1.6(0.1) \times 10^{-3} \Gamma$. The dotted line is the FWHM deduced by $s_{\text{eff}}^{\text{RE}}$ in a rate equation model for the same γ .

The data are shown in Fig. 3.10 as a function of the pump beam intensity. By fitting the data with Eq. (3.9) the value for γ is found to be $1.6(0.1) \times 10^{-3} \Gamma$.

The effective decay rate for the ground states is a rough measure for the rate of atoms entering and leaving the laser beam. Considering the average thermal velocity of In atoms at 600 °C and the beam diameter of the pump beam, this rate is estimated to be $2 \times 10^{-3} \Gamma$ which compares well with the value inferred from our measurements. The $s_{\text{eff}}^{\text{DM}}$ based on the measured γ is calculated to be 137 at the pump Rabi frequency $\Omega_1 =$

0.5Γ . The solid line in Fig. 3.10 shows the fitted FWHM of the SW term due to the surprisingly large values for $s_{\text{eff}}^{\text{DM}}$. The very large saturation parameter can be interpreted as a consequence of strong optical pumping in such a 3-level, Λ -type system. Typically the pump intensity is much stronger than that of the probe, and the ground state of the probe transition experiences almost no decay. Thus, for resonant excitation atoms are rapidly (in comparison to the transit time of the atoms through the laser beam) pumped to uncoupled states. Even relatively far off resonance optical pumping remains efficient since small excitation probabilities are compensated by long dwell times within the laser beam ($\tau_{\text{transit}} = 400/\Gamma$).

In order to gain more physical insight I have studied in addition to the full density matrix treatment a rate equation model which neglects all coherences and compares the effective saturation parameters deduced by the density matrix and rate equation models. Here I describe the complete rate equations which are exactly the same as those from the density matrix model except the coherences. The rate equations in the theoretical model in Fig. 3.5 can be written as

$$\begin{aligned}\dot{N}_1 &= R_1(N_2 - N_1) + \Gamma_1 N_2 - \gamma N_1 + \lambda_1, \\ \dot{N}_2 &= R_1(N_1 - N_2) + R_2(N_3 - N_2) - \Gamma N_2 + \lambda_2, \\ \dot{N}_3 &= R_2(N_2 - N_3) + \Gamma_2 N_2 - \gamma N_3 + \lambda_3,\end{aligned}\tag{3.10}$$

where R_i is the optical pumping rate and can be written as

$$R_i = \frac{\Omega_i^2}{\Gamma} \frac{1}{1 + (2\Delta_i/\Gamma)^2}, \quad (i = 1, 2).\tag{3.11}$$

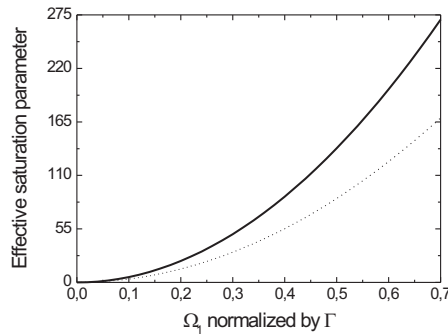


Figure 3.11: The effective saturation parameter deduced by the density matrix model (solid line) and the rate equation model (dotted line). See also Fig. 3.10.

After simple algebra assuming no thermal populations in the excited state $N_{20} = 0$, and the unity total populations $N_t = N_1 + N_2 + N_3 + N_L = 1$, the steady state expression of

the population difference $\Delta N_{32}^{\text{ss}}$ can be obtained to be

$$\begin{aligned} \Delta N_{32}^{\text{ss}} &= N_3^{\text{ss}} - N_2^{\text{ss}} \\ &= N_{31}^0 \frac{\gamma(3R_1 + \Gamma)}{2\gamma\Gamma + R_2(3\gamma + \Gamma + \Gamma_1 - \Gamma_2)} \times \frac{1}{1 + s_{\text{eff}}^{\text{RE}}} \\ &\quad + (1 - N_L^{\text{ss}}) \frac{(\gamma\Gamma + R_1(\Gamma - \Gamma_1 + \Gamma_2))}{2\gamma\Gamma + R_2(3\gamma + \Gamma + \Gamma_1 - \Gamma_2)} \times \frac{1}{1 + s_{\text{eff}}^{\text{RE}}}, \end{aligned} \quad (3.12)$$

where $\Gamma = \Gamma_1 + \Gamma_2 + \Gamma_L$, Γ_L is the decay rate of the excited state into the uncoupled states, and N_L^{ss} is the population in the uncoupled state indicating the leakage. The saturation parameter from the rate equation model, $s_{\text{eff}}^{\text{RE}}$ is defined by

$$\begin{aligned} s_{\text{eff}}^{\text{RE}} &= \frac{\Omega_1^2 \frac{\Gamma^2}{\Omega_2^2} (3\gamma + \Gamma - \Gamma_1 + \Gamma_2) + 6\Gamma}{\Gamma^2 (3\gamma + \Gamma + \Gamma_1 - \Gamma_2) + 2\gamma \frac{\Gamma^2}{\Omega_2^2}} \\ &\approx \frac{\Omega_1^2}{\Gamma} \left[\frac{3}{2} \frac{1}{\Gamma} + \frac{1}{2\gamma} \left(1 - \frac{\Gamma_1 - \Gamma_2}{\Gamma} \right) \right], \end{aligned} \quad (3.13)$$

where I assume that the square of the probe Rabi frequency is much smaller than other frequency scales ($\Omega_2^2 \ll \Gamma^2, \gamma\Gamma^2/\Gamma_i, \gamma\Gamma$). The form of $s_{\text{eff}}^{\text{RE}}$ is similar to that of $s_{\text{eff}}^{\text{DM}}$ and the slight difference between them can be attributed to the usage of a different model. Fig. 3.11 shows the $s_{\text{eff}}^{\text{DM}}$ and $s_{\text{eff}}^{\text{RE}}$ as a function of the Rabi frequency of the coupled pump beam. The dotted line in Fig. 3.10 shows the FWHM of SW term based on the $s_{\text{eff}}^{\text{RE}}$ in a rate equation model.

The effective saturation intensity for the experimental value of γ is found at the low pump Rabi frequency $\Omega_1 = 0.054 \Gamma$ ($I_{\text{sat}}^{\text{eff}} = 1.9 \text{ mW/cm}^2$) from the rate equation model and $\Omega_1 = 0.043 \Gamma$ ($I_{\text{sat}}^{\text{eff}} = 1.2 \text{ mW/cm}^2$) from the density matrix model which are one order of magnitude smaller than that deduced by the two level system (16 mW/cm^2). For the given parameters in Tab. 3.2, the $s_{\text{eff}}^{\text{RE}}$ is calculated to be 86 which is comparable to $s_{\text{eff}}^{\text{DM}} = 137$ from the density matrix model.

In addition I have checked the dependence of FWHM_{SW} on the transit time by comparing the spectra for two different beam diameters d (1 and 3 mm) at a fixed pump Rabi frequency ($\sim 0.2\Gamma$). For the FWHMs of the LIA signals we find $164 \pm 35 \text{ MHz}$ for the small beam and $271 \pm 12 \text{ MHz}$ for the large beam. In the limit $\gamma \ll \Gamma_i, \Omega_i$ the theoretical ratio should be approximately $\text{FWHM}^{(1 \text{ mm})} / \text{FWHM}^{(3 \text{ mm})} \sim \sqrt{\gamma^{(3 \text{ mm})} / \gamma^{(1 \text{ mm})}} = \sqrt{1 \text{ mm} / 3 \text{ mm}} = 0.58$ which compares very well with the measured ratio $164/271 \sim 0.6$.

3.3 Spectroscopy of In with a hollow cathode lamp

An alternative source of atomic vapor to an ASC is a hollow cathode lamp (HCL) which can provide robust and compact atomic references [32, 33]. Here I show that a discharge in a novel hollow cathode lamp produces excellent absorption densities without the need of high temperatures.

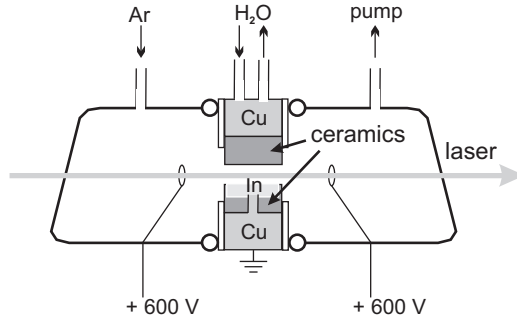


Figure 3.12: Schematic drawing of the hollow cathode lamp. The cathode is made of pure Indium which is inserted into a crucible made of nonconducting ceramic (dark grey). The Indium pool is grounded by a copper inlet (light grey) at the bottom of the crucible. The crucible has a length of 30 mm and a clearance of 5 mm above the Indium pool.

While the ASC provides good spectroscopic access to the relevant In transitions, it is enclosed by a high temperature oven and hence the dissipated electrical power impairs experiments by e.g. air currents. We have thus constructed a new hollow cathode lamp which closely resembles the concept presented in [34] and is outlined in Fig. 3.12. It is operated at ambient temperature, thus avoiding the technical disadvantages of the ASC. It generates a vapor density equivalent to a temperature in excess of 1000 °C, the population in the upper finestructure ground state is $N(P_{3/2}) = 18\%$. The hollow cathode lamp is specially designed for materials with low melting points (In: 156 °C) which cannot directly be used to make massive electrodes. Furthermore, there is no need for a buffer gas that impairs the application of Doppler free methods of laser spectroscopy for laser stabilisation [35].

The cathode is made of pure Indium which is inserted into a crucible made of nonconducting ceramic. At the bottom of the crucible a copper inlet ensures electric conductivity between the Indium pool and the outer grounded copper casing. When the Indium melts during normal discharge operation it remains confined to this reservoir. The crucible has a length of $L = 30$ mm and free space of 5 mm above the Indium pool allowing the laser beam to travel through. The whole cathode block is watercooled to 17 °C. The anode is made of two stainless steel rings which are mounted 5 mm to the sides of the cathode holder. The assembly of two pyrex tubes and a central cathode is clamped together and sealed with o-rings. The cell pressure is sustained by a roughing pump at a level of 500 Pa while venting the cell with argon gas which ensures a stable discharge. The discharge current is supplied by a 2 kV voltage power supply with a maximum current of 100 mA DC. The minimum current at which we can observe a stable discharge is about 20 mA. The electrical resistance of the discharge is approximately 6 k Ω .

A single laser beam ($\lambda = 451$ nm) with intensity $0.08 I_{\text{sat}}^{451}$ passes just above the In reservoir through the cell. The transmitted intensity is measured with a photo-diode behind the cell as a function of laser frequency for different discharge currents. The laser frequency is scanned across the $F'' = 6 \rightarrow F' = 5$ transition at 451 nm. Figure 3.14 shows the strong, Doppler broadened absorption lines at a discharge current of 40 mA. The dips correspond

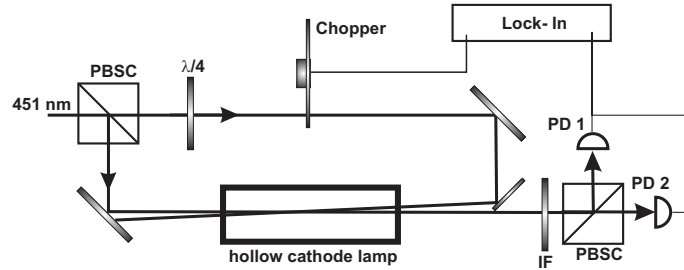


Figure 3.13: Setup for spectroscopy with the HCL. The incoming laser beam is split in half by a polarising beam splitter cube (PBSC) and guided through the hollow cathode lamp (HCL). The pump beam is circular polarized and can be amplitude modulated with a chopper wheel. The polarisation of the probe beam behind the HCL is analyzed with photodiodes PD1 and PD2 and demodulated with a lock-in amplifier. An interference filter (IF) blocks light caused by the discharge.

to the $F'' = 6 \rightarrow F' = 5$ transition for the larger one and the $F'' = 5 \rightarrow F' = 5$ transition for the smaller one. The minima of the two peaks serve as a frequency calibration for the lower axis. The absorption for the larger dip ($6 \rightarrow 5$) is $(95 \pm 3) \%$ and the FWHM is $\Delta\nu = (1620 \pm 20)$ MHz. The flattened line shape in the center of the absorption spectrum in Fig. 3.14 is attributed to saturation.

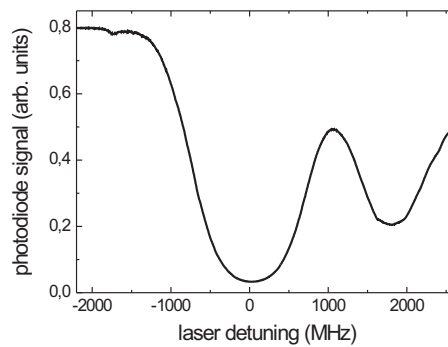


Figure 3.14: HCL: Doppler broadened transmission spectrum of the 451 nm probe laser for the $5P_{3/2}, F'' = 6, 5 \rightarrow 6S_{1/2}, F' = 5$ transitions. Discharge current is 40 mA.

For Doppler free polarization spectroscopy a circularly polarized pump beam is shone in counter propagating to the linear polarized probe beam as shown in Fig. 3.13. The pump beam is amplitude-modulated with a chopper wheel rotating at a frequency of 1.4 kHz. The probe beam is split behind the HCL with a polarizing beam splitter cube (PBSC) oriented 45° with respect to the polarization axis of the beam. The two output beams are detected with photo-diodes and subtracted. An interference filter in front of the PBSC blocks all light generated by the discharge. The difference signal of the photo diodes is

analyzed with a lock-in amplifier.

Fig. 3.15 shows the resulting dispersive signal which is typical for polarization spectroscopy with an additional Doppler base of (140 ± 10) MHz. The width of the dispersive signal is (22 ± 1) MHz. The smaller signal which is about 275 MHz below the large resonance belongs to the ^{113}In isotope which has a natural abundance of 4.3 %. The dispersive signal could be used as an error signal for a feedback circuit to reduce slow drifts of the Ti:Sapphire laser. Since the discharge is robust, laser stabilization is ensured for hours.

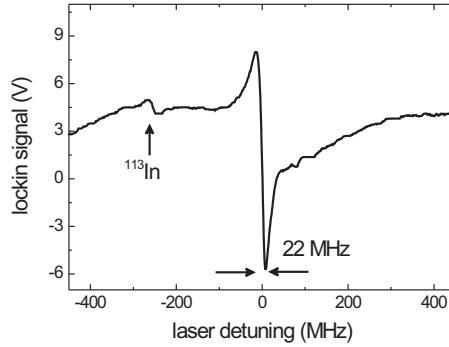


Figure 3.15: Narrow line width signal obtained by polarization spectroscopy. The small dispersive signal is the $F'' = 6 \rightarrow F' = 5$ transition of ^{113}In .

The width (22 MHz) of the peak-to-peak in the dispersive signal in Fig. 3.15 is a little bit smaller than that of the natural linewidth (25 MHz) of the $5S_{1/2}$ state. This is somewhat strange because the resolution limit of a saturation spectroscopy cannot exceed the natural linewidth. In the polarization spectroscopy the birefringence induced by a circularly polarized pump beam is measured by a linearly polarized probe beam. Specifically the difference between the real part of the refractive indices of σ^+ and σ^- is measured. After the simple Jones matrix calculations, the signal in a polarization spectroscopy is obtained to be

$$I_{\text{sig}} = kL(n_{+1}^{\text{R}} - n_{-1}^{\text{R}}) = kL\Delta n^{\text{R}} = L\Delta\alpha_0 \frac{x}{1+x^2}, \quad (3.14)$$

where k is the wavevector, L is the interaction length, n_q^{R} is the real part of the refractive index of a polarization component q , $\Delta\alpha_0$ is the maximum difference in absorption at the line center, and $x = \frac{\omega_0 - \omega}{\Gamma/2}$. Eq. (3.14) exhibits the dispersive character, and the width between peak-to-peak is the natural linewidth Γ . What can be the origin of such a subnatural linewidth? This can be attributed to uncertainties in the frequency calibration due to several possible reasons, e.g. the hysteresis or nonlinearity of the PZT in the Ti:Sapphire laser, or the uncertainty of the minima of the two peaks in Fig. 3.14. In our previous spectroscopy experiment, the width of the peak-to-peak in the dispersive signals for $4 \rightarrow 5$ and $5 \rightarrow 4$ transitions are measured to be 70 MHz as shown in Fig. 3.16(a), where the frequency was calibrated by the separation between the sharp absorption peaks of the two hyperfine states, $4 \rightarrow 5$ and $5 \rightarrow 4$ as shown in Fig. 3.16(b).

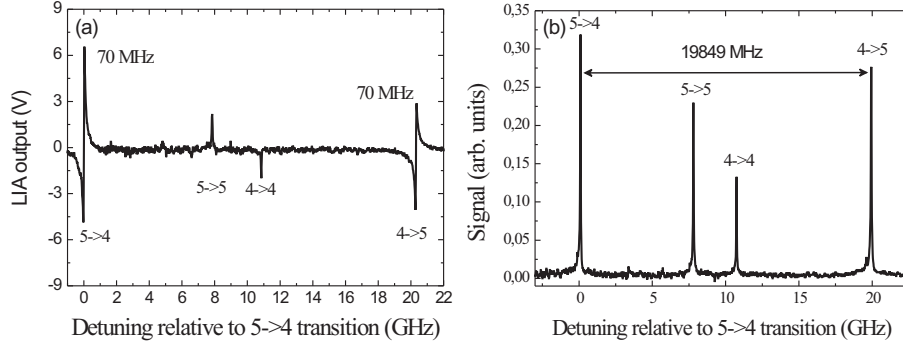


Figure 3.16: (a) The observed dispersive signal for polarization spectroscopy. The width of the peak-to-peak in the dispersive signals for $4 \rightarrow 5$ and $5 \rightarrow 4$ transitions is measured to be 70 MHz. (b) The transmission signal at 410 nm for saturation spectroscopy with an ASC [26].

Furthermore, the dispersive shape in Fig. 3.15 is unsymmetric. This can be understood in terms of the imperfect orientation of the PBSC at 45° . When the orientation of the PBSC is slightly rotated with respect to the 45° -position, i.e. $45^\circ + \delta\theta$, the expected signal in the polarization spectroscopy is calculated to be

$$I_{\text{sig}} = kL \underbrace{[n_{+1}^{\text{R}} - n_{-1}^{\text{R}}]}_{\text{dispersive}} + 2\delta\theta \underbrace{(n_{+1}^{\text{I}} + n_{-1}^{\text{I}})}_{\text{Lorentzian}} - \underbrace{2\delta\theta}_{\text{offset}}, \quad (3.15)$$

where n_q^{I} is the imaginary part of the refractive index of a polarization component q . The Lorentzian term causes an unsymmetry in the dispersive shape, and the offset in I_{sig} is linearly increased by the mistilted angle $\delta\theta$. The offset can be checked by comparing the center point of the dispersive signal from the polarization spectroscopy and the center of the peak of the Lorentzian shape from the saturation absorption spectroscopy.

Assuming that the main contribution to the lineshape shown in Fig. 3.14 is due to Doppler broadening only, the temperature can be inferred from the linewidth $\Delta\nu$ (FWHM),

$$T = \frac{m \lambda^2}{8 \ln 2 R} \Delta\nu^2, \quad (3.16)$$

where m is the atomic mass of Indium and R the gas constant. Fig. 3.17(a) shows the extracted temperatures as a function of the discharge current. The widths have been determined by fitting two Gaussians representing the two transitions onto the measured data. The resulting uncertainty in the temperature is 2 %. Already at the minimal stable discharge current, the temperature of the atoms is comparable to the temperature in the all-sapphire cell. At higher currents the signal saturates around $T_{\text{eff}} \sim 1500$ K. In this region the absorption signal is strongly saturated and causes larger uncertainties.

The depth of the absorption signal is given by Beer's law from which it is possible to derive the density n of the gas as

$$n = -\ln \left(\frac{I}{I_0} \right) \cdot (\sigma L)^{-1}, \quad (3.17)$$

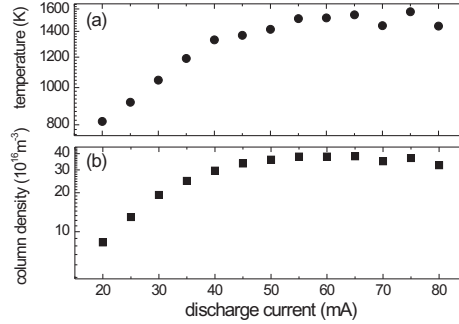


Figure 3.17: (a) The inferred temperature and (b) the In vapor density as a function of discharge current. The discharge is not stable below 20 mA. Temperature and density differ slightly because the density is a function of not only the measured width, $\Delta\nu$, but also of the transmission, I/I_0 .

where a uniform density of neutral atoms in the plasma and optically thin sample are assumed. The Doppler broadened absorption cross section can be calculated from the measured temperature by

$$\sigma = \frac{\lambda^3}{8\pi^{3/2}} \Gamma_{451} \sqrt{\frac{M}{RT}}. \quad (3.18)$$

Here, M is the molar mass. The branching rate of the $6S_{1/2} \rightarrow 5P_{3/2}$ transition is $\Gamma_{451} = 2\pi \times 16.2$ MHz. The density as a function of the discharge current is plotted in Fig. 3.17(b). Again two Gaussians were fitted but the resulting uncertainty of 23 % is higher than before as both the depth and the width influence the density. The measured density is in a reasonable range where the density at 20 mA of $8.3 \times 10^{16} \text{ m}^{-3}$ corresponds to a thermal vapour cell with a temperature of 816 K.

3.4 Conclusion

I observed and analyzed open Λ -type two-color transitions with In vapor cells. A perturbative 3-level model [27] convincingly and exhaustively explains all aspects of the observed spectra and under different conditions. This model provides an excellent basis for understanding line shapes involving 3 coupled levels in gas cells.

Experimentally I have shown that a special hollow cathode lamp overcomes the technical disadvantages of a high temperature spectroscopy cell. It offers high densities at low ambient temperatures. Doppler free spectroscopy offers narrow spectral lines well suited for e.g. laser stabilization. I expect that the concept of this spectroscopy cell can be transferred to more elements.

Chapter 4

A UV laser source based on fiber amplifiers

I have demonstrated a tunable single frequency source of continuous-wave (CW) coherent ultraviolet (UV) radiation at $\lambda_{3\omega} = 326$ nm. Laser light of a tunable diode laser at $\lambda_{\omega} = 977$ nm was split and injected into two independent fiber amplifiers yielding 1 W and 0.4 W, respectively. The 1 W branch was resonantly frequency doubled, resulting in 120 mW of useful power at $\lambda_{2\omega} = 488$ nm. The third harmonic was generated by summation of the second branch of λ_{ω} and $\lambda_{2\omega}$ which were enhanced by a doubly resonant cavity. This light source has TEM₀₀ character and can be continuously tuned over more than 18 GHz. This light source is used for efficient laser cooling of In and is of interest for potentially other applications.

4.1 Fiber light source

4.1.1 Introduction

The first rare-earth doped fiber source had begun with the demonstration of a flash-lamp-pumped neodymium-doped fiber amplifier [36]. After 24 years, a single mode fiber laser [37] was demonstrated. The combination of rare-earth doped fibers as a gain medium and diode lasers as a pumping source made fiber-based light sources so practical, but the power scale of commercial single-mode diode lasers was limited to a few hundred milliwatts.

A breakthrough idea to overcome the problems came from the cladding pumping scheme using double-clad fibers. Figure 4.1 shows a schematic of a fiber amplifier consisting of a double-clad fiber (DCF), a seed, and a pump source. The pump and seed beams are coupled by a dichroic mirror to be coupled into the DCF. The pump beam is guided through a multimode inner cladding to pump the doped rare-earth ions in the core, and the seed light is guided by the single mode core. Through the stimulated emission processes, the seed light is amplified as it propagates in the rare-earth doped core. The greatest advantage of a DCF is that multi-mode, high power diode sources such as multi-diode arrangements, diode bars, and stacks, can serve as pumping sources for the fiber-based light sources. Thanks to the semiconductor technologies, the power from those multi-mode diode lasers

is in the range of several hundred Watts. A CW high power fiber laser generating more than 1 kW output power was reported [38], and currently fiber laser systems with higher power in the range of 100 kW are under development.

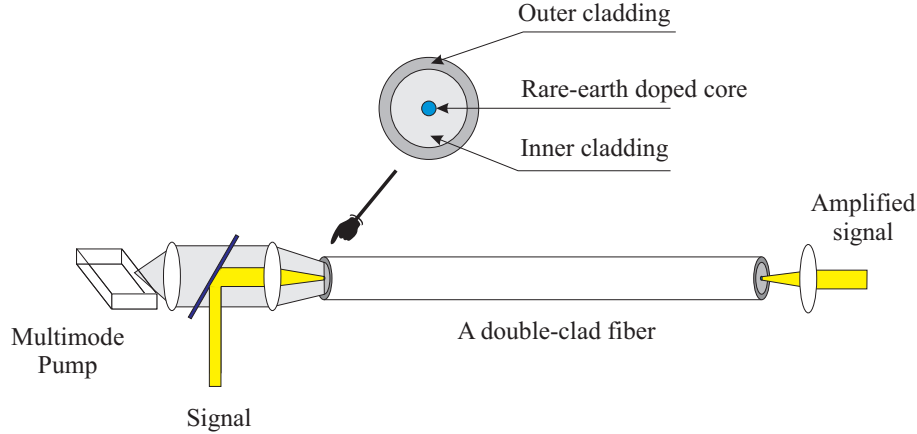


Figure 4.1: Schematic of a double-clad fiber amplifier. A multi-mode pump beam and a single mode seed beam are combined by a dichroic mirror, and the pair of pump and seed beam is coupled to the multi-mode inner cladding ($\phi \sim 10^2 \mu\text{m}$) and the single mode core ($\phi \sim \mu\text{m}$), respectively. The rare-earth ions doped in the core are pumped by the pump beam, and the seed beam is amplified through the stimulated emission process. The amplified seed beam is out-coupled by a lens.

In the point of view of the atomic physicist, high output power is not the only requirement in experiments. The ideal light sources should have narrow spectral width, wide frequency tuning range, good polarization property, easiness of handling, and good spatial beam quality. Fiber sources fulfill the most requirements above if they are appropriately prepared. In the atomic physics laboratory, a well-established single mode diode laser as a seed beam can be combined with a rare-earth doped fiber as a gain medium to form an efficient fiber amplifier.

Since the first demonstration of fiber lasers using an Yb-doped fiber [40], these fiber sources have attracted the interest of scientists due to the high efficiency, high CW power, broad absorption and emission bandwidth, and compactness. Usually Yb doped fiber sources operate at $1030 \sim 1060 \text{ nm}$ in the quasi-four level system because of the small absorption at the emission wavelengths at $1030 \sim 1060 \text{ nm}$ and low threshold pump power. Laser action at 980 nm , the wavelength of interest for our experiment, is unusual due to a large absorption peak at $\sim 977 \text{ nm}$. Careful considerations should be taken in a Yb-doped fiber source operating at 977 nm [41], which are discussed later.

4.1.2 Yb-doped double clad fiber

Spectroscopic characteristics of Yb^{3+} in silica

The electronic configuration of Yb^{3+} is $[\text{Xe}]4f^{13}$, so there is only a single hole in the 4f shell. $^2F_{7/2}$ and $^2F_{5/2}$ serve as a ground state and an excited state, respectively, as shown

in Fig. 4.2. The energy gap between them is around $11,000 \text{ cm}^{-1}$. There are two laser transitions at 980 nm (the three level transition) and at $\sim 1030 \text{ nm}$ (the quasi four level transition).

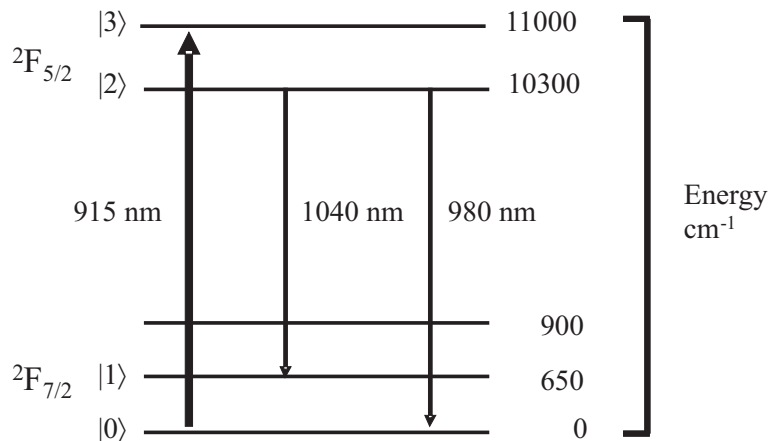


Figure 4.2: The energy level diagram of Yb^{3+} in silica [39]

Figure 4.3 shows the emission (dotted) and absorption (solid) cross sections of Yb^{3+} in a germanosilicate glass [40]. In the absorption spectrum, there are two pump bands at $\sim 915 \text{ nm}$ and $\sim 975 \text{ nm}$ with bandwidths of $\sim 4 \text{ nm}$ and $\sim 50 \text{ nm}$, respectively. Usually the 915 nm band is used for 977 nm output, and 975 nm is employed for 1060 nm output. In the emission spectrum, there are also two main emission bands at 977 nm and 1060 nm with FWHM linewidth of $\sim 4 \text{ nm}$ and $\sim 50 \text{ nm}$, respectively. In the case of 1060 nm Yb-doped fiber sources (YDFS), the pump absorption at 977 nm is maximized, but that of the signal or the lasing beam is minimized. Due to this fact, Yb-doped double cladding fibers (YDCFs) are conventionally operating at 1060 nm instead of 977 nm. The detailed considerations are presented in the next section. Table 4.1 shows the important spectroscopic parameters of Yb^{3+} in silica [39].

λ (nm)	σ (10^{-25} m^2)	τ
910	$\sigma_a = 8$	$\tau_{32} \leq 1 \text{ ns}$
977	$\sigma_a = 25$	$\tau_2 = 770 \mu\text{s}$
	$\sigma_e = 25$	$\tau_{10} \leq 1 \text{ ns}$
1036	$\sigma_e = 6$	$\tau_2 = 770 \mu\text{s}$

Table 4.1: The spectroscopic parameters of Yb^{3+} in silica [39].

Challenges in a YDCF light source operating at 980 nm

In this section, special considerations of a YDCF light source operating at 980 nm are presented. As explained above, there are two emission peaks at 980 nm and 1030 nm in Yb^{3+} , which work in a 3 and a quasi-4 level system, respectively. The required populations

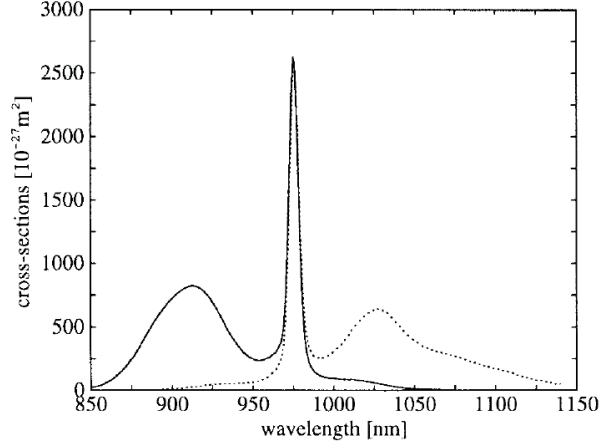


Figure 4.3: Emission (dotted line) and absorption (solid line) cross sections of Yb^{3+} in a germanosilicate glass [40]. The technical difficulty in a Yb-doped double cladding fiber (YDCF) source operating at 977 nm results from the fact that the absorption and the emission cross-sections are maximum at 977 nm.

which bleach the saturable absorption are 50 % in 980 nm and only 5 % in 1030 nm. In the case of a conventional YDCF, a high pump power is required to bleach the gain medium in the 3 level system due to the poor overlap factor (≤ 0.001) which is determined by the ratio of the core to the inner cladding area. The threshold pump power of a fiber source is given by [40]

$$P_{\text{th}} = \frac{A_{\text{core}} h \nu_p}{\Gamma_{\text{pump}} \left(\frac{\sigma_{\text{es}} \sigma_{\text{ap}}}{\sigma_{\text{as}}} - \sigma_{\text{ep}} \right) \tau}, \quad (4.1)$$

where P_{th} is the threshold pump power required to bleach the gain medium, Γ_{pump} is the overlap factor of the pump beam, A_{core} is the area of the core, h is Planck's constant, ν_p is the frequency of the pump laser and τ is the life time of the metastable state. The overlap factor of a pump beam in a double cladding structure can be approximated to be the ratio of the area of the doped core to that of the cladding [42]. σ_{ep} and σ_{es} are the emission cross-sections at the pump and the signal frequency respectively, and the σ_{ap} and σ_{as} are the absorption cross-sections at the pump and the signal frequency, respectively. The P_{th} for 977 nm transition is calculated to be 4.7 W, while that for the 1030 nm transition is only 320 mW. For a practical amplifier, the threshold pump power should be lower than 500 mW. As expected from Eq. (4.1), a high overlap factor or a small size of the inner cladding is required to decrease P_{th} . In addition to a low P_{th} , there is another important consideration, the gain at 1030 nm. The relation between gain (decibel) at 976 nm and 1030 nm can be written as [41]

$$\begin{aligned}
G^{1030} &= G^{976} \frac{\sigma_{e1030}/\sigma_{ep} - \sigma_{a1030}/\sigma_{ap}}{\sigma_{es}/\sigma_{ep} - \sigma_{as}/\sigma_{ap}} - \alpha_p \beta \frac{\sigma_{e1030}/\sigma_{es} - \sigma_{a1030}/\sigma_{as}}{\sigma_{ep}/\sigma_{es} - \sigma_{ap}/\sigma_{as}} \\
&= 0.25 G^{976} + 0.72 \beta \alpha_p,
\end{aligned} \tag{4.2}$$

where σ_{a1030} and σ_{e1030} are the absorption and emission cross-sections at 1030 nm, and $\beta = \frac{\Psi_d^s}{\Psi_d^p} \sim \frac{A_{\text{cladding}}}{A_{\text{core}}}$ and Ψ_d^i is the normalized modal intensity averaged over the dopant area, and α_p is the pump absorption in decibel. A conventional YDCF has a β of 469 which means that the gain at 1030 nm grows rapidly with increasing pump absorption by 338 dB for every decibel of pump absorption. In practice, the initial amplified spontaneous emission (ASE) at 1030 nm is of the order of 10^{-7} W and the ASE power at 1030 nm in the experiment is around the order of 10^{-2} W after a 1 m long fiber, which means $G^{1030} \sim 50$ dB amplification. Considering 0.5 dB pump absorption, G^{976} is - 476 dB, almost complete absorption. To decrease the gain at G^{1030} , a small β and a small area of the inner cladding are necessary.

A company in Denmark, Crystal Fibre, manufactures a special YDCF with a small inner cladding of 27 μm . For the efficient coupling of a multi-mode diode pump laser, air holes were made around the inner cladding to increase the numerical aperture (NA) to more than 0.55. Fig. 4.4 shows the cross-section of the fiber.

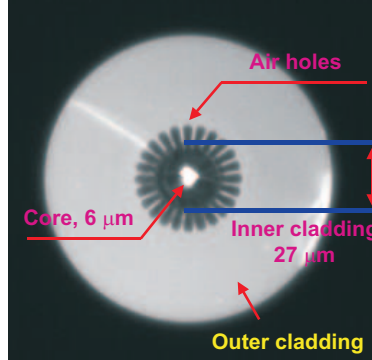


Figure 4.4: The cross-section of the YDCF manufactured by Crystal Fibre. The core diameter is 6 μm while the multi-mode inner cladding has a diameter of 27 μm . The main difference between this fiber and other conventional double cladding fibers is the small diameter of the inner cladding allowing a high overlap factor. For the efficient coupling of a pump beam, the numerical aperture is enhanced up to 0.55 by air holes around the inner cladding.

Let's estimate the gain at 976 nm in this special fiber. Here β is 24.1 and the pump absorption is 1 dB for a 1 m long fiber. For the practical amplifier, unwanted gain at 1030 nm is recommended to get down to 25 dB. Therefore the desired gain at 976 nm can be obtained from Eq. (4.2) as 30 dB, which means 1 W output power from 1 mW seed power. The calculated P_{th} is 201 mW which is quite an amount smaller than that of a traditional YDCF.

A Yb-doped jacketed air-clad fiber (YJACF) has been developed to decrease β without affecting Ψ_d^p [43]. The microscopic image of a YJACF is shown in Fig. 4.5. The ring doping

of Yb ions around the core makes it possible to decrease β down to a core pumped device. The YJACF can be also used to obtain high power at 977 nm, but the photodarkening effect can play an important role in the 3 level system with high gain [44].

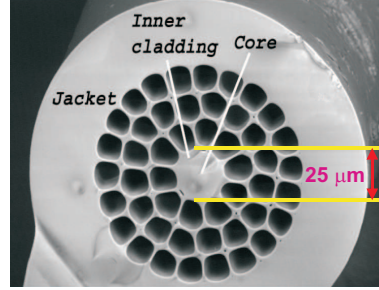


Figure 4.5: The microscopic pictures of Yb-doped jacketed air-clad fiber (YJACF) manufactured by Optoelectronics Research Center at the University of Southampton.

4.1.3 Theoretical model

In this section, a simple theoretical model based on rate equations is described to deduce the expected power from a YDFA. Provided that amplified spontaneous emission (ASE) in the lasing process is negligible, the populations of Yb ions in the ground and excited states can be expressed by simple rate equations [40].

$$\begin{aligned}\frac{dN_2(t)}{dt} &= (R_{12} + W_{12}) N_1(t) - (R_{21} + W_{21} + \gamma) N_2(t), \\ \frac{dN_1(t)}{dt} &= -(R_{12} + W_{12}) N_1(t) + (R_{21} + W_{21} + \gamma) N_2(t),\end{aligned}\tag{4.3}$$

where R_{12} and W_{12} are the pumping rates induced by the pump and signal photons, R_{21} and W_{21} are the emission rates induced by the pump and signal photons, and γ is the spontaneous emission rate of a meta-stable state of Yb ions. The steady state solutions can be easily obtained by

$$\begin{aligned}N_2^0 &= \frac{R_{12} + W_{12}}{R_{12} + R_{21} + W_{12} + W_{21} + \gamma}, \\ N_1^0 &= 1 - N_2^0.\end{aligned}\tag{4.4}$$

The pumping and emission rates are expressed by

$$\begin{aligned}
R_{12} &= \frac{\sigma_{\text{ap}} I_{\text{p}}}{h\nu_{\text{p}}} = \frac{\Gamma_{\text{pump}} P_{\text{p}}}{hcA_{\text{core}}} \sigma_{\text{ap}}, \\
R_{21} &= \frac{\sigma_{\text{ep}} I_{\text{p}}}{h\nu_{\text{p}}} = \frac{\Gamma_{\text{pump}} P_{\text{p}}}{hcA_{\text{core}}} \sigma_{\text{ep}}, \\
W_{12} &= \frac{\sigma_{\text{as}} I_{\text{s}}}{h\nu_{\text{s}}} = \frac{\Gamma_{\text{signal}} P_{\text{s}}}{hcA_{\text{core}}} \sigma_{\text{as}}, \\
W_{21} &= \frac{\sigma_{\text{es}} I_{\text{s}}}{h\nu_{\text{s}}} = \frac{\Gamma_{\text{signal}} P_{\text{s}}}{hcA_{\text{core}}} \sigma_{\text{es}},
\end{aligned} \tag{4.5}$$

where Γ_{signal} is the overlap factor of the signal beam with the core which is easily determined by the single mode fiber theory. The change of power of the pump and the signal beam in the propagation direction in a YDCF is given by

$$\begin{aligned}
\frac{P_{\text{s}}(z)}{dz} &= \Gamma_{\text{signal}} [(\sigma_{\text{as}} + \sigma_{\text{es}})N_{\text{t}}^0 - \sigma_{\text{as}}N_{\text{t}}] P_{\text{s}}(z), \\
\frac{P_{\text{p}}(z)}{dz} &= -\Gamma_{\text{pump}} [\sigma_{\text{ap}}N_{\text{t}} - (\sigma_{\text{ap}} + \sigma_{\text{ep}})N_{\text{t}}^0] P_{\text{p}}(z),
\end{aligned} \tag{4.6}$$

where N_{t} is the total density of Yb ions in the core. In Eq. (4.6) copropagating pump and signal beams are assumed.

The spectroscopic parameters, e.g. emission and absorption cross sections, and life time of the meta stable state of Yb ions in a glass medium, can be obtained from Ref. [40]. The total density of Yb ions can be easily determined by measuring the absorption of the pump light in a YDCF. The small-signal-absorption coefficient is given by [45]

$$\alpha(\lambda) = \Gamma_{\text{pump}} \sigma_{\text{ap}}(\lambda) N_{\text{t}}. \tag{4.7}$$

4.1.4 Fiber amplifier operating at 977 nm

Basic measurements

The coupling efficiency of a multi-mode pump beam is measured to be 78 % using a 5 cm long YDCF. Then, the absorption of the pump beam by Yb ions in the single-mode core is obtained to be 1.1 dB/m by measuring the transmission of the pump beam through a 1 m long YDCF. For this measurement, very weak power (1.23 mW) was used to satisfy the small-signal-absorption condition. This value is similar to the specification provided by the manufacturer. Considering the density of mole mass of Yb ions (394 g/mol) and the density of fused quartz (2.203 g/cm³), absorption can be also calculated to be 1097 ppm [46]. The coupling efficiency of the signal beam into the Yb doped single mode core is obtained from the measurement of the transmission of the signal beam. First of all, the YDCF is operated in the optimized condition which means that the seed beam is optimally coupled into the core. Then, the pump beam is cut to measure the transmitted seed power. In this measurement, very weak seed power is required to suppress a lasing

process. The seed power coupled into the core will be completely absorbed by Yb ions due to the strong absorption at 980 nm region. The part of the seed power coupled into the inner cladding will be transmitted after experiencing a certain amount of absorption. The transmitted power guided by the inner cladding P_{out} can be written as

$$0.96^2 P_{\text{in}} (1 - \eta_{\text{core}}) e^{-\alpha l} = P_{\text{out}}, \quad (4.8)$$

where 0.96^2 is the consideration of Fresnel losses at the incidence and exit surfaces of the YDCF, l is the fiber length in use, P_{in} is the input power at the seed wavelength. From this measurement the coupling efficiency η_{core} was obtained to be 70 %, which is similar to the coupling of the seed laser to a normal single mode fiber.

Experimental setup

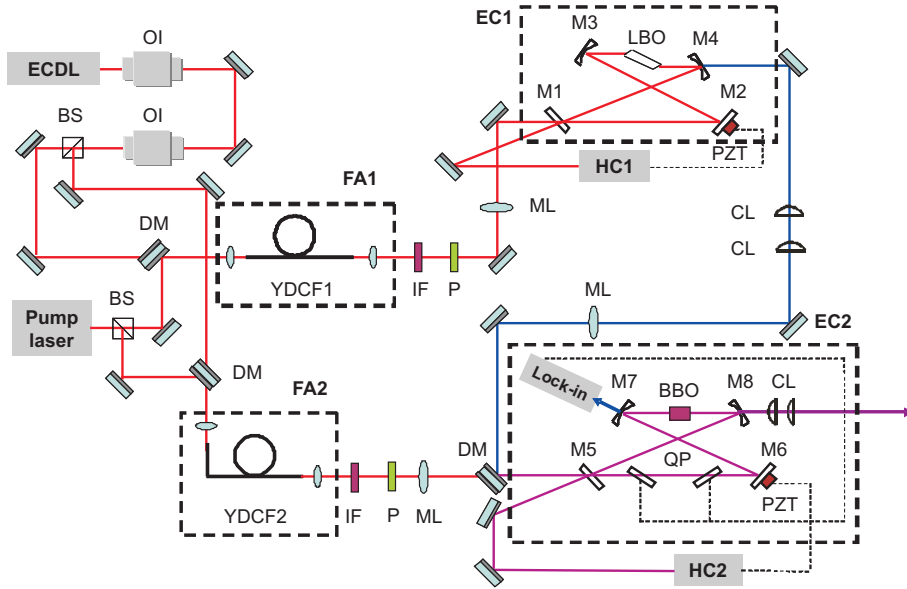


Figure 4.6: Experimental setup. Our system uses a diode laser system (ECDL), two fiber amplifiers (FA) and two external cavities (EC) for upconversion, $\lambda_{\omega} \rightarrow \{\lambda_{\omega}, \lambda_{2\omega}\} \rightarrow \lambda_{3\omega}$. ECDL: external cavity diode laser; EC: external cavity; YDCF: Yb-doped double clad fiber; HC: Hänsch-Couillaud method; OI: optical isolator; DM: dichroic mirror; M: mirror; CL: cylindrical lens; ML: mode-matching lens; IF: interference filter; PZT: piezo-electric transducer; BS: beam splitter; P: polarizer; QP: quartz plate.

The schematic of the experimental setup is shown in Fig. 4.6 [47]. As a seed source a home-built external cavity diode laser (ECDL) emitting λ_{ω} at 977 nm is employed. Two 60 dB optical isolators protect the ECDL from backreflections. A 920 nm, 40 W multi-mode diode laser module (Fianium PUMA-920-40) serves as a pump source. As a gain medium for the amplification of the seed power, a YDCF is selected. The fiber is angle cleaved ($\sim 8^\circ$) in order to suppress back-reflection induced lasing. Two independent fiber

amplifiers are used rather than just splitting the output beam from one amplifier in order to obtain efficient operation and to escape the photo darkening effect caused primarily by a high population inversion which is required in 3 level Yb-doped fiber light sources at ~ 977 nm [44]. We split the seed and pump beams into two beams each and form two seed-pump beam pairs by combining them with dichroic mirrors. The pairs are then coupled to the YDCFs by a 3.1 mm focal length and 0.68 NA collimating lens. At each output port of the FAs, the pump light is eliminated by an interference filter.

Performance of YDCFs

Figure 4.7 shows the experimental and theoretical output power from both FAs as a function of the launched pump power. The lengths of the first (FA1, YDCF1) and the second (FA2, YDCF2) fibers are 1.2 m and 0.8 m, respectively. With 14 W pump power launched into each FA, we obtain 1.26 W (0.63 W) at λ_w from FA1 (FA2) using 20 mW (15 mW) seed power. Solid lines are the calculated output powers based on a rate equation model [40], and experiment and theory are in good agreement. The corresponding gains are 18 dB for FA1 and 16 dB for FA2.

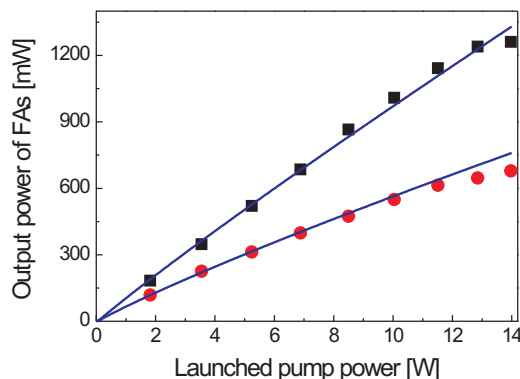


Figure 4.7: Experimental output powers of FA1 (rectangles) and FA2 (circles) at 977 nm as a function of the launched pump power at ~ 920 nm. The solid lines show the theoretical output powers.

For the laser cooling experiment, a light source should have a narrow linewidth ($\leq \gamma$). The output spectrum of the seed (ECDL) and one of the YDCFAs operating at full power is compared in Fig. 4.8(a). Both spectra have no significant difference except amplified spontaneous emission which is suppressed down to 33 dB. The beating signal between the seed and one of the YDCFA is shown in Fig. 4.8(b). The 3 dB bandwidth of the signal is 18 kHz, which means both of them are almost identical. Figure 4.9 shows the long term power stability of one of YDCFAs. Two different signals of the same output beam are measured simultaneously. The upper trace is the normal output power, and the lower trace is that behind a polarizer. After a slight adjustment of the alignment at ~ 2 hours,

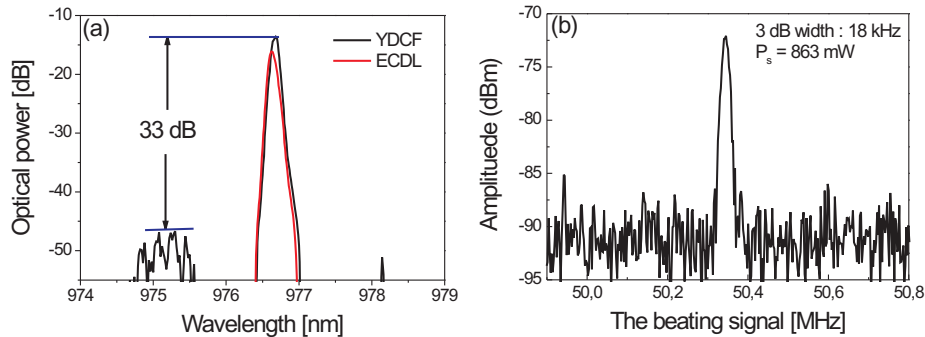


Figure 4.8: (a) The spectrum of the seed laser (ECDL) and the FA operating at full power. Suppression of ASE is more than 33 dB below the carriers as measured with an optical spectrum analyzer. (b) The beating signal between seed laser and FA operating at full power. 3 dB bandwidth is 18 kHz.

the power of the fiber amplifier becomes stable because the mechanical system enters the thermal equilibrium. In the stable region, the averaged values of the upper and the lower trace are 1003 ± 5 and 878 ± 4 mW, respectively yielding ± 0.5 % deviations. Although the YDCF is non-polarization preserving, only small polarization fluctuations are observed. The origin of the power fluctuations in the FAs may originate from the instabilities of the power of the pump and the seed lasers, or from a mechanical instability of the fiber holders yielding a variation of the coupling of the pump and the seed beams to the gain fiber.

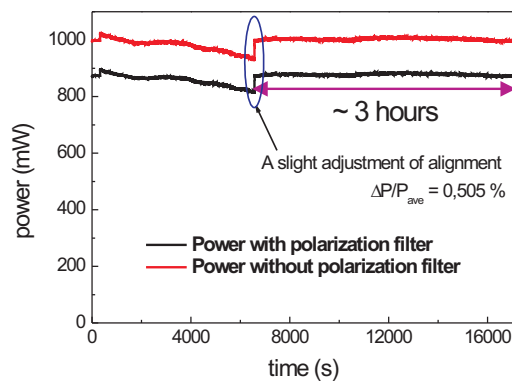


Figure 4.9: Long term power stability of a YDCFA. After a slight adjustment of the alignment at ~ 2 hours, the power of the fiber amplifier becomes stable because the mechanical system enters the thermal equilibrium. In the equilibrium region, the instability of the output power is measured to be ± 0.5 % of the averaged power.

4.2 Nonlinear frequency conversion

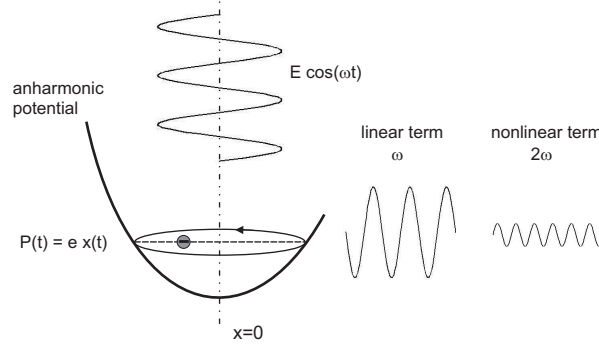


Figure 4.10: A Lorentz oscillator in an anharmonic potential. $P(t)$ is the induced polarization which exhibits nonlinear response to the driving field, $E(t)$.

Nonlinear interaction of light and matter can be understood in terms of a simplified classical model. Let's consider a Lorentz oscillator under a weak anharmonic force excluding the linear damping for simplicity as shown in Fig. 4.10. The induced polarization is $P = ex(t)$. The equation of motion of a Lorentz oscillator is given by

$$\frac{d^2}{dt^2}x + \omega_0^2 x + \alpha x^2 = \frac{e}{m} [E_1 \cos(\omega_1 t) + E_2 \cos(\omega_2 t)], \quad (4.9)$$

where the term αx^2 represents an anharmonic force. The solution of Eq. (4.9) is expanded in a perturbative way like

$$x(t) = x^{(1)}(t) + x^{(2)}(t) + x^{(3)}(t) + \dots \quad (4.10)$$

The first order term is the linear part, and the higher order terms are nonlinear terms. The second order solutions include $\omega_1 \pm \omega_2$, $2\omega_i$, and a zero frequency term. The zero frequency term means a constant macroscopic polarization of the sample, so-called optical rectification or inverse Kerr effect. The other terms well describe sum- and difference-frequency generation, and second harmonic generation.

Generally, the induced polarization of second order can be expressed by

$$P_i(\omega) = \epsilon_0 \sum_{jk} \sum_{mn} \chi_{i,j,k}^{(2)}(\omega; \omega_m, \omega_n) E_j(\omega_m) E_k(\omega_n), \quad (4.11)$$

where $\chi_{i,j,k}^{(2)}$ is the nonlinear susceptibility in second order. In a crystal with inversion symmetry or centrosymmetry, the second order susceptibility cannot exist. When one takes the inversion of all coordinates, the sign of the electric field and the induced polarization should be changed except for that of the susceptibility as

$$P_i = \epsilon_0 \chi_{i,j,k}^{(2)}(E_j)(E_k) \quad \rightarrow \quad -P_i = \epsilon_0 \chi_{i,j,k}^{(2)}(-E_j)(-E_k) \quad (4.12)$$

resulting in $\chi_{i,j,k}^{(2)} = 0$. One of the representative materials with inversion symmetry is glass in which there no second order nonlinear process can exist, e.g. second harmonic generation. But this symmetry can be broken on the surface of a glass so that second harmonic generation is possible by matching phase conditions appropriately. A more detailed description of nonlinear optics is given in the next section.

4.2.1 Theory on nonlinear optics

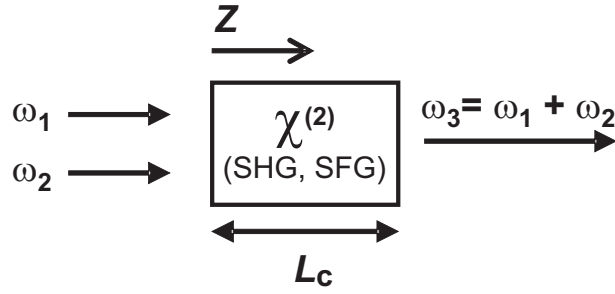


Figure 4.11: Concept of nonlinear frequency conversions.

In this section, a theory on nonlinear frequency conversion based on $\chi^{(2)}$ processes is quantitatively described using nonlinear coupled wave equations. A conceptual schematic is shown in Fig. 4.12. Two input frequencies of ω_1 and ω_2 pass through a nonlinear medium with a length of L_c and an output frequency of ω_3 is produced after the nonlinear process in the medium. The general form of the wave equation in matter without any free current is written as

$$\begin{aligned}\vec{\nabla} \times \vec{\nabla} \times \vec{E}(\vec{r}, t) &= \vec{\nabla}(\vec{\nabla} \cdot \vec{E}(\vec{r}, t)) - \vec{\nabla}^2 \vec{E}(\vec{r}, t) \\ &= -\mu\epsilon \frac{\partial^2}{\partial t^2} \vec{E}(\vec{r}, t) - \mu \frac{\partial^2}{\partial t^2} \vec{P}(\vec{r}, t),\end{aligned}\quad (4.13)$$

where μ is the permeability of the medium, ϵ_0 is the vacuum permittivity. Although the first term of the vector identity cannot be removed in nonlinear optics, it can be neglected in planar waves. The induced polarization term can be divided into linear and nonlinear terms, $\vec{P}(\vec{r}, t) = \epsilon_0 \chi \vec{E}(\vec{r}, t) + \vec{P}^{\text{NL}}(\vec{r}, t)$. If we assume that the induced polarization vector is parallel to the electric fields, the vector form can be expressed by the scalar form. Considering this, Eq. (4.13) can be expressed by

$$\nabla^2 E(r, t) = \mu\epsilon \frac{\partial^2}{\partial t^2} E(r, t) + \mu \frac{\partial^2}{\partial t^2} P^{\text{NL}}(r, t),\quad (4.14)$$

where μ is the magnetic permeability, ϵ is the electric permeability. Electric fields can be written as

$$E_{\omega_i}(z, t) = \frac{1}{2} \left[E_i(z) e^{i(\omega_i t - k_i z)} + c.c. \right], \quad (i = 1, 2, 3). \quad (4.15)$$

The induced nonlinear polarizations can be expressed by

$$\begin{aligned} P_{\omega_1}^{\text{NL}}(z, t) &= 2\epsilon_0 d_{\text{eff}} E_{\omega_2}^*(z, t) E_{\omega_3}(z, t), \\ P_{\omega_2}^{\text{NL}}(z, t) &= 2\epsilon_0 d_{\text{eff}} E_{\omega_1}^*(z, t) E_{\omega_3}(z, t), \\ P_{\omega_3}^{\text{NL}}(z, t) &= 2\epsilon_0 d_{\text{eff}} E_{\omega_1}(z, t) E_{\omega_2}(z, t), \end{aligned} \quad (4.16)$$

where d_{eff} is the effective nonlinear coefficient. Using the slowly-varying-amplitude approximation expressed by

$$\left| k_i \frac{\partial}{\partial z} E_i(z) \right| \gg \left| \frac{\partial^2}{\partial z^2} E_i(z) \right|, \quad (4.17)$$

and useful expression, $\partial/\partial t = i\omega_i$, after simple algebra one can get finally three coupled wave equations as

$$\begin{aligned} \frac{d}{dz} E_1(z) &= -2i \frac{\omega_1}{cn_{\omega_1}} d_{\text{eff}} E_2^*(z) E_3(z) e^{-i\Delta kz}, \\ \frac{d}{dz} E_2^*(z) &= +2i \frac{\omega_2}{cn_{\omega_2}} d_{\text{eff}} E_1(z) E_3^*(z) e^{i\Delta kz}, \\ \frac{d}{dz} E_3(z) &= -2i \frac{\omega_3}{cn_{\omega_3}} d_{\text{eff}} E_1(z) E_2(z) e^{i\Delta kz}, \end{aligned} \quad (4.18)$$

where $\Delta k = k_3 - k_1 - k_2$.

In the case of second harmonic generation (SHG), $\omega_1 = \omega_2 = \omega$, and $\omega_3 = 2\omega$. So the wave equations for SHG can be reduced to

$$\begin{aligned} \frac{d}{dz} E_{\text{FUN}}(z) &= -2i \frac{\omega}{cn_{\omega}} d_{\text{eff}} E_{\text{FUN}}^*(z) E_{\text{SHG}}(z) e^{-i\Delta kz}, \\ \frac{d}{dz} E_{\text{SHG}}(z) &= -4i \frac{\omega}{cn_{2\omega}} d_{\text{eff}} (E_{\text{FUN}}(z))^2 e^{i\Delta kz}, \end{aligned} \quad (4.19)$$

where $\Delta k = k_{2\omega} - 2k_{\omega}$.

Let's assume that the depletion of the fundamental wave (E_{FUN}) is negligible due to the low conversion efficiency in SH processes. Then the amplitude of $E_{\text{FUN}}(z)$ can be regarded to be constant. After integration over the interaction length of L_c , the amplitude of the SH wave can be expressed by

$$E_{\text{SHG}} = i4\omega \frac{d_{\text{eff}}}{cn_{2\omega}} L_c (E_{\text{FUN}})^2 \frac{e^{i\Delta k L_c} - 1}{i\Delta k L_c}. \quad (4.20)$$

Using the expression $I = 1/2nc\epsilon_0 |E|^2$, one can obtain the intensity of the second harmonic wave and the conversion efficiency as

$$\begin{aligned}
I_{\text{SHG}} &= \frac{32d_{\text{eff}}^2\omega^2}{c^3n_{2\omega}n_{\omega}^2\epsilon_0}L_c^2I_{\text{FUN}}^2\frac{\sin^2\frac{\Delta kL_c}{2}}{\frac{\Delta kL_c}{2}} \\
&= \Gamma_{\text{single}}L_c^2I_{\text{FUN}}^2\text{sinc}^2\left(\frac{\Delta kL_c}{2}\right), \\
\frac{P_{\text{SHG}}}{P_{\text{FUN}}} &= \Gamma_{\text{single}}L_c^2\frac{P_{\text{FUN}}}{A}\text{sinc}^2\left(\frac{\Delta kL_c}{2}\right),
\end{aligned} \tag{4.21}$$

where Γ_{single} is the single pass conversion coefficient, A is the area of the beam. The second harmonic intensity is proportional to the square of the fundamental intensity and also the square of the interaction length. The SH process is maximized when $\Delta kL_c = 0$, the so called phase matching condition. In other words

$$n_{\omega} = n_{2\omega}, \tag{4.22}$$

in which constructive interference between the fundamental and second harmonic wave occurs in a nonlinear medium.

As mentioned above, I_{FUN} is proportional to the square of the interaction length. This fact holds only for true planar waves. Usually a focused Gaussian beam is employed in the experiment. When a Gaussian beam is focused satisfying the confocal condition $L_c = 2z_0$, the area of the fundamental beam becomes πw_0^2 , where $w_0^2 = \lambda_{\omega}L_c/(2\pi n_{\omega})$. Under these conditions, the conversion efficiency is

$$\begin{aligned}
\frac{P_{\text{SHG}}}{P_{\text{FUN}}} &= \frac{32d_{\text{eff}}^2\omega^3}{c^4n_{2\omega}n_{\omega}\epsilon_0}L_cP_{\text{FUN}}\text{sinc}^2\left(\frac{\Delta kL_c}{2}\right), \\
&= \Gamma_{\text{single}}^G L_c P_{\text{FUN}} \text{sinc}^2\left(\frac{\Delta kL_c}{2}\right),
\end{aligned} \tag{4.23}$$

where Γ_{single}^G is the single pass conversion coefficient in the case of a focused Gaussian beam. The conversion efficiency in the case of a focused Gaussian beam is proportional to the interaction length L_c , not the square of it.

Let's consider sum frequency generation. For simplification, a strong pumping field ($E_2 \gg E_1$) and a perfect phase matching condition ($\Delta k = 0$) is assumed. Then Eq. (4.18) can be simplified to

$$\begin{aligned}
\frac{d}{dz}E_{\text{SUM}}(z) &= -i2\frac{\omega_{\text{SUM}}d_{\text{eff}}}{cn_{\omega_{\text{SUM}}}}E_1(z)E_2 = i\kappa_{\text{SUM}}E_1(z)E_2, \\
\frac{d}{dz}E_1(z) &= -i2\frac{\omega_1d_{\text{eff}}}{cn_{\omega_1}}E_2^*E_{\text{SUM}}(z) = i\kappa_1E_2^*E_{\text{SUM}}(z).
\end{aligned} \tag{4.24}$$

The solution of Eq. (4.24) is

$$\begin{aligned}
E_{\text{SUM}}(z) &= E_1(0) \cos\left(\sqrt{\kappa_1\kappa_{\text{SUM}}|E_2|^2}z\right), \\
E_1(z) &= E_1(0) \sqrt{\frac{\kappa_1}{\kappa_{\text{SUM}}}} \sin\left(\sqrt{\kappa_1\kappa_{\text{SUM}}|E_2|^2}z\right),
\end{aligned} \tag{4.25}$$

and the intensity can be expressed by

$$\begin{aligned} I_{\text{SUM}}(z) &= I_1(0) \cos \left(\sqrt{\kappa_1 \kappa_{\text{SUM}}} |E_2|^2 z \right), \\ I_1(z) &= I_1(0) \frac{n_{\omega_{\text{SUM}}} \omega_1}{n_{\omega_1} \omega_{\text{SUM}}} \sin \left(\sqrt{\kappa_1 \kappa_{\text{SUM}}} |E_2|^2 z \right). \end{aligned} \quad (4.26)$$

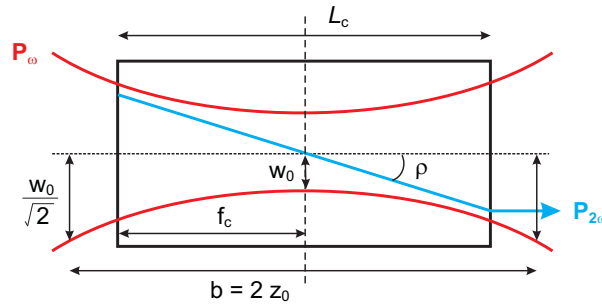


Figure 4.12: Gaussian beam in a nonlinear crystal. The fundamental wave (red trace) generates the second harmonic beam (blue trace). Due to the walk-off, the propagation of the blue and the red beam is not corresponding. L_c : the length of a nonlinear crystal; z_0 : Rayleigh length; b : confocal parameter; w_0 : beam waist in the crystal; ρ : walk-off angle; f_c : focal length.

Up to now, a simple theory on nonlinear frequency conversions based on coupled wave equations has been overviewed. A detailed theory on optical mixing processes employing a focussed Gaussian beam has been developed by Boyd and Kleinmann (BK) [48]. The BK theory predicts the optimal focusing condition considering a give-and-take between the intensity of the light beam and the interaction length. According to the BK theory, single pass conversion efficiencies for SHG and SFG are given by

$$\begin{aligned} \gamma_{\text{SHG}} &= \frac{P_{\text{SHG}}}{P_\omega^2} = \frac{2\omega^2 k_\omega}{\pi n_\omega^3 \epsilon_0 c^3} d_{\text{eff}}^2 L_c h(\sigma, B, a, \xi, f), \\ \gamma_{\text{SFG}} &= \frac{P_{\text{SFG}}}{P_1 P_2} = \frac{8\omega_1 \omega_2 k_0}{\pi n_1 n_2 n_{\text{SUM}} \epsilon_0 c^3} d_{\text{eff}}^2 L_c h(\sigma, B, a, \xi, f), \end{aligned} \quad (4.27)$$

where $k_0 = n_0 \omega_0 / c$, $n_0 = (n_1 + n_2) / 2$, $k_0 = (k_1 + k_2) / 2$. The Boyd-Kleinmann factor is given by

$$h(\sigma, B, a, \xi, f) = \frac{1}{2\xi} \int_{-f}^{\xi-f} \int_{-f}^{\xi-f} d\tau d\tau' \frac{\text{Exp} \left(-a(\tau + \tau' + 2f) - i\sigma(\tau - \tau') - \beta^2(\tau - \tau')^2 \right)}{(1 + i\tau)(1 - i\tau')}, \quad (4.28)$$

where

$$\begin{aligned}
 \sigma &= \Delta k z_0, \\
 \beta &= B \sqrt{2/\xi}, \\
 B &= \rho \frac{L_c k \omega}{2}, \\
 a &= (\alpha_1 - \alpha_2/2) z_0, \\
 \xi &= L_c / z_0, \\
 f &= f_c / z_0.
 \end{aligned} \tag{4.29}$$

Here σ is the phase mismatching parameter, β is the double refraction, B is the double refraction parameter, ρ is the walk-off angle, a is the absorption, ξ is the focusing parameter, and z_0 is the Rayleigh length. In the optimal focal position, the absorption a is negligible, and the focal length f is set to be $2L_c$. The interesting point in the theory is that perfect phase matching in a Gaussian beam is not the optimal condition anymore. The optimal phase mismatching parameter, σ_m , is not "0" any more. Fig. 4.13 shows the calculated Boyd-Kleinmann factors depending on various double refraction parameters using a mathematica program [49].

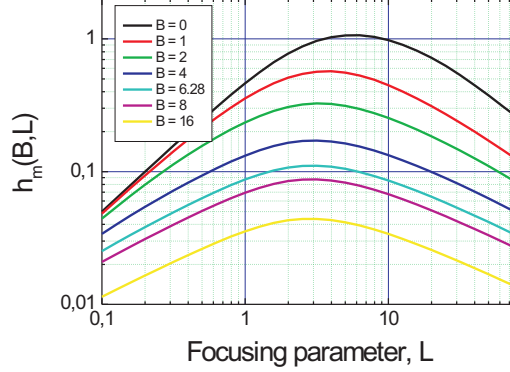


Figure 4.13: Calculated Boyd-Kleinmann factors depending on various double refraction parameters.

Equation (4.28) is very complicated and it takes much time to calculate. For convenience, one can use an approximated form of an optimum BK factor and an optimum focusing parameter written as [50]

$$\begin{aligned}
 h_m(B) &= \frac{0.27163}{1 + 0.339B} + \frac{1.0517}{1 + 1.00008B^2} - \frac{0.25563}{1 + 0.59847B^3}, \\
 \xi_m(B) &= 2.7517 + \frac{0.62204}{1 + 0.39218B} + \frac{2.49362}{1 + 3.2012B^2}.
 \end{aligned} \tag{4.30}$$

The accuracy of Eq. (4.30) is 10^{-2} for $0.1 \leq B \leq 10$. Both of Eq. (4.28) and Eq. (4.30) give us the same value of the BK factor of 0.111 for the BIBO crystal in the experiment. From the optimum focusing parameter, ξ_m , one can deduce an optimum waist in a nonlinear crystal. The calculated optimum focusing parameters using Eq. (4.30) are shown in Fig. 4.14.

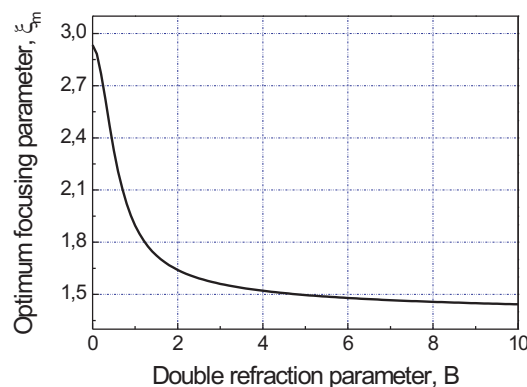


Figure 4.14: The calculated optimum focusing parameter as a function of the double refraction parameter.

4.2.2 Nonlinear crystals for frequency upconversions

In this experiment, three nonlinear crystals (BIBO, LBO, KNbO₃) have been used for the SHG, and a BBO is employed for SFG. To select an appropriate nonlinear crystal for the experiment, two important requirements should be fulfilled. Firstly, the beam profile of the blue beam should be good because the blue light generated by SHG process is coupled into a doubly resonant cavity (DRC). Due to this fact, a crystal with small walk-off angle is necessary. Secondly, a crystal should have a large effective nonlinear coefficient (d_{eff}) to obtain high conversion efficiency.

A BIBO crystal was selected for the first crystal because it has higher d_{eff} than that of BBO and LBO crystal. But due to a relatively large walk-off, the beam profile is not so good to be coupled into a DRC. The mode matching efficiency was measured to be only 20 % although the SH power was more than 300 mW. This will be discussed later. The second crystal was a Brewster cut LBO crystal. A Brewster cut crystal provides very low linear loss (≤ 0.5 %). A critically phase-matched LBO crystal has a relatively small walk-off, and the mode matching efficiency to the DRC was measured to be around 50 %. But, as the fundamental power from the FAs was degraded due to the burning of the fiber, SH power was decreased down to 50 mW. So the LBO crystal was not suitable for the low fundamental power any more. A KNbO₃ crystal has a large d_{eff} and also a very small walk-off, which is the combination of advantages of the BIBO and LBO crystals.

Using the KNbO₃ crystal, the SH power and the mode matching efficiency are 150 mW and 60 %, respectively.

A BBO crystal is employed for SFG process. This crystal has a larger d_{eff} than a LBO and is transparent in the UV region including the third harmonic frequency at 325 nm. Table 4.2 and 4.3 show the summary of characters, advantages and disadvantages of the used crystals.

	BIBO	LBO	KNbO ₃
Crystal class	negative biaxial	negative biaxial	negative biaxial
d_{eff} (pV/m)	3.25	0.82	9.4
ρ (mrad)	37	10	6.7
Refractive indices	1.796	1.607	2.227
Phase matching type	e + e → o	o + o → e	e + e → o
θ, φ (Deg)	164, 90	90, 17	11.5, 90
Dimensions(mm ³)	3 × 3 × 10	3 × 3 × 10	2 × 1.8 × 5
Advantages	large d_{eff}	small ρ	large d_{eff} and small ρ
Disadvantages	poor beam quality	small d_{eff}	easy to be broken

Table 4.2: Summary of the important parameters of nonlinear crystals for SHG. θ is the angle between the \vec{k}_ω and the optical axis (Z) of the crystal, and ϕ is the azimuthal angle of the wavevector on the XY plane of the crystal.

	BBO
Crystal class	negative uniaxial
d_{eff} (pV/m)	2
Walk-off angle(mrad)	77
Refractive indices	1.656 @ 977 nm, 1.678 @ 488 nm
Phase matching type	o + o → e
θ (Deg)	34.5
Dimensions(mm ³)	3 × 3 × 10

Table 4.3: Summary of the important parameters of BBO for SFG.

4.2.3 Second harmonic generation in external cavities

Due to the low single-pass conversion efficiency in nonlinear frequency upconversions, a conventional method to overcome this problem is to use an enhancement cavity. One can build up the optical power of the fundamental wave up to several tens or even hundreds of Watt using an external cavity.

Cavity design

To design a cavity appropriately, an ABCD matrix approach is necessary to estimate the waist sizes in a cavity. The matrix elements of the ABCD matrix are presented

elsewhere [51]. Figure 4.15 shows a model of the cavity geometry including a pair of curved mirrors and a pair of flat mirrors, a so-called bow-tie shape, used in the calculation of the ABCD matrix. A nonlinear crystal is placed in the middle of the two curved mirrors. Special care is required to design a cavity including a Brewster cut crystal [52]. The angle of incidence should be chosen to compensate the astigmatism caused by the crystal Brewster surfaces. The special angle is given by [52]

$$R_c \tan \theta \sin \theta = L_c(n_\omega^2 - 1)/n_\omega^3, \quad (4.31)$$

where R_c is the radius of curvature of the curved mirrors, θ is the angle of incidence, and L_c is the length of the crystal. The geometrical parameters for the cavities for SHG are summarized in Tab. 4.4.

	BIBO	LBO	KNbO ₃
L (mm)	58	58.4	56.2
l_1 (mm)	101	124	119
l (mm)	127	153	161
θ (Deg)	12	15.7	12
L_T (mm)	388	458.4	456.2
w_{01}^t (μm)	25.6	36	22.3
w_{01}^s (μm)	25.3	24	23.2
w_{02}^t (μm)	199	279	185
w_{02}^s (μm)	270	180	234

Table 4.4: Summary of the cavity parameters for SHG. L_T is a total length of resonators.

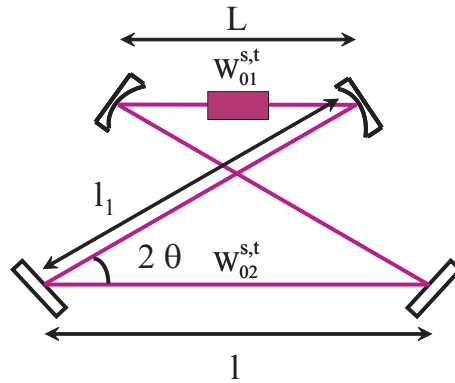


Figure 4.15: Cavity geometry used in the calculation of ABCD matrix. Two waists exist, one (w_{01}) is between the two curved mirrors, another (w_{02}) is between the two flat mirrors.

Figure 4.16 shows the calculated waist size of each cavity. In the cases of Fig. 4.16(a) and (c), the distance between the two curved mirrors is determined to the crossing point at which both of the tangential and sagittal modes meet with each other. In the case of Fig. 4.16(b), the distance L is chosen at the center point of the tangential beam waist.

The astigmatism in the cavity including a Brewster cut LBO crystal cannot be perfectly compensated because the astigmatism inside the crystal cannot be compensated even in the condition, Eq. (4.31) as shown in Fig. 4.16(b). One can insert several optics, for instance, cylindrical lenses to compensate the aberrations, but the linear loss in the cavity will be increased.

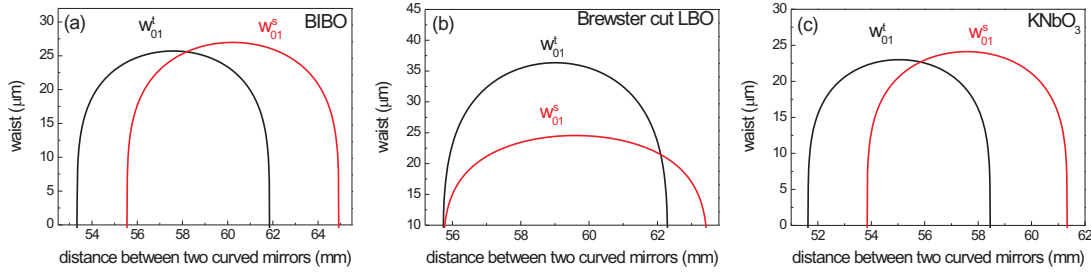


Figure 4.16: Waists of the cavities including a BIBO, a Brewster cut LBO, and a KNbO_3 crystal.

Mode matching

The beam mode from the YDCFA's should be well matched into the cavity eigen mode otherwise the unmatched mode is simply reflected by the resonator. In the experiment, two lenses are employed for the mode matching. One is a small collimating lens with short focal length ($f = 5.0$ mm), and the other is a 1 inch lens with focal length of 300 mm. The distances between the lenses and the resonator can be deduced by a simple ray matrix model. The distance between the fiber and the small collimating lens can be finely and easily varied by a mechanical translation stage attached to the fiber holder.

Locking scheme for the cavity

An external cavity for frequency upconversion is required to be resonant with the frequency of the fundamental wave to build up the power of the fundamental light. The most widely used method to lock a cavity is the Hänsch-Couillaud method [53]. The key idea of this method is to remove the ellipticity induced by a slight off-resonance of the cavity. The polarization of the input light consists of p- and s-polarization. For convenience, let's assume that only p-polarization is resonant with the cavity. Then the s-polarized component is reflected at the input coupler, and the p-polarized component is transmitted through the input coupler after circulating the resonator. Depending on the resonance conditions, the p-polarized light experiences a certain phase shift inside the cavity to form elliptical polarization together with the reflected s-polarized light. In exact resonance, there is no phase shift yielding linear polarization. A detector consisting of a quarter wave plate and a polarizer detects the ellipticity of the fundamental light. Depending on the sign of the phase shift of the p-polarized light, the detector gives a plus or a minus sign which acts as an error signal. A servo electronics which is connected to a piezo transducer

to control the length of the cavity keeps the phase shift zero and sustains resonance. This method is very easy to be realized and also economic. Only a quarter wave plate and a polarization beam splitter cube are needed.

Theory on second harmonic generation in an external cavity

The power of the second harmonic light can be expressed by [54]

$$P_{\text{SHG}} = \gamma_{\text{SHG}} P_{\text{cir},\omega}^2 = \frac{16 \kappa_{\text{eff}} (1 - R)^2 \gamma_{\text{SHG}}}{\left[2 - \sqrt{R} (2 - \delta_{\text{L}} - \sqrt{\gamma_{\text{SHG}} P_{\text{SHG}}})\right]^4} P_{\text{in},\omega}^2, \quad (4.32)$$

where κ_{eff} is the effective mode matching efficiency, γ_{SHG} is the single-pass conversion efficiency, R is the reflectance of the input mirror, δ_{L} is the linear loss of the cavity, and $P_{\text{in},\omega}$ is the input power at the fundamental frequency. The optimum transmittance of the input mirror considering the impedance matching is given by

$$T_{\text{opt}} = \frac{\delta_0}{2} + \sqrt{\frac{\delta_0^2}{4} + \gamma_{\text{SHG}} P_{\text{SHG}}}. \quad (4.33)$$

In the perfect impedance matching case, there is no reflected beam from the cavity due to the destructive interference between the reflected and transmitted beam from the cavity. The total loss of the cavity, δ_{T} , can be estimated by measuring the power of the reflected beam and the circulating beam. After simple algebraic manipulations of power equations of a cavity, one can obtain

$$\delta_{\text{T}} = \delta_{\text{L}} + \delta_{\text{NL}} = \delta_{\text{L}} + \gamma_{\text{SHG}} P_{\text{cir},\omega} = \frac{P_{\text{in},\omega} - P_{\text{ref},\omega}}{P_{\text{cir},\omega}}, \quad (4.34)$$

where $P_{\text{cir},\omega}$ is the circulating power which is easily estimated by measuring the leaking power from the cavity. One can know the nonlinear loss by measuring the second harmonic power, then the linear loss in the cavity can be deduced by Eq. (4.34). Using Eq. (4.32), the effective mode matching coefficient can be calculated. So by measuring the second harmonic, the circulating, and the reflected powers, the whole cavity parameters can be deduced.

Second harmonic generation in an external cavity

Figure 4.17 shows the SH power as a function of the input power in the case of BIBO (a) and a Brewster cut LBO (b) crystals. The BIBO cavity produces more than 300 mW blue light, and the theory and the experiment are in good agreement. The LBO cavity generates 120 mW blue power and the enhancement factor is measured to be 95. The 160 mW blue power is obtained from the KNbO₃ cavity with only 450 mW input power, which is the highest conversion efficiency. The SH power dependence on the input power in the KNbO₃ cavity is not obtained. The measured cavity parameters are shown in Tab. 4.5.

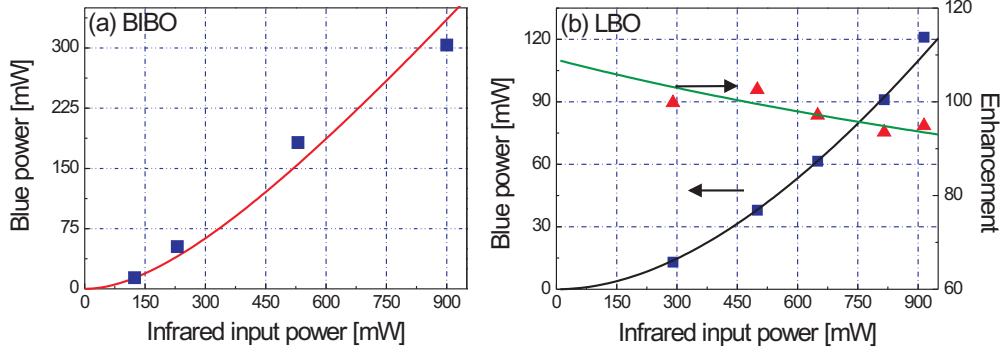


Figure 4.17: Second harmonic power from the cavities including (a) a BIBO and (b) a Brewster cut LBO as a function of the input power at λ_ω .

	BIBO	LBO	KNbO ₃
Experimental γ_{SHG} (W ⁻¹)	1.5×10^{-4}	2×10^{-5}	1.1×10^{-3}
Theoretical γ_{SHG} (W ⁻¹)	2.4×10^{-4}	4.4×10^{-5}	5.8×10^{-3}
δ_L (%)	0.82	0.44	0.55
κ_{eff} (%)	82	74	61
Overall conversion efficiency (%)	33	13	36

Table 4.5: Summary of the SH cavity parameters.

The beam profiles of the blue light from each cavity are shown in Fig. 4.18. In the beam profile of the blue light from the BIBO cavity as shown in Fig. 4.18(a), one can see clearly 3 parts due to the severe walk-off. One of these parts could be coupled to the DRC. The coupling efficiency was measured to be only 20 %. So the BIBO crystal was replaced by a Brewster cut LBO crystal which has a four times smaller ρ than that of BIBO. Figure 4.18(b) and (c) show the beam profile of the blue and infrared beams, respectively. The beam profile of the blue beam from the LBO cavity looks like an ellipse, and the ratio of the width in the vertical to transversal direction is 0.33 which can be easily compensated by a cylindrical lens pair. The beam profile of the transmitted fundamental beam looks almost circular as shown in Fig. 4.18(c). The ratio of the width in the vertical to transversal directions of the infrared beam is 0.97. So the astigmatism at the Brewster surface is almost compensated. The blue beam profile from the KNbO₃ cavity looks almost circular. The ratio of the vertical to horizontal directions is measured to be 1.06.

4.2.4 Sum frequency generation in an external cavity

Theory on sum frequency generation in an external cavity

A theory on sum frequency generation in an external cavity is well established in Ref. [55]. It is just a simple extension of the theory on the SHG in a cavity. The power generated

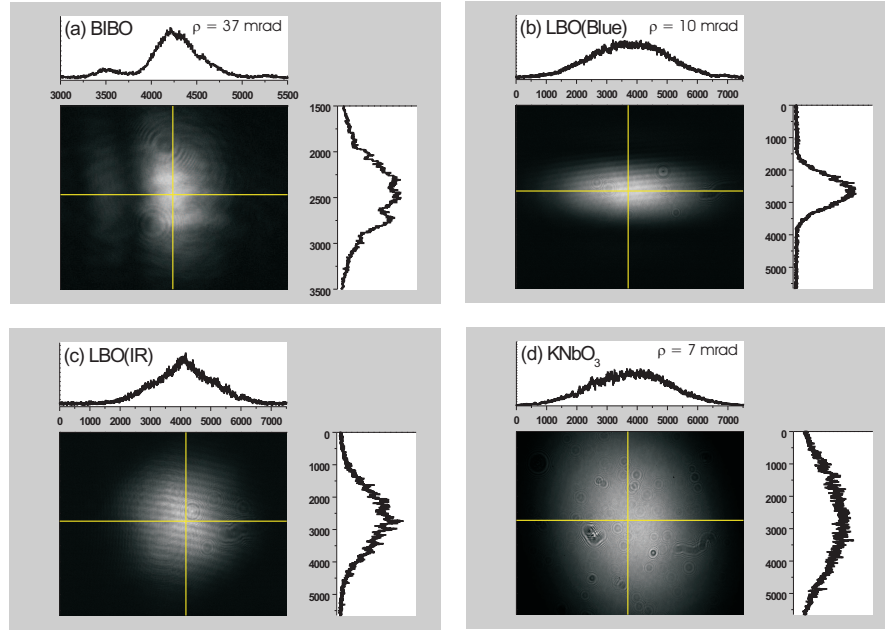


Figure 4.18: The beam profiles of the blue beam from (a) BIBO, (b) Brewster cut LBO, (d) KNbO₃ cavities and (c) the beam profile of the infrared beam from the astigmatism-compensated cavity. The elongated shape in the blue beam profile results from walk-off. In the profile (c), the astigmatism for the infrared light is substantially suppressed.

by sum frequency generation process in an external cavity can be expressed by

$$P_{\text{SFG}} = \gamma_{\text{SFG}} P_{c, \omega_1} P_{c, \omega_2}, \quad (4.35)$$

where P_{c, ω_i} is the circulating power at the frequency ω_i . The nonlinear loss in the sum frequency generation can be obtained by

$$\begin{aligned} \delta_{\text{NL},1} &= \frac{\omega_1}{\omega_1 + \omega_2} \gamma_{\text{SFG}} P_{c, \omega_2}, \\ \delta_{\text{NL},2} &= \frac{\omega_2}{\omega_1 + \omega_2} \gamma_{\text{SFG}} P_{c, \omega_1}, \end{aligned} \quad (4.36)$$

Equation 4.36 indicates that the nonlinear loss is dependent on the frequency. The round trip loss for each frequency is given by

$$\begin{aligned} R_{m,1} &= 1 - (\delta_{L,1} + \delta_{\text{NL},1}), \\ R_{m,2} &= 1 - (\delta_{L,2} + \delta_{\text{NL},2}), \end{aligned} \quad (4.37)$$

where $\delta_{L,i}$ is the linear loss in the cavity at frequency ω_i . The circulating power inside the cavity at each frequency can be written as

$$\begin{aligned} P_{c, \omega_1} &= \frac{\kappa_{\text{eff}, \omega_1} (1 - R_{\omega_1})}{(1 - \sqrt{R_{\omega_1} R_{m,1}})^2} P_{\text{in}, \omega_1}, \\ P_{c, \omega_2} &= \frac{\kappa_{\text{eff}, \omega_2} (1 - R_{\omega_2})}{(1 - \sqrt{R_{\omega_2} R_{m,2}})^2} P_{\text{in}, \omega_2}, \end{aligned} \quad (4.38)$$

where $\kappa_{\text{eff}, \omega_i}$ is the mode matching efficiency of the beam at the frequency ω_i , R_{ω_i} is the reflectance of the input coupler at the frequency ω_i , and P_{in, ω_i} is the input power at the frequency ω_i . Using Eq. (4.35) and Eq. (4.38), one can easily obtain the expected SFG power.

4.3 Third harmonic generation in a doubly resonant cavity

Third harmonic generation is based on the frequency upconversion of $\lambda_{2\omega}$ light from the EC1 and another λ_ω beam from FA2 [56, 57]. The blue light beam at $\lambda_{2\omega}$ from the first enhancement cavity (EC1) and the second infrared light beam at λ_ω from FA2 are combined by a dichroic mirror and then coupled to the second bow-tie shaped cavity through mode matching lenses as shown at the bottom right corner of Fig. 4.6. Here a 10-mm-long type-I phase-matched β -BaB₂O₄ (BBO) crystal was chosen, since it has high transmission at UV wavelengths. Both of the facets of the BBO crystal are antireflection coated for λ_ω , $\lambda_{2\omega}$ and $\lambda_{3\omega}$ light. The input coupler M5 has 98.5 % reflectivity at λ_ω and 97 % reflectivity at $\lambda_{2\omega}$. A small mirror M6 is mounted on a low-voltage PZT to keep the cavity resonant. The output coupler M8 has high reflectivity for λ_ω , $\lambda_{2\omega}$, and 87 % transmission for $\lambda_{3\omega}$. The radii of curvature of the curved mirrors M7 and M8 are -75 mm. The distance between the mirrors is optimized for maximum conversion efficiency. The angle of incidence of the second cavity is 12°. The waist is calculated to be 43 μm for λ_ω and 24 μm for $\lambda_{2\omega}$ light yielding the ratio 1.79. Considering the optimal beam waist, the ratio of the beam waists of both fundamental beams in a doubly resonant cavity $w_\omega/w_{2\omega} = \sqrt{2n_{2\omega}/n_\omega}$ is calculated to be 1.42 which is comparable to the designed value. To maintain the second cavity simultaneously resonant with the λ_ω and $\lambda_{2\omega}$ wavelengths, two steps are used [57]. The length of EC2 is locked to the λ_ω wavelength using the Hänsch-Couillaud method [53]. A small optical path length difference (OPD) between λ_ω and $\lambda_{2\omega}$ caused by dispersion in the cavity is compensated by slightly rotating two quartz plates mounted at Brewster's angle. The thickness of each plate is 2 mm and tuning the angle by $\pm 0.2^\circ$ can cover 250 nm OPD corresponding to about half the wavelength of $\lambda_{2\omega}$. The quartz plates are mounted on counter rotating galvo motors and dithered at 270 Hz. Phase sensitive detection of the blue light at $\lambda_{2\omega}$ leaking from M7 allows us to derive an error signal for compensating cavity dispersion, so that EC2 is resonant for the blue wavelength $\lambda_{2\omega}$, too. The experimental values of the third harmonic power at $\lambda_{3\omega}$ as a function of the input power at λ_ω are shown in Fig. 4.19. The maximum third harmonic power at $\lambda_{3\omega}$ measured behind the output coupler M8 is 12 mW for 405 mW at λ_ω and 120 mW at $\lambda_{2\omega}$, respectively. The measured circulating powers are 26 W for

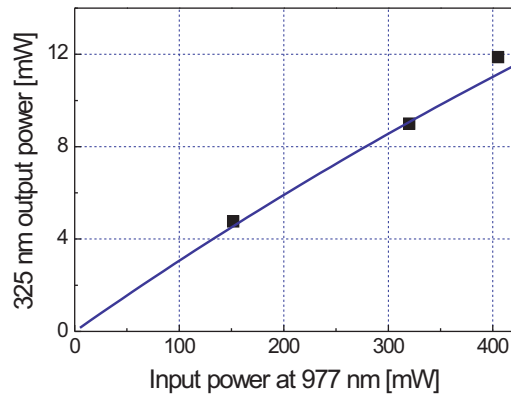


Figure 4.19: Experimental (rectangles) and theoretical (solid line) third harmonic power at 325 nm as a function of the input power at 977 nm. Blue light power at 488 nm is fixed at 120 mW.

λ_ω and 2.4 W for $\lambda_{2\omega}$. The estimated single-pass conversion efficiency is $2.2 \times 10^{-4} \text{ W}^{-1}$, which is 88 % of the calculated value. By measuring the rejected power of the blue and infrared beam from EC2, the linear losses are estimated to be 1.23 % for λ_ω and 2 % for $\lambda_{2\omega}$. The mode-matching efficiencies are calculated to be 80 % for λ_ω and 49 % for $\lambda_{2\omega}$. The overall conversion efficiency is 2.3 %, and the internal efficiency with respect to the coupled fundamental waves is 3.6 %. The result of a theoretical calculation [55] of the UV power based on the measured parameters is shown in the solid line in Fig. 4.19, and the theory agrees well with the experimental result. The mode-hop free tuning range of UV light is more than 18 GHz.

As the fibers burned from time to time, the power of the FAs and the SG power have been degraded. After replacing the LBO with a KNbO_3 crystal, the SH power was increased up to 160 mW with the conversion efficiency of 36 %. The better effective mode matching efficiency was obtained to be ≥ 60 %, and the UV power at 326 nm was measured to be 12 mW again.

4.3.1 Linear spectroscopy of the $5P_{3/2} \rightarrow 5D_{5/2}$ transition of Indium in a hollow cathode lamp

The $5P_{3/2} \rightarrow 5D_{5/2}$ transitions are found by linear absorption spectroscopy of Indium in a commercial hollow cathode lamp (HCL) using UV light at $\lambda_{3\omega}$ as shown in Fig. 4.20. The amplitude modulated 300 nW UV beam passes through a commercial hollow cathode lamp (Cathodeon, 3QQNY/In, Ne buffer gas, 6 Torr). A PMT detects the transmission of the UV light while the frequency of the seed laser at λ_ω is scanned across the resonance. The demodulated signal by a lock-in amplifier (LIA) is recorded by an oscilloscope together with the transmission peaks of a 1.5-GHz Fabry-Perot interferometer injected by the seed beam for frequency calibration. The absorption is observed at $\lambda_\omega = 976.837 \text{ nm}$ in air.

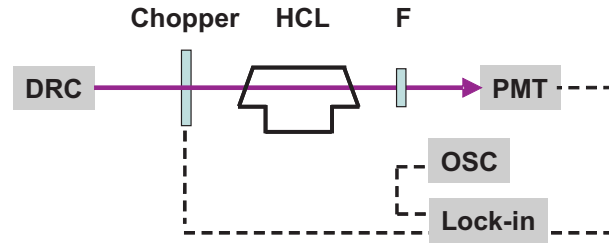


Figure 4.20: Experimental setup for the linear absorption spectroscopy of Indium using UV light at λ_{cool} . The dotted lines indicate the electrical connections.

This value is not the same as $3 \times 325.609 \text{ nm}$. The deviation between them can be attributed to the difference of the refractive index of the air at IR and UV region.

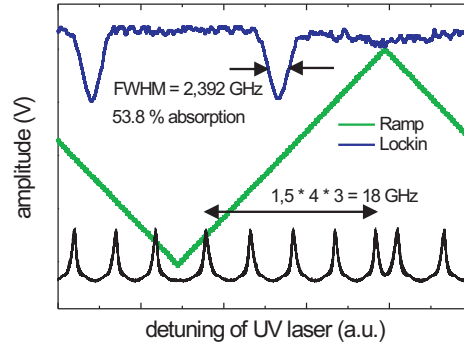


Figure 4.21: An example of the absorption of the UV beam at $\lambda_{3\omega}$.

Figure 4.21 shows the LIA signal (blue), the transmission of a 1.5 GHz Fabry-Perot cavity (black), and the ramp signal for the frequency scanning (green). The drive current of the HCL is 10 mA. The FWHM of the observed spectra is measured to be 2.4 GHz contributed to by each hyperfine transition. The FWHM of the transmission spectra is measured as a function of the applied current to deduce the temperature in the cell. The measured spectra is fitted by the sum of Gaussians of each hyperfine transitions, and the deduced width of a hyperfine transition is directly converted into the cell temperature as shown in Fig. 4.22.

4.4 Conclusion

In summary, we have developed a tunable single-mode UV source at $\lambda_{3\omega}$. Two FAs using a single seed laser were built to generate 1 W (FA1) and 0.4 W (FA2) fundamental power for nonlinear frequency conversion. The output of FA1 was frequency doubled in a cavity to generate 120 mW blue light at $\lambda_{2\omega}$. To generate UV light at $\lambda_{3\omega}$ through third harmonic generation, the output of FA2 and the second harmonic light beam at $\lambda_{2\omega}$ were coupled

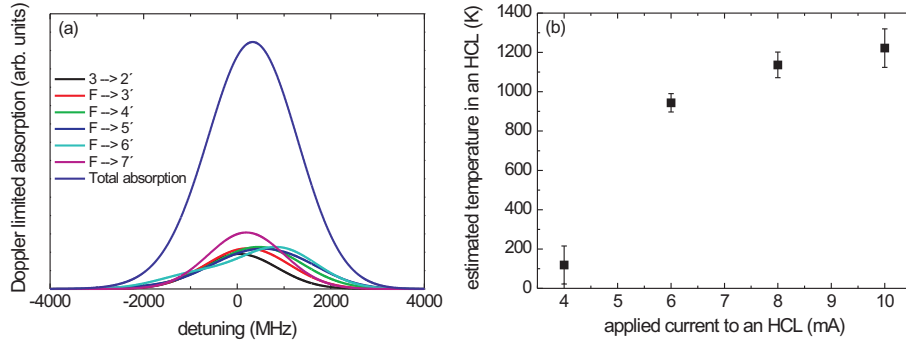


Figure 4.22: (a) An example of fitted spectra. (b) The deduced temperature of the HCL as a function of the applied current.

into the second cavity which was doubly resonant with both λ_ω and $\lambda_{2\omega}$ wavelengths. We have obtained 12 mW UV light at $\lambda_{3\omega}$ and tuned the UV laser frequency continuously more than 18 GHz. A strong linear absorption of the $5P_{3/2} \rightarrow 5D_{5/2}$ state was observed using the developed UV laser at $\lambda_{3\omega}$.

Realistic improvements of our system include a longer fiber for FA2 (1 W instead of 0.4 W) and a reduction of intracavity loss in EC1 (400 mW instead of 120 mW at $\lambda_{2\omega}$). Then we should approach 100 mW output power at $\lambda_{3\omega} = 326$ nm. Already with the current setup a UV light source suitable for laser cooling of Indium with the $5P_{3/2}$ - $5D_{5/2}$ closed transition is available.

Chapter 5

Efficient laser cooling of an Indium atomic beam

I present efficient sub-Doppler laser cooling of an In atomic beam on a UV cycling transition at 325.6 nm. The transverse velocity of the atomic beam is reduced to 13.5 ± 3.8 cm/s, well below the Doppler cooling limit. The fraction of laser-cooled In atoms is enhanced to 12 ± 3 % by optical pumping in the present experiment. It can be scaled up to approach almost 100 % efficiency in cooling, providing high brightness atomic beams for further applications.

5.1 Experimental apparatus

Light sources

For the present laser cooling scheme three different light sources are required, a blue beam for probing, a violet beam for optical pumping, and a UV beam for laser cooling.

Blue light at $\lambda_{\text{probe}} = 451$ nm is generated by a frequency-doubled Ti:sapphire laser. The output power of 0.5 mW is produced after a single-pass of the infrared beam at 902 nm through a periodically-poled KTP crystal. Since on excitation by the probe laser in the open $^2P_{3/2} \rightarrow ^2S_{1/2}$ transition every atom undergoes 1.2 fluorescence cycles on average only the fluorescence distribution is directly proportional to the atomic flux density.

The violet beams at $\lambda_{\text{pump}} = 410$ nm are provided by external cavity diode lasers, 4 mW for $4 \rightarrow 5$ and 2 mW for $5 \rightarrow 5$ transitions, respectively. Both of the violet beams are combined by a polarization beam splitter cube and have a dimension of 2 mm \times 1 mm resulting the interaction time 3.6 μ s for the 2 mm long interaction length. The frequencies of violet lasers are locked to each transition by a conventional saturated absorption spectroscopy using an ASC [26].

The cooling laser light at $\lambda_{\text{cool}} = 326$ nm is generated by upconversion of the output of two fiber amplifiers driven by a single diode laser at $3\lambda_{\text{cool}}$ [47]. A frequency doubling stage with a critically phase-matched KNbO₃ crystal is employed ($3\lambda_{\text{cool}} \rightarrow 3\lambda_{\text{cool}}/2$), and summation is achieved with a BBO crystal in a doubly resonant cavity ($(3\lambda_{\text{cool}})^{-1} + (3\lambda_{\text{cool}}/2)^{-1} \rightarrow \lambda_{\text{cool}}^{-1}$). The UV output light of the summation stage is collimated by a pair of cylindrical

lenses yielding a cross section of $1 \text{ mm} \times 3 \text{ mm}$ with 7 mW of UV power and corresponding to a saturation parameter ($s = 4.5$). The 3 mm interaction length with the atomic beam corresponds to an average interaction time of $\tau_{\text{int}} = 700 \tau$.

Vacuum system and Indium atomic beam

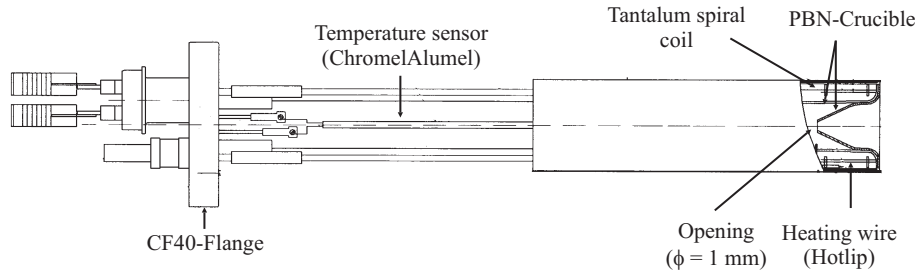


Figure 5.1: An oven for the generation of an Indium atomic beam.

The vacuum system consists of three different parts, an atomic oven to produce an atomic Indium beam, an interaction region where Indium atoms interact with pump beams and cooling beams, and a probe region where the transverse velocity distribution of atoms is investigated.

The vacuum pressure reaches 10^{-8} Torr by two turbo-molecular pumps (Turbo-V70 and Turbo-V250, Varian). An Indium atomic beam is produced by a commercial effusion cell (DFC-35/23-SH, CreaTec) with 2 heating wires as shown in Fig. 5.1. The Indium reservoir is located in a crucible made of pyrolytical Boron nitride (PBN) and heated up to $1200 \text{ }^\circ\text{C}$ with a Tantalum spiral coil. Another crucible with an opening of 1 mm diameter is placed on the crucible containing the Indium reservoir. This additional crucible is heated by an additional heating wire, a so called hotlip, up to a slightly higher temperature than that of the reservoir so that Indium cannot condensate at the rim of another crucible. Without the hotlip, the Indium condensate slides down from the rim and frequently clogs a small aperture of the second crucible, then the atomic Indium bursts and the condensate clogs the aperture again, and such a sequence is repeated. Eventually this process produces an atomic Indium beam pulse, not a continuous Indium atomic beam.

As shown in Fig. 5.2 a water-cooled copper shield with an opening of $1 \text{ mm} \times 5 \text{ mm}$ is located above the oven to minimize the amount of Indium deposited everywhere in the chamber. The Indium atomic beam is mechanically collimated by a mechanical aperture with a 0.5 mm diameter above the rectangular aperture. In the interaction region, a photo multiplier tube (PMT) detects the laser-induced fluorescence signal. At the distance of 611 mm above the cooling region, a CCD camera records images of the atomic fluorescence induced by the probe beam to investigate the velocity distribution of the Indium atomic beam at the probe region.

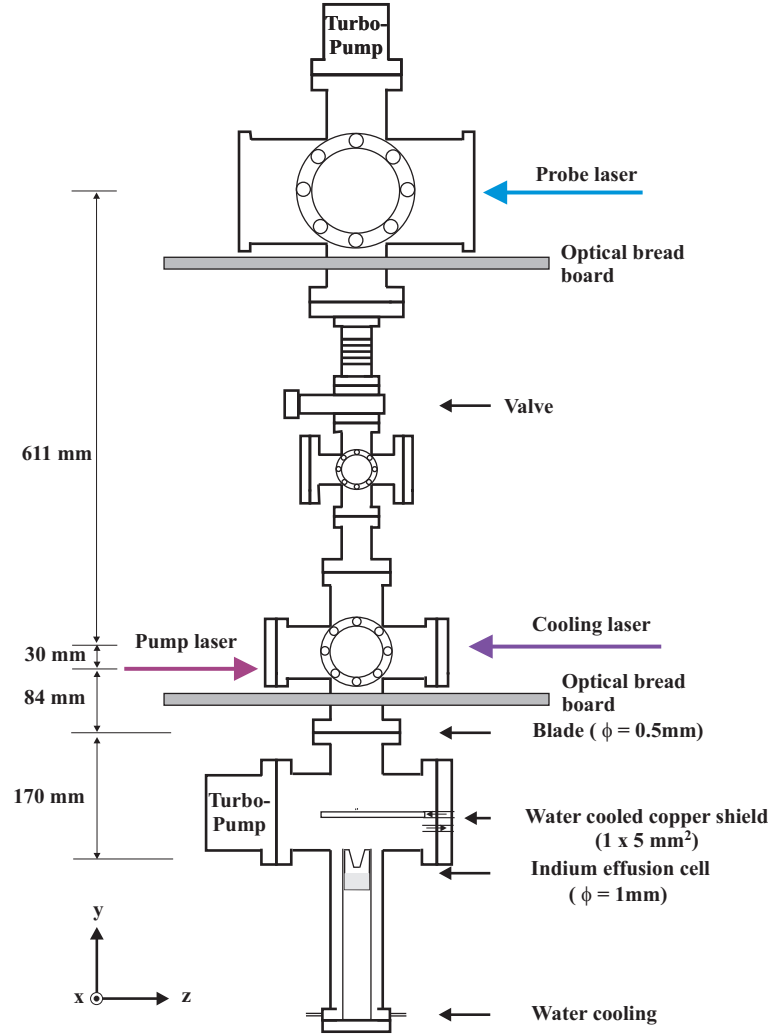


Figure 5.2: Schematics of the vacuum system.

The longitudinal velocity of an atomic beam is given by [59]

$$f(v_y) = \frac{v_y^3}{2\tilde{v}^4} \exp\left(-\frac{v_y^2}{2\tilde{v}^2}\right), \quad \text{where } \tilde{v} = \sqrt{\frac{k_B T}{m}} = \frac{v_{\text{mp}}}{\sqrt{3}}, \quad (5.1)$$

and k_B is the Boltzmann constant, m the mass of an atom, v_{mp} the most probable velocity. The most probable velocity of the Indium atomic beam at 1200 °C is calculated to be 560 m/s while the time-of-flight measurement of the velocity yields 530 ± 22 m/s [58]. Considering the geometry of the two apertures, the collimation ratio is calculated to be $\kappa = 4.4 \times 10^{-3}$ yielding the transverse velocity $v_t = v_z = \kappa v_{\text{mp}} = 2$ m/s.

Figure 5.3 shows images of the atomic beam and their integrated transverse intensity profile (a) in the cooling and (b) the probe region. The atomic beam is illuminated by a violet laser light at 410 nm whose frequency is locked to the $4 \rightarrow 5$ transition, and the

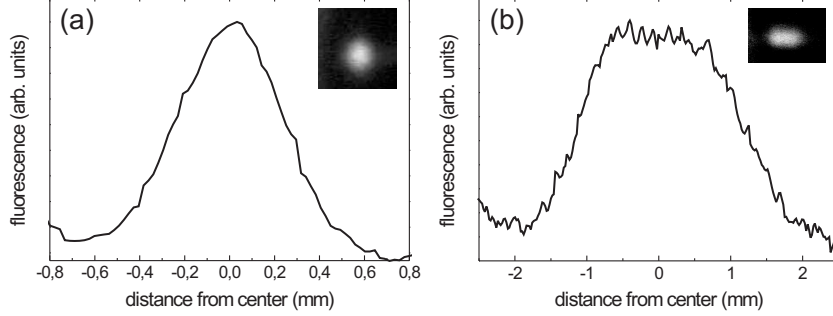


Figure 5.3: Images of the atomic beam and their integrated transverse profile (a) in the cooling and (b) the probe region. The FWHMs of the profile of the cooling and the probe region are measured to be 0.57 ± 0.01 and 2.36 mm, respectively.

fluorescence images are taken in the cooling region by CCD1 and in the probe region by CCD2. The FWHM of the integrated profile of the atomic beam in the cooling and the probe region is measured to be 0.57 ± 0.01 mm and 2.36 mm, respectively. According to the geometry of the vacuum setup, the full divergence angle of the atomic Indium beam is determined to be 2.93 ± 0.02 mrad yielding the transverse velocity of 1.64 ± 0.01 m/s which is a bit smaller than the expected velocity, 2.34 m/s. The difference between the theoretical collimation rate and the measured full divergence angle of the Indium atomic beam could be attributed to the clogging of the apertures so that the effective aperture becomes smaller. Table 5.1 shows several parameters relevant to laser cooling of Indium and our setup.

Parameter	Symbol	Value
Life time	τ	7.7 ns
Decay rate	Γ	$2\pi \times 20.7$ MHz
Doppler capture velocity	v_c	6.7 m/s
Recoil velocity	v_r	1.1 cm/s
Velocity at Doppler limit	v_D	19 cm/s
Recoil frequency	ω_r	$2\pi \times 16$ kHz
Cooling ratio	ϵ	7.9×10^{-4}
Saturation intensity	I_{sat}	78 mW/cm ²
Cooling beam diameter	z_1	3 mm
Free flight distance	l	611 mm
Longitudinal velocity	v_l	560 m/s
Beam divergence(FWHM)	θ	3 mrad
Interaction time	τ_{int}	$5.4 \mu\text{s} \sim 700 \tau$

Table 5.1: Atomic parameters of the cooling transition $^2P_{3/2}, F'' = 6 \rightarrow ^2D_{5/2}, F''' = 7$.

5.2 Efficient sub-Doppler laser cooling

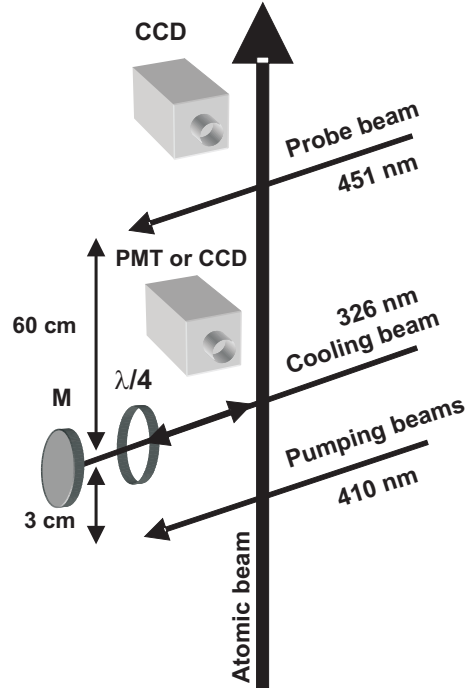


Figure 5.4: Schematic of the experimental setup. The atoms are optically pumped to the $^2P_{3/2}$ levels by two violet lasers at λ_{pump} in the pumping region. In the cooling region, UV light at λ_{cool} is applied with a polarization gradient configuration (lin \perp lin) for laser cooling. The spatial distribution of the atomic flux density is measured by exciting the atoms at λ_{probe} and imaging the fluorescence distribution at λ_{pump} in the probe region.

Atomic fluorescence detection

A photo-multiplier tube in the cooling region detects laser-induced UV fluorescence producing a frequency reference for the cooling laser as shown in Fig. 5.4. In the cooling region, 3 cm above the pumping region, the UV light beams interact at right angles with the atomic beam. A weak magnetic guiding field (2 G) is applied in the direction of the cooling laser beam. Figure 5.5(a) shows a fluorescence spectrum (solid line) along with a Doppler limited absorption spectrum (dotted line) of In in a hollow cathode lamp for comparison. The frequency of the laser is calibrated by the separation between the $6 \rightarrow 5$ and the $6 \rightarrow 7$ transition (1948 MHz). The FWHM of the transition $6 \rightarrow 7$, which serves as a cooling transition, is measured to be 44 MHz. Considering the divergence of the atomic beam (3 mrad, 5 MHz), the power broadening ($s = I/I_{\text{sat}} = 0.7$, 27 MHz), and the spectral linewidth of the laser (10 MHz), the expected FWHM is deduced to be 42 MHz, which is comparable to the measured width. The height of the peak of the $6 \rightarrow 7$ transition is much larger than those of other transitions even though the relative transition strength

of the $6 \rightarrow 7$ transition is not so different as shown in Fig. 5.5(b). This fact indicates that the $6 \rightarrow 7$ transition is a strongly cycling transition which is suitable for the efficient laser cooling. The cooling laser frequency is locked to one side of the fluorescence peak of the cycling transition yielding an appropriate detuning of $\sim -\Gamma$ for cooling and $\sim +\Gamma$ for heating.

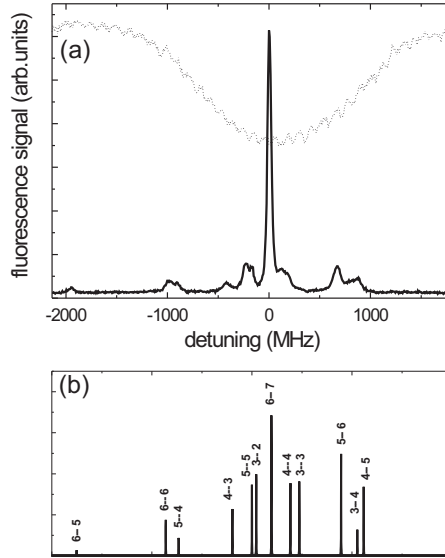


Figure 5.5: (a) Solid line: Fluorescence spectrum of the $\text{In } ^2P_{3/2} \rightarrow ^2D_{5/2}$ transitions induced by the UV laser at λ_{cool} . Dotted line: Doppler limited absorption spectrum of a hollow cathode lamp. The frequency of the laser is calibrated by the separation between the $6 \rightarrow 5$ and the $6 \rightarrow 7$ transitions (1948 MHz). The FWHM of the peak of the $6 \rightarrow 7$ transition is 44 MHz. (b) Theoretical spectrum indicating position and oscillator strengths of hyperfine transitions. In the observed spectrum, optical cycling leads to strong enhancement on the closed $6 \rightarrow 7$ transition.

Optical pumping

In order to enhance the population in the ground state of the cooling transition, the Indium atoms are optically pumped to the $5P_{3/2}$ state by the pump beams at λ_{pump} . For the optical pumping, the atomic Indium beam is irradiated by two violet beams at λ_{pump} whose frequencies are locked to the $4 \rightarrow 5$ (4 mW) and $5 \rightarrow 5$ (2 mW), respectively. The frequency of the cooling beam at λ_{cool} is scanned around the cycling transition, and the enhancement of the amplitude of the fluorescence signal due to the optical pumping is observed by a PMT as shown in Fig. 5.6(a). The amplitude of the fluorescence signal is increased by a factor of 7.4 ($4 \rightarrow 5$, $5 \rightarrow 5$ pumping), 2.9 ($5 \rightarrow 5$ pumping), and 2 ($4 \rightarrow 5$ pumping) with respect to the no-pumping case. When we assume that the

thermal populations of the ground state of the cooling transition is 6.5 % at 1200 °C, the optically pumped population is deduced to be 48.2 %, 18.7 %, 13.15 %. Thus the fraction of the accessible Indium atoms is enhanced up to $\sim 50\%$. Figure 5.6(b) shows the time evolution of the population of $5P_{3/2}, F = 6$ calculated by a rate equation model depending on the pumping scheme. Already for interaction time of 1 μs the evolutions already reach a steady state. The theoretical values in terms of a rate equation model are calculated to be 53 %, 25.9 %, 23.8 % with respect to each pumping scheme. The reasons of the deviation between experiment and theory might be attributed to a formation of dark states in a $F \rightarrow F'$ transition. The detailed investigation of the pumping effect is beyond the scope of the present dissertation.

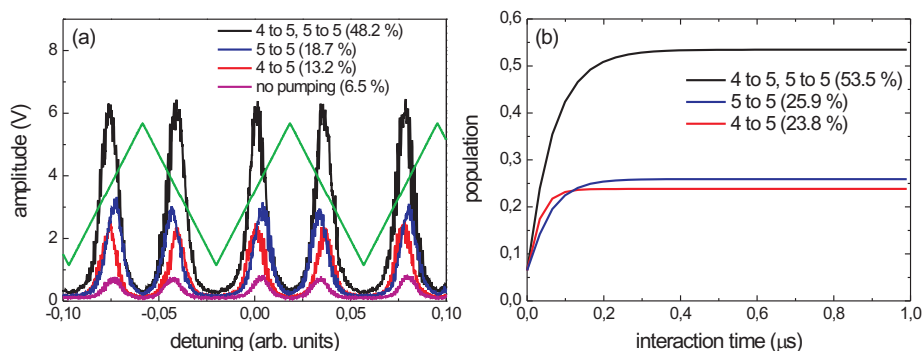


Figure 5.6: (a) Fluorescence peaks of the $6 \rightarrow 7$ transition depending on the optical pumping scheme. The green line is the ramp signal. (b) Time evolution of the population of $5P_{3/2}, F = 6$ with the various pumping scheme.

Atomic beam pushing

In the probe region, 61 cm above the cooling region, the beam pushing effect is investigated to deduce the opto-mechanical parameters, e.g. a scattering rate, and a maximum velocity transfer. The frequency of the cooling laser is set to be resonant with the cooling transition. The interaction time is $\tau_{\text{int}} = 5.4 \mu\text{s} = 700 \tau$. The saturation parameter in the pushing experiment is deduced to be 4.5. The optical pumping beams underneath the cooling beam are shone to the atomic beam to observe a clearer fluorescence image in the probe region. Figure 5.7(a) shows the fluorescence images of an atomic beam in the probe region without and with the pushing beam at λ_{cool} , and their integrated transverse profiles are shown in Fig. 5.7(b). The transverse velocity change can be deduced from the spatial shift of the atomic beam using $\Delta v = v_l \Delta x / l$ in the same way as in Ref. [18]. The displacement of the atomic beam (Δx) due to the resonant pushing effect is measured to be 1.8 mm yielding a velocity change (Δv) of 1.7 m/s ($152 v_r$). The scattering rate can be deduced

from the velocity change,

$$\gamma_c \hbar k = m_{\text{In}} \frac{\Delta v}{\Delta t}, \quad (5.2)$$

where Δt is the interaction time, m_{In} the mass of an Indium atom, and γ_c the scattering rate. The scattering rate is estimated to be 3×10^7 Hz indicating 160 scattering events during the interaction time. For exact investigation, the frequency of the UV laser should

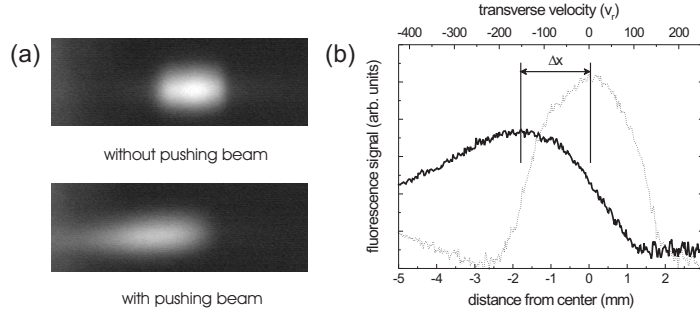


Figure 5.7: The images (a) and integrated transverse profiles (b) of the atomic beam in the probe region with and without the pushing beam at λ_{cool} . The displacement of the atomic beam due to the pushing effect is measured to be 1.8 mm which is corresponding to the transverse velocity change of $152 v_r$.

be locked to the resonance line by means of an appropriate spectroscopy.

Efficient sub-Doppler laser cooling

In order to induce a lin \perp lin polarization gradient in the cooling region a linearly polarized beam is sent to the atomic beam and retro-reflected passing a quarter wave plate twice which induces a 90° rotation of the polarization as shown in Fig. 5.4. The propagation directions of the cooling beams are set at right angles to the atomic beam within 2 mrad uncertainty by overlapping the two fluorescence signals induced by the counter-propagating UV beams.

Efficient sub-Doppler laser cooling caused by polarization gradient cooling [60] for red detuned cooling laser beams as well as heating effects for blue detuned laser beams are observed by flux enhancements and attenuations in the probe region as shown in Fig. 5.8(a). The insets of Fig. 5.8(a) show fluorescence images of the In atomic beam with a striking bright region of cooled atoms (left, red detuned cooling laser), and a dark region caused by the expulsion of heated atoms (right, blue detuned cooling laser).

For further analysis the fluorescence images are integrated along the direction transverse to the propagation direction of the cooling laser. Fig. 5.8 shows the profiles of the laser-cooled (solid line), the uncooled (dotted line), and the heated (dashed line) atomic In beam in the probe region, respectively. Here, the FWHM of the cooled fraction is measured to be 0.2 mm, which is smaller than the nominal initial width of the atomic beam (0.5 mm). This

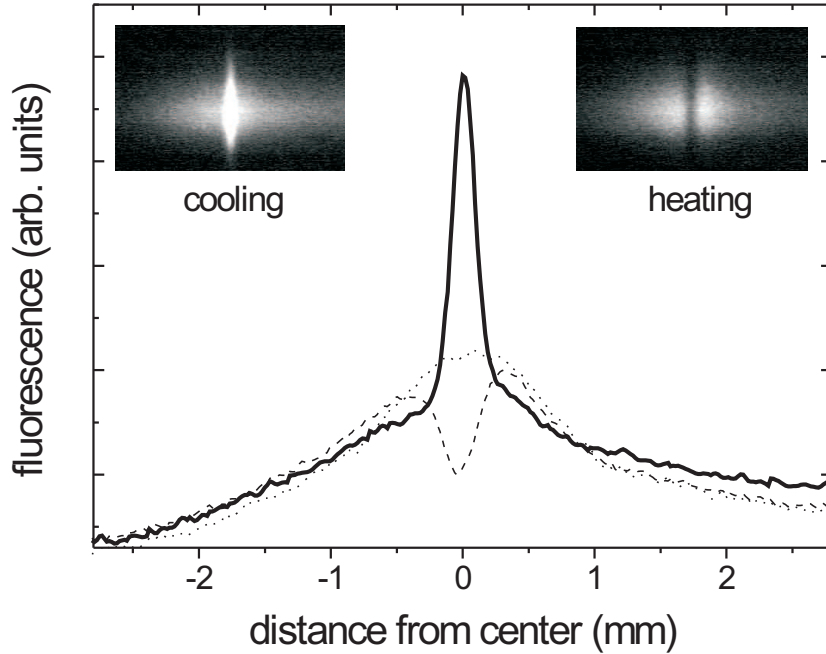


Figure 5.8: Integrated transverse profiles of the atomic beam in the probe region: (solid line) cooling with the lin \perp lin polarization gradient ($\Delta \sim -\Gamma$), (dotted line) no laser cooling, (dashed line) heating with lin \perp lin polarization gradient ($\Delta \sim +\Gamma$). Insets: Images of a cooled (left) and a heated (right) In atomic beam.

could be attributed to the fact that residual In partially clogged the mechanical aperture so that the effective diameter of the aperture was decreased. After cleaning the aperture, the FWHM of the laser-cooled atomic beam was re-measured to be 0.86 ± 0.07 mm yielding the 13.5 ± 3.8 cm/s transverse velocity well below the Doppler limited velocity of 19 cm/s. The corresponding full divergence is 0.48 ± 0.13 mrad.

The fraction of laser-cooled atoms is deduced to be 12 ± 3 %. It is currently limited by the number of effective scattering events which is deduced by analyzing the laser-heated atomic beam profiles because opto-mechanical effects can be better estimated by heating processes rather than cooling processes. The FWHM of the laser-heated atomic beam is measured to be 1.06 ± 0.13 mm. Assuming that atoms with zero transverse velocity are kicked out to the side, the velocity change of the zero velocity group is deduced to be 48.58 ± 0.06 cm/s. Then, an effective scattering rate can be calculated to be $2 \pi \cdot 1.35 \times 10^6$ Hz by means of Eq. (5.2) yielding the number of effective scattering events of 50 during the interaction time.

The asymmetry in the laser-cooled beam profile could be attributed to an imbalance in

the cooling laser power induced by the uncoated vacuum windows. After interaction of the In atoms with the cooling laser, most of the In atoms ($> 99\%$) survive within the cooling transition indicating no significant leakage in the cycling transition.

This result is a significant improvement in terms of cooling efficiency and a fraction of laser-cooled In atoms compared to the previous experiment [18].

5.3 Calculation of the average force by polarization gradient for Indium

In this section, I will give a theoretical description of the polarization gradient cooling on Indium. This calculation is based on a famous paper, Ref. [60]. All formalism in this paper is completely demonstrated by Mathematica program and extended to the $F_g = 6 \rightarrow F_e = 7$ transition in Indium.

In the polarization gradient cooling, two counter-propagating laser fields with orthogonal linear polarizations (\hat{x} , \hat{y}) are shone to the atoms in the z direction as shown in Fig. 5.2 and can be expressed by

$$\begin{aligned} \mathbf{E}(z, t) &= E_0 e^{i\omega t} (\hat{x} e^{ikz} + i\hat{y} e^{-ikz}) + c.c. \\ &= \sqrt{2} E_0 e^{i\omega t} \left[\frac{(\hat{x} + i\hat{y})}{\sqrt{2}} \cos kz + i \frac{(\hat{x} - i\hat{y})}{\sqrt{2}} \sin kz \right] + c.c. \\ &= \sqrt{2} E_0 e^{i\omega t} [\hat{\sigma}_+ \cos kz + i \hat{\sigma}_- \sin kz] + c.c., \end{aligned} \quad (5.3)$$

where ω is the angular frequency of the laser, k is the wave number. As shown in Eq. (5.3) counter-propagating light fields with orthogonal polarization can be converted into σ_+ polarized and σ_- polarized light with different phase. The Rabi frequency for each transition can be expressed by

$$\Omega_{ij} = -2 \frac{dE_0}{\hbar} = 2 \sqrt{\frac{3\lambda^3}{2\pi\hbar c} \gamma_{ij} I} = 2 \sqrt{S_{ij}} \sqrt{\frac{3\lambda^3}{2\pi\hbar c} \gamma I} = 2 \sqrt{S_{ij}} \Omega_0, \quad (5.4)$$

where S_{ij} is the relative transition strength as calculated in Appendix A.

The average force applied to the atom is calculated by taking the spatial gradient of the Hamiltonian in Eq. (2.6) like

$$\begin{aligned} \langle F \rangle &= - \left\langle \frac{d\tilde{H}}{dz} \right\rangle \\ &= - \frac{\hbar k}{\sqrt{2}} \Omega \cos(kz) \sum_{i=-6}^6 \sqrt{S(g_i, e_{i-1})} \rho(g_i, e_{i-1}) \\ &\quad + \frac{\hbar k}{\sqrt{2}} \Omega \sin(kz) \sum_{i=-6}^6 \sqrt{S(g_i, e_{i+1})} \rho(g_i, e_{i+1}), \end{aligned} \quad (5.5)$$

where the state g_i indicates the ground state and e_i the excited state.

To deduce the reactive force, the coherences between the ground and the excited states in Eq. (5.5) should be calculated. Assuming low intensity and low velocity, the coherences between the ground and the excited states and the population of the excited states follow adiabatically the ground state populations. Therefore, the optical force can be expressed in terms of the ground state populations, $\rho(g_i, g_i)$. More specifically the force can be expressed by

$$\langle F(t) \rangle = -\hbar k \delta \Omega^2 \sin(2kvt) \sum_{i=1}^6 A_i(\Gamma, \delta) \Delta \rho(g_{-i}, g_i)(t), \quad (5.6)$$

where z is replaced by vt , $\Delta \rho(g_{-i}, g_i)(t)$ is the population difference between the ground states, and $A_i(\Gamma, \delta)$ are coefficients which have the form

$$A_i(\Gamma, \delta) = \frac{c_1^i \Gamma^2 + c_2^i \delta^2}{c_3^i \Gamma^4 + c_4^i \Gamma^2 \delta^2 + c_5^i \delta^4}. \quad (5.7)$$

Each coefficient (c_j^i) in Eq. (5.7) can be calculated numerically.

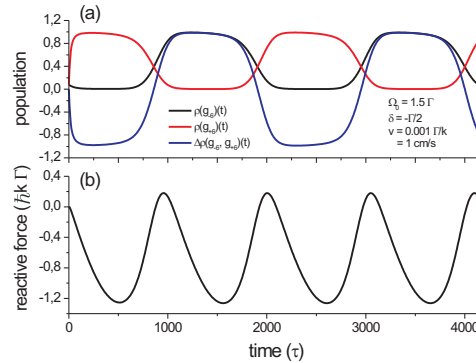


Figure 5.9: (a) The time evolution of the ground state populations, $\rho(g_{-6})(t)$ (black), $\rho(g_6)(t)$ (red), and $\rho(g_{-6})(t) - \rho(g_6)(t) = \Delta \rho(g_{-6}, g_6)(t)$ (blue). (b) The time evolution of the reactive force in the unit of $\hbar k \Gamma$. The parameters used in the calculation are $\Omega_0 = 1.5 \Gamma$ ($s = 4.5$), $\delta = -0.5 \Gamma$. The velocity is selected to be $0.0015 \Gamma/k = 1 \text{ cm/s}$.

By replacing the excited state populations and the coherences with the ground state populations, the time derivatives of the ground state populations can be expressed in terms of the ground state populations, so the time evolution of the optical force can be obtained. Figure 5.9(a) shows the time evolution of the ground state populations, e.g. $\rho(g_{-6})(t)$ (black), $\rho(g_6)(t)$ (red), and $\rho(g_{-6})(t) - \rho(g_6)(t) = \Delta \rho(g_{-6}, g_6)(t)$ (blue) and (b) the time evolution of the reactive force in the unit of $\hbar k \Gamma$ over a wavelength, $z = \lambda = vt$. The parameters used in the calculation are $\Omega_0 = 1.5 \Gamma$ ($s = 4.5$), $\delta = -0.5 \Gamma$. The velocity is selected to be $0.0015 \Gamma/k = 1 \text{ cm/s}$ for this example.

Finally the reactive force can be averaged over a wavelength to deduce the average force. An average force curve for all velocity groups is obtained by averaging the reactive forces

for each velocity group numerically, and the total average force curve is fitted by a simple function including a capture velocity (v_c) and a coefficient (α) like

$$F_{\text{ave}} = -\frac{\alpha v/v_c}{1 + (v/v_c)^2}, \quad \beta = \frac{\alpha}{2v_c} \hbar k^2, \quad (5.8)$$

where β is the friction coefficient.

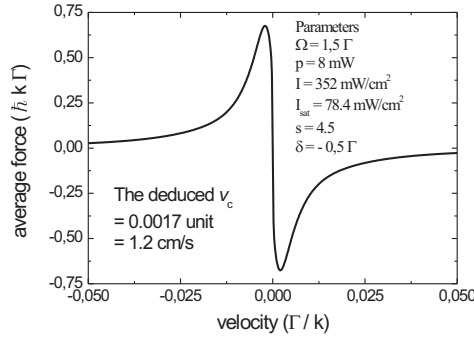


Figure 5.10: The average force for Indium in the lin \perp lin configuration. The parameters used in the calculation are $\Omega_0 = 1.5 \Gamma$ ($s = 4.5$), $\delta = -0.5 \Gamma$.

Figure 5.10 shows the calculated average force as a function of the velocity for the same parameter as in Fig. 5.9. The capture velocity and the friction coefficient are deduced to be $0.002 \Gamma/k$ and $876 \hbar k^2$, respectively. The friction coefficient in the case of the polarization gradient cooling is several orders of magnitude larger than that of the Doppler cooling ($\sim 0.4 \hbar k^2$). The friction coefficient is proportional to the detuning. For the same Rabi frequency β is calculated to be $1980 \hbar k^2$ for a larger detuning of $\delta = -1.5 \Gamma$.

Using the deduced average force, the transverse profile of the Indium atomic beam in the probe region is calculated as shown in Fig. 5.11. In this simulation, the trajectories of 2×10^6 Indium atoms are traced. The FWHM of the cooled and uncooled profiles fitted by two Gaussian functions are obtained to be 0.4 and 2.3 mm, respectively. The fraction of the laser-cooled atoms is 5% which is comparable to the experimental result, 12% .

For higher laser power (50 mW) and longer interaction length ($L_{\text{int}} = 10$ mm) yielding the same intensity as in Fig. 5.11, the fraction of the cooled In atoms can be enhanced as shown in Fig. 5.12. The fraction of the laser-cooled atoms is deduced to be 32% , which is much larger than that of the experiment.

5.4 Conclusions and further improvements

In summary, I have realized an experiment showing efficient sub-Doppler laser cooling of an In atomic beam on a cycling transition. The fraction of In atoms in the ground state of the cycling transition was enhanced by optical pumping. The fraction of laser-cooled In atoms (now $12 \pm 3 \%$) can be further enhanced by increasing the number of scattering

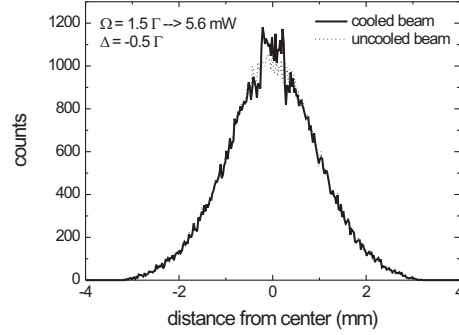


Figure 5.11: The calculated transverse profile of a cooled (black solid line) and an uncooled (red dotted line) Indium atomic beam. The fraction of the laser-cooled atoms is calculated to be 5 %. The parameters used in the calculation are $\Omega_0 = 1.5 \Gamma$ ($s = 4.5$), $\delta = -0.5 \Gamma$ and $L_{\text{int}} = 3$ mm.

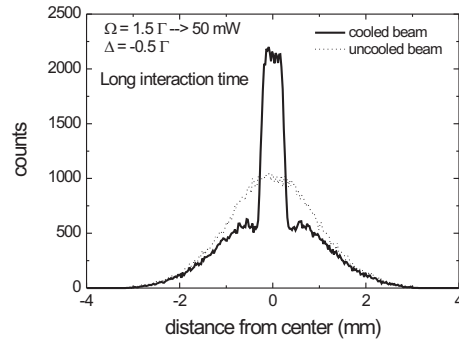


Figure 5.12: The calculated transverse profile of a cooled (black solid line) and an uncooled (red dotted line) Indium atomic beam in the improved case. The fraction of the laser-cooled atoms is calculated to be 32 %. The parameters used in the calculation are $\Omega_0 = 1.5 \Gamma$ ($s = 4.5$), $\delta = -0.5 \Gamma$ and $L_{\text{int}} = 10$ mm.

events, i.e. increasing the interaction length and the cooling laser power in order to extend the velocity range captured by Doppler cooling processes. Realistic improvements include higher UV power (100 mW instead of 7 mW), a longer interaction length (10 mm instead of 3 mm) and additional optical pumping frequencies at λ_{probe} . With these advances one may well approach 100 % efficiency in laser cooling of In atomic beams.

Chapter 6

Summary and outlook

Summary

In this dissertation, I described nonlinear spectroscopy of Indium in high temperature cells, a coherent UV light source based on fiber amplifiers, and transverse laser cooling of an Indium atomic beam which is an important step towards ANF.

In Chapter 3, nonlinear spectroscopy of an open 3-level, Λ -type level system driven by a pump and a probe beam was investigated in order to understand the absorption line shapes used as a frequency reference in the previous two-colour spectroscopy experiment [26]. The theoretical model derived in this chapter was very useful to analyze and explain the features of the observed spectra and I came to the conclusion that the origin of the line width broadening in the two-colour spectroscopy was not velocity changing collisions but strong optical pumping in a 3-level, Λ -type system. The home-made hollow cathode lamp provided an appropriate frequency reference for the blue light at $\lambda = 451$ nm.

In Chapter 4, I presented a continuous-wave coherent ultraviolet source at 326 nm based on frequency tripling for efficient laser cooling on a cycling transition. It was the first time in our group to build fiber-based light sources which could be the next generation of novel light sources in atomic physics laboratories. The technical recipes in building a fiber amplifier are also presented in Appendix C. The unusual wavelength at $\lambda = 326$ nm was successfully synthesized by means of 2nd order nonlinear optical processes in two enhancement cavities.

In Chapter 5, I described sub-Doppler transverse laser cooling of an Indium atomic beam on a cycling transition in the presence of a polarization gradient in the linear-perpendicular-linear configuration. The final transverse velocity achieved is 13.5 ± 3.8 cm/s, well below the Doppler cooling limit. The fraction of the laser-cooled In atoms is obtained to be 12 ± 3 %.

Outlook

Further improvements in the cooling experiment can be achieved by enhancing the power of the cooling laser, additionally pumping Indium atoms using blue light at $\lambda = 451$ nm for

100% pumping efficiency, and appropriately coated optics for UV wavelengths. Recently, a 94 W laser source at $\lambda = 980$ nm based on a large-mode area rod-type double-clad fiber has been developed [63]. This special fiber has an enhanced overlap factor up to 0.18 allowing an efficient pumping. The manufacturer is Crystal-Fibre and its model is DC-200-85-Yb-ROD.

The cooling laser frequency should be stabilized to a cycling transition using a conventional spectroscopy for a well-defined frequency detuning. With such an improved power and a well-defined detuning, more detailed investigation of the cooling process in Indium should be performed as a function of the laser detuning and the laser power.

Next step of the Indium experiment is to focus an Indium atomic beam by means of an atom lens. Ultimately Indium might be co-deposited with other elements, e.g. Al or As producing a fully 3D structured (In,Al)As crystal with periodically modulated In concentration as shown in Fig. 6.1.

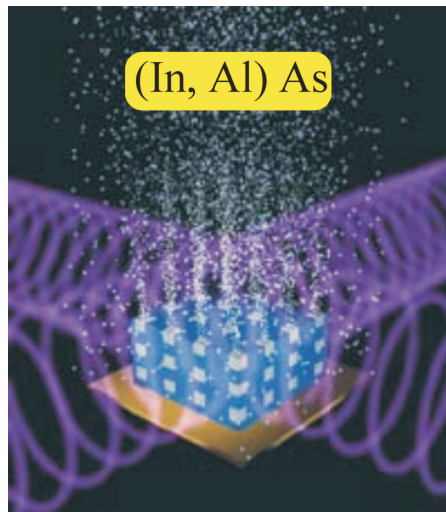


Figure 6.1: Ultimate goal of ANF experiment: Co-deposition of Indium with other elements, e.g. Al or As for structured doping.

Appendix A

Matrix elements

The exact transition probabilities for the Zeeman-, hyperfine- and fine transitions of Indium are essential to estimate the interaction of Indium with light. Let's start with a Zeeman transition and go up from here. The matrix element for a polarization ($q = -1, 0, 1$) is

$$d_{m'_F \rightarrow m_F}^2 = |\langle F, m_F | d_q | F', m_{F'} \rangle|^2$$

Using the Wigner-Eckardt theorem this can be reduced to

$$|\langle F, m_F | d_q | F', m_{F'} \rangle|^2 = \begin{pmatrix} F' & 1 & F \\ -m_{F'} & q & m_F \end{pmatrix}^2 |\langle F || d || F' \rangle|^2 \quad (\text{A.1})$$

where $|\langle F || d || F' \rangle|^2$ is the reduced matrix element which is given by

$$|\langle F || d || F' \rangle|^2 = \left\{ \begin{matrix} J & J' & 1 \\ F' & F & I \end{matrix} \right\}^2 (2F' + 1)(2F + 1) |\langle J || d || J' \rangle|^2 \quad (\text{A.2})$$

So the matrix element can be written as

$$d_{m'_F \rightarrow m_F}^2 = \begin{pmatrix} F' & 1 & F \\ -m_{F'} & q & m_F \end{pmatrix}^2 \left\{ \begin{matrix} J & J' & 1 \\ F' & F & I \end{matrix} \right\}^2 (2F' + 1)(2F + 1) |\langle J || d || J' \rangle|^2 \quad (\text{A.3})$$

After summing the matrix elements for every q and m_F , one can get

$$\begin{aligned} d_{F' \rightarrow F}^2 &= \sum_{q, m_F} d_{m'_F \rightarrow m_F}^2 \\ &= \underbrace{\sum_{q, m_F} \begin{pmatrix} F' & 1 & F \\ -m_{F'} & q & m_F \end{pmatrix}^2}_{\text{Eq. (4.42) in [66]}} \left\{ \begin{matrix} J & J' & 1 \\ F' & F & I \end{matrix} \right\}^2 (2F' + 1)(2F + 1) |\langle J || d || J' \rangle|^2 \\ &= (2F + 1) \left\{ \begin{matrix} J & J' & 1 \\ F' & F & I \end{matrix} \right\}^2 |\langle J || d || J' \rangle|^2 \end{aligned} \quad (\text{A.4})$$

In the Ref. [65], the the decay rate can be expressed by

$$\Gamma_{J' \rightarrow J} = \frac{4}{3} \frac{\alpha}{c^2 e^2} \omega_{J' \rightarrow J}^3 \frac{|\langle J || d || J' \rangle|^2}{2J' + 1}. \quad (\text{A.5})$$

Thus the decay rate of each hyperfine transition can be obtained in terms of $|\langle J || d || J' \rangle|^2$ basis as

$$\begin{aligned} \Gamma_{F' \rightarrow F} &= \frac{4}{3} \frac{\alpha}{c^2 e^2} \omega_{F' \rightarrow F}^3 d_{F' \rightarrow F}^2 \\ &= \left\{ \begin{array}{ccc} J & J' & 1 \\ F' & F & I \end{array} \right\}^2 (2F+1)(2J'+1) \Gamma_{J' \rightarrow J} \end{aligned} \quad (\text{A.6})$$

According to the NIST database (www.physics.nist.gov/cgi-bin/AtData/display.ksh) the natural line widths for the fine transitions are found as

$$\begin{aligned} \Gamma_{J'=1/2 \rightarrow J=1/2} &= \Gamma_{410} = 2 \pi \text{ 8.9 MHz} \\ \Gamma_{J'=1/2 \rightarrow J=3/2} &= \Gamma_{451} = 2 \pi \text{ 16.2 MHz.} \end{aligned} \quad (\text{A.7})$$

451 nm

The $d_{m_F \rightarrow m_{F'}}^2$ is expressed in terms of $|\langle J = \frac{3}{2} || d || J' = \frac{1}{2} \rangle|^2$ for 451 nm and in terms of $|\langle J = \frac{1}{2} || d || J' = \frac{1}{2} \rangle|^2$ for 410 nm.

Table A.1: F=3 to F'=4, π -polarisation

-3 → -3	-2 → -2	-1 → -1	0 → 0	1 → 1	2 → 2	3 → 3
$\frac{7}{144}$	$\frac{1}{12}$	$\frac{5}{48}$	$\frac{1}{9}$	$\frac{5}{48}$	$\frac{1}{12}$	$\frac{7}{144}$

Table A.2: F=3 to F'=4, σ^+ -polarisation

-3 → -2	-2 → -1	-1 → 0	0 → 1	1 → 2	2 → 3	3 → 4
$\frac{7}{144}$	$\frac{1}{12}$	$\frac{5}{48}$	$\frac{1}{9}$	$\frac{5}{48}$	$\frac{1}{12}$	$\frac{7}{144}$

Table A.3: F=4 to F'=4, π -polarisation

-4 → -4	-3 → -3	-2 → -2	-1 → -1	0 → 0	1 → 1	2 → 2	3 → 3	4 → 4
$\frac{11}{75}$	$\frac{33}{400}$	$\frac{11}{300}$	$\frac{11}{1200}$	0	$\frac{11}{1200}$	$\frac{11}{300}$	$\frac{33}{400}$	$\frac{11}{75}$

Table A.4: F=4 to F'=4, σ^+ -polarisation

-4 → -3	-3 → -2	-2 → -1	-1 → 0	0 → 1	1 → 2	2 → 3	3 → 4
$\frac{11}{300}$	$\frac{77}{1200}$	$\frac{33}{400}$	$\frac{11}{120}$	$\frac{11}{120}$	$\frac{33}{400}$	$\frac{77}{1200}$	$\frac{11}{300}$

Table A.5: F=5 to F'=4, π -polarisation

-4 → -4	-3 → -3	-2 → -2	-1 → -1	0 → 0	1 → 1	2 → 2	3 → 3	4 → 4
$\frac{1}{50}$	$\frac{8}{225}$	$\frac{7}{150}$	$\frac{4}{75}$	$\frac{1}{18}$	$\frac{4}{75}$	$\frac{7}{150}$	$\frac{8}{225}$	$\frac{1}{50}$

Table A.6: F=5 to F'=4, σ^+ -polarisation

-5 → -4	-4 → -3	-3 → -2	-2 → -1	-1 → 0	0 → 1	1 → 2	2 → 3	3 → 4
$\frac{1}{10}$	$\frac{2}{25}$	$\frac{14}{225}$	$\frac{7}{150}$	$\frac{1}{30}$	$\frac{1}{45}$	$\frac{1}{75}$	$\frac{1}{150}$	$\frac{1}{450}$

Table A.7: F=4 to F'=5, π -polarisation

$-4 \rightarrow -4$	$-3 \rightarrow -3$	$-2 \rightarrow -2$	$-1 \rightarrow -1$	$0 \rightarrow 0$	$1 \rightarrow 1$	$2 \rightarrow 2$	$3 \rightarrow 3$	$4 \rightarrow 4$
$\frac{3}{275}$	$\frac{16}{825}$	$\frac{7}{275}$	$\frac{8}{275}$	$\frac{1}{33}$	$\frac{8}{275}$	$\frac{7}{275}$	$\frac{16}{825}$	$\frac{3}{275}$

Table A.8: F=4 to F'=5, σ^+ -polarisation

$-4 \rightarrow -3$	$-3 \rightarrow -2$	$-2 \rightarrow -1$	$-1 \rightarrow 0$	$0 \rightarrow 1$	$1 \rightarrow 2$	$2 \rightarrow 3$	$3 \rightarrow 4$	$4 \rightarrow 5$
$\frac{1}{825}$	$\frac{1}{275}$	$\frac{2}{275}$	$\frac{2}{165}$	$\frac{1}{55}$	$\frac{7}{275}$	$\frac{28}{825}$	$\frac{12}{275}$	$\frac{3}{55}$

Table A.9: F=5 to F'=5, π -polarisation

$-5 \rightarrow -5$	$-4 \rightarrow -4$	$-3 \rightarrow -3$	$-2 \rightarrow -2$	$-1 \rightarrow -1$	$0 \rightarrow 0$	$1 \rightarrow 1$	$2 \rightarrow 2$	$3 \rightarrow 3$	$4 \rightarrow 4$	$5 \rightarrow 5$
$\frac{1}{8}$	$\frac{2}{25}$	$\frac{9}{200}$	$\frac{1}{50}$	$\frac{1}{200}$	0	$\frac{1}{200}$	$\frac{1}{50}$	$\frac{9}{200}$	$\frac{2}{25}$	$\frac{1}{8}$

Table A.10: F=5 to F'=5, σ^+ -polarisation

$-5 \rightarrow -4$	$-4 \rightarrow -3$	$-3 \rightarrow -2$	$-2 \rightarrow -1$	$-1 \rightarrow 0$	$0 \rightarrow 1$	$1 \rightarrow 2$	$2 \rightarrow 3$	$3 \rightarrow 4$	$4 \rightarrow 5$
$\frac{1}{40}$	$\frac{9}{200}$	$\frac{3}{50}$	$\frac{7}{100}$	$\frac{3}{40}$	$\frac{3}{40}$	$\frac{7}{100}$	$\frac{3}{50}$	$\frac{9}{200}$	$\frac{1}{40}$

Table A.11: F=6 to F'=5, π -polarisation

$-5 \rightarrow -5$	$-4 \rightarrow -4$	$-3 \rightarrow -3$	$-2 \rightarrow -2$	$-1 \rightarrow -1$	$0 \rightarrow 0$	$1 \rightarrow 1$	$2 \rightarrow 2$	$3 \rightarrow 3$	$4 \rightarrow 4$	$5 \rightarrow 5$
$\frac{1}{24}$	$\frac{5}{66}$	$\frac{9}{88}$	$\frac{4}{33}$	$\frac{35}{264}$	$\frac{3}{22}$	$\frac{35}{264}$	$\frac{4}{33}$	$\frac{9}{88}$	$\frac{5}{66}$	$\frac{1}{24}$

Table A.12: F=6 to F'=5, σ^+ -polarisation

$-6 \rightarrow -5$	$-5 \rightarrow -4$	$-4 \rightarrow -3$	$-3 \rightarrow -2$	$-2 \rightarrow -1$	$-1 \rightarrow 0$	$0 \rightarrow 1$	$1 \rightarrow 2$	$2 \rightarrow 3$	$3 \rightarrow 4$	$4 \rightarrow 5$
$\frac{1}{4}$	$\frac{5}{24}$	$\frac{15}{88}$	$\frac{3}{22}$	$\frac{7}{66}$	$\frac{7}{88}$	$\frac{5}{88}$	$\frac{5}{132}$	$\frac{1}{44}$	$\frac{1}{88}$	$\frac{1}{264}$

410 nm

Table A.13: F=4 to F'=4, π -polarisation

-4 \rightarrow -4	-3 \rightarrow -3	-2 \rightarrow -2	-1 \rightarrow -1	0 \rightarrow 0	1 \rightarrow 1	2 \rightarrow 2	3 \rightarrow 3	4 \rightarrow 4
$\frac{8}{75}$	$\frac{3}{50}$	$\frac{2}{75}$	$\frac{1}{150}$	0	$\frac{1}{150}$	$\frac{2}{75}$	$\frac{3}{50}$	$\frac{8}{75}$

Table A.14: F=4 to F'=4, σ^+ -polarisation

-4 \rightarrow -3	-3 \rightarrow -2	-2 \rightarrow -1	-1 \rightarrow 0	0 \rightarrow 1	1 \rightarrow 2	2 \rightarrow 3	3 \rightarrow 4
$\frac{2}{75}$	$\frac{7}{150}$	$\frac{3}{50}$	$\frac{1}{15}$	$\frac{1}{15}$	$\frac{3}{50}$	$\frac{7}{150}$	$\frac{2}{75}$

Table A.15: F=5 to F'=4, π -polarisation

-4 \rightarrow -4	-3 \rightarrow -3	-2 \rightarrow -2	-1 \rightarrow -1	0 \rightarrow 0	1 \rightarrow 1	2 \rightarrow 2	3 \rightarrow 3	4 \rightarrow 4
$\frac{3}{50}$	$\frac{8}{75}$	$\frac{7}{50}$	$\frac{4}{25}$	$\frac{1}{6}$	$\frac{4}{25}$	$\frac{7}{50}$	$\frac{8}{75}$	$\frac{3}{50}$

Table A.16: F=5 to F'=4, σ^+ -polarisation

-5 \rightarrow -4	-4 \rightarrow -3	-3 \rightarrow -2	-2 \rightarrow -1	-1 \rightarrow 0	0 \rightarrow 1	1 \rightarrow 2	2 \rightarrow 3	3 \rightarrow 4
$\frac{3}{10}$	$\frac{6}{25}$	$\frac{14}{75}$	$\frac{7}{50}$	$\frac{1}{10}$	$\frac{1}{15}$	$\frac{1}{25}$	$\frac{1}{50}$	$\frac{1}{150}$

Table A.17: F=4 to F'=5, π -polarisation

-4 \rightarrow -4	-3 \rightarrow -3	-2 \rightarrow -2	-1 \rightarrow -1	0 \rightarrow 0	1 \rightarrow 1	2 \rightarrow 2	3 \rightarrow 3	4 \rightarrow 4
$\frac{3}{50}$	$\frac{8}{75}$	$\frac{7}{50}$	$\frac{4}{25}$	$\frac{1}{6}$	$\frac{4}{25}$	$\frac{7}{50}$	$\frac{8}{75}$	$\frac{3}{50}$

Table A.18: F=4 to F'=5, σ^+ -polarisation

-4 \rightarrow -3	-3 \rightarrow -2	-2 \rightarrow -1	-1 \rightarrow 0	0 \rightarrow 1	1 \rightarrow 2	2 \rightarrow 3	3 \rightarrow 4	4 \rightarrow 5
$\frac{1}{150}$	$\frac{1}{50}$	$\frac{1}{25}$	$\frac{1}{15}$	$\frac{1}{10}$	$\frac{7}{50}$	$\frac{14}{75}$	$\frac{6}{25}$	$\frac{3}{10}$

Table A.19: F=5 to F'=5, π -polarisation

-5 \rightarrow -5	-4 \rightarrow -4	-3 \rightarrow -3	-2 \rightarrow -2	-1 \rightarrow -1	0 \rightarrow 0	1 \rightarrow 1	2 \rightarrow 2	3 \rightarrow 3	4 \rightarrow 4	5 \rightarrow 5
$\frac{1}{6}$	$\frac{8}{75}$	$\frac{3}{50}$	$\frac{2}{75}$	$\frac{1}{150}$	0	$\frac{1}{150}$	$\frac{2}{75}$	$\frac{3}{50}$	$\frac{8}{75}$	$\frac{1}{6}$

Table A.20: F=5 to F'=5, σ^+ -polarisation

-5 \rightarrow -4	-4 \rightarrow -3	-3 \rightarrow -2	-2 \rightarrow -1	-1 \rightarrow 0	0 \rightarrow 1	1 \rightarrow 2	2 \rightarrow 3	3 \rightarrow 4	4 \rightarrow 5
$\frac{1}{30}$	$\frac{3}{50}$	$\frac{2}{25}$	$\frac{7}{75}$	$\frac{1}{10}$	$\frac{1}{10}$	$\frac{7}{75}$	$\frac{2}{25}$	$\frac{3}{50}$	$\frac{1}{30}$

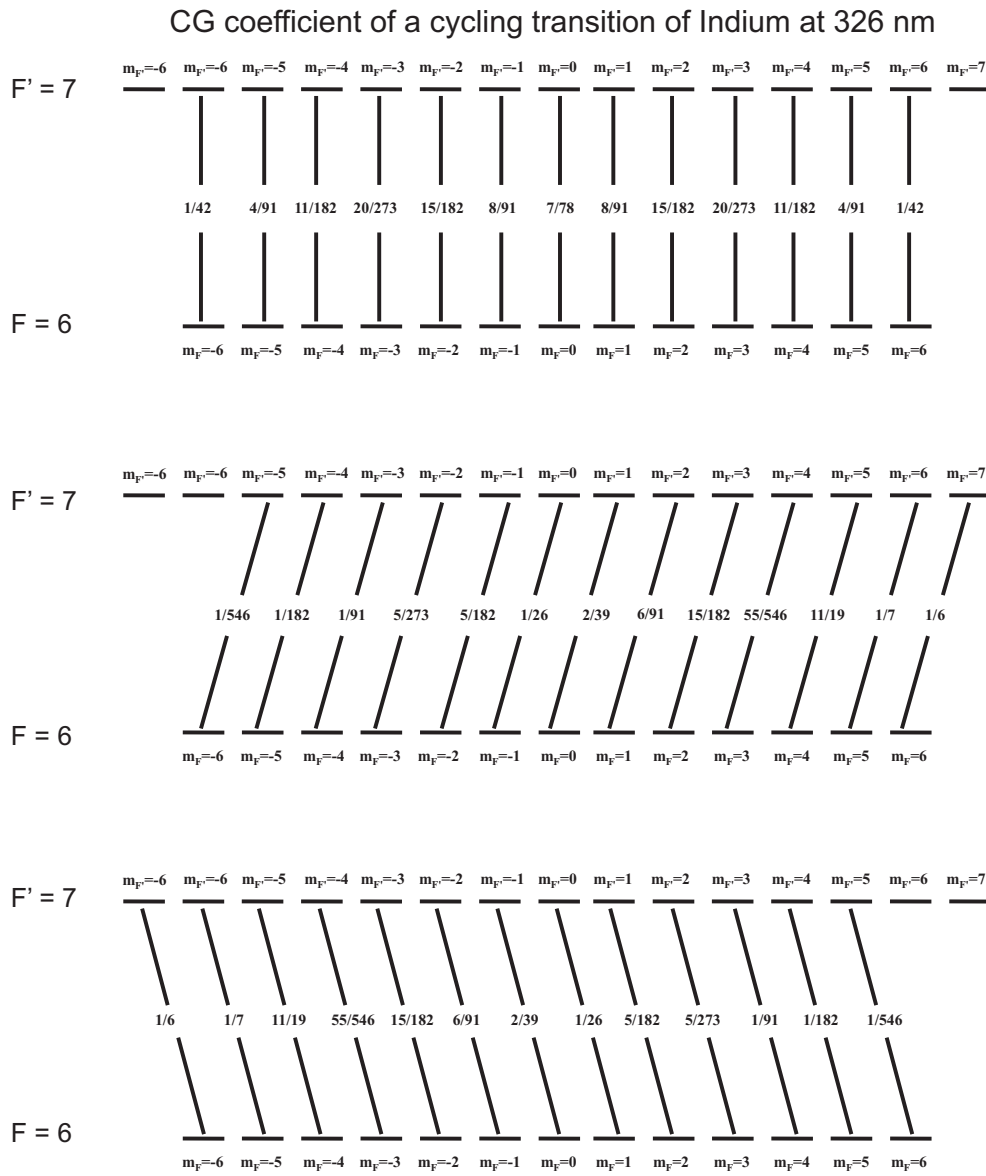


Figure A.1: The Clebsch-Gordan coefficients of a cycling transition of Indium at 326 nm.

Appendix B

Saturation intensity

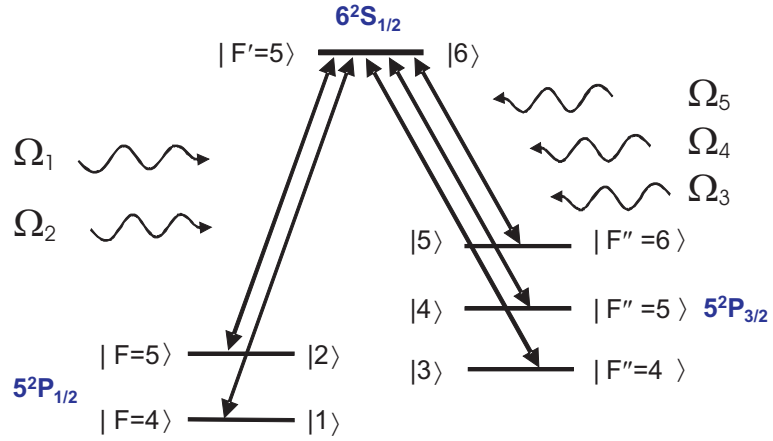


Figure B.1: A multi-level, Λ -type level scheme of ^{115}In for the calculation of saturation intensities.

In this Appendix saturation intensities of a multi-level, Λ -type transition as shown in Fig. B.1, Λ -type transition of In are deduced by a rate equation model [18]. The rate equations for Indium can be written by

$$\dot{N}_6 = \sum_{i=1}^5 R_i(N_i - N_6) - \Gamma N_6, \quad (\text{B.1})$$

$$\dot{N}_i = R_i(N_6 - N_i) + \Gamma_i N_6, \quad (\text{B.2})$$

where R_i is the pumping rate and can be written as

$$R_i = \frac{\Omega_i^2}{\Gamma} \frac{1}{1 + (2\Delta_i/\Gamma)^2}. \quad (\text{B.3})$$

The steady state solution of Eq. (B.1) is easily calculated as

$$N_6^{\text{ss}} = \frac{1}{6} \left(1 + \sum_{i=1}^5 \frac{\Gamma_i}{\Gamma \cdot s_i} \right)^{-1}, \quad (\text{B.4})$$

$$s_i = \frac{6\Omega_i^2}{\Gamma^2} \frac{1}{1 + (2\Delta_i/\Gamma)^2} = \frac{s_{0i}}{1 + (2\Delta_i/\Gamma)^2} \quad (\text{B.5})$$

where s_i is the saturation parameter. The saturation intensity, I_{sat} , is defined such that when $I = I_{\text{sat}}$, the population of the excited state will reach half of the maximum value. In the case of Indium, the maximum population of the excited state is $1/6$ not $1/2$. Figure B.2 shows the population of the excited state as a function of the saturation intensity for a two level system (black) and for Indium (red), respectively. One can see that the Indium system is rapidly saturated compared to a two level system. The gray dots designate the saturation points in each system.

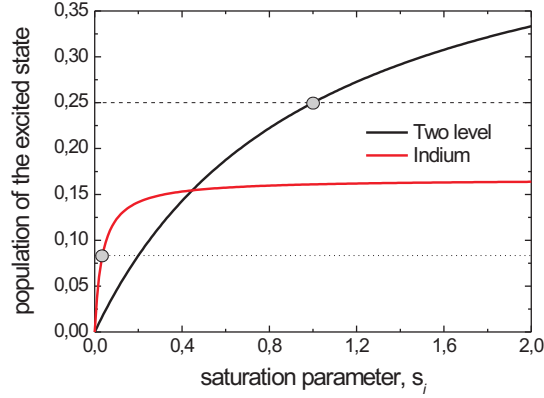


Figure B.2: The population of the excited state as a function of the saturation intensity for a two level system (black) and for Indium (red), respectively.

Let's deduce the saturation intensity of $5P_{1/2}, F = 4 \rightarrow 6S_{1/2}, F' = 5$ transition. From the definition of I_{sat} , one can find

$$N_6^{\text{ss}} = \frac{1}{6} \times \frac{1}{2} \approx \frac{1}{6} \left(1 + \frac{\Gamma_1}{\Gamma s_{01}} \right)^{-1}, \quad (\text{B.6})$$

$$s_{01} = \frac{\Gamma_1}{\Gamma} = \frac{6\Omega_1^2}{\Gamma^2}.$$

Using the fact that $\Omega_1^2 = \frac{3\lambda^3}{2\pi\hbar c} \Gamma_1 I_1$, the final form of the saturation intensity is given by

$$I_{\text{sat}}^1 = \frac{\pi\hbar c}{9\lambda^2} \times \Gamma = 15.9 \text{ mW/cm}^2 = I_{\text{sat}}^{410}. \quad (\text{B.7})$$

The interesting point is that the saturation parameter is not dependent on the decay rate of the individual transition but on the total decay rate, Γ . In the same way, the saturation parameter of blue transitions can be calculated to be $I_{\text{sat}}^{451} = 11.9 \text{ mW/cm}^2$.

Appendix C

Building a fiber amplifier

In this Appendix, I summarize relevant technical tips in building the fiber amplifier. Figure C.1 shows a schematic of a fiber amplifier. I address the important aspects component by component in the system.

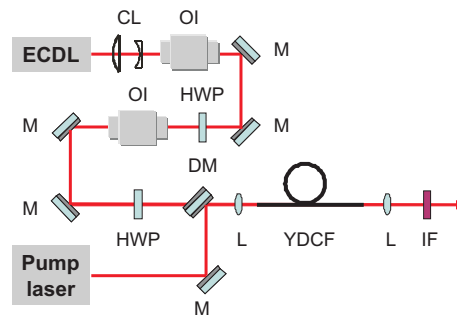


Figure C.1: A schematic of a fiber amplifier.

Seed laser

The purpose of a fiber amplifier is to enhance the power of a seed laser by means of a gain medium, i.e. a rare-earth doped fiber. In an atomic physics lab, an external cavity diode laser (ECDL) is commonly used, so this is a good seed laser in terms of cost, robustness, and easiness of handling.

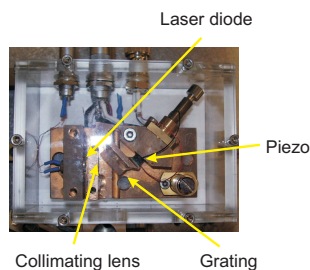


Figure C.2: A picture of the ECDL for the seed beam at λ_ω .

Pump laser

By means of modern semiconductor technology, high power diode lasers (few hundred Watts) are easily available. Usually high power light is guided by a multi-mode fiber. For pumping purpose, the linewidth of the pump laser is not so critical because the absorption bands for pumping Yb^{3+} are broad. The typical line width of these high power diode lasers is around 5 nm.

Coupling lens

A lens is required to couple the pump and seed beams into a rare-earth doped fiber. For this purpose, a typical collimating lens for diode lasers can be used. It is cheap, and easily available from several companies, e.g. Thorlabs, Newport. One can choose an appropriate lens considering the numerical aperture of the inner cladding for a pump beam and that of the core for the seed beam.

Mechanical mount for fiber

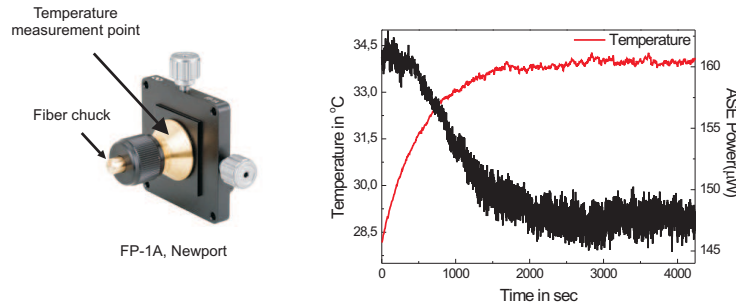


Figure C.3: (a) A fiber holder under the test. The temperature near the fiber chuck is measured. (b) The temperature of a fiber holder as a function of time. The fiber chuck is heated up to more than 35 °C.

To fix a rare-earth doped fiber, a mechanical mount should be appropriately chosen. I have tested two mounts. One is a cheap fiber mount (FP-1A, Newport), the other one is a precision fiber mount (MBT612, Thorlabs). Firstly, FP-1A model is tested. The fiber amplifier is operated in the ASE mode. Due to the high pump power, a fiber chuck is rapidly heated so that a sudden displacement of the fiber mount can occur. Then the high pump power beam is focused on the jacket of the fiber not on the inner cladding and the fiber is burned. In fact, I have frequently observed a flame due to the burning of the fiber. I have measured the temperature near the fiber chuck in the operation of the fiber amplifier as shown in Fig. C.3. It is very hard to precisely compensate the thermal displacement by hand in the FP-1A model. Instead, a precision fiber holder (MBT612, Thorlabs) provides fine control of the fiber position. This type of precision holder is strongly recommended.

Fiber coiling

For efficient pumping of the core, the fiber should be coiled properly. In the cylindrical cladding structure, there always exists a helical ray which can never be overlapped with the core. To overcome this problem, one can coil the fiber in a kidney shape, or a special fiber with unsymmetric inner cladding, e.g. rectangular-shape, can be used to break the symmetry in the pump guide cladding as shown in Fig. C.4(a) and (b), respectively.

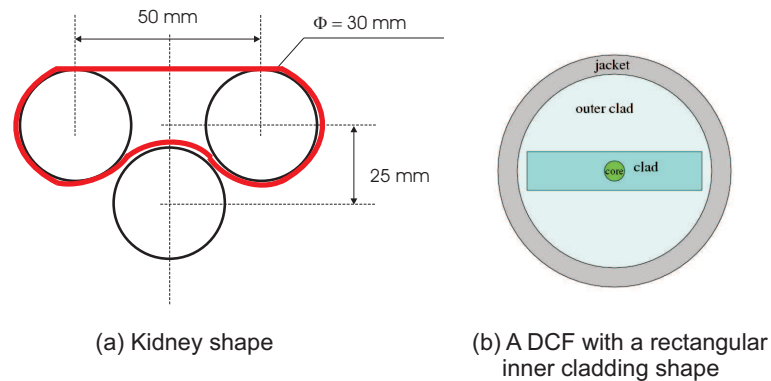


Figure C.4: (a) A kidney shape for coiling a double cladding fiber. The thick red line represents the coiled fiber. (b) A special fiber with the rectangular-shape inner cladding.

Other points

The seed laser is very sensitive to optical feedback. When I use only one 60 dB optical isolator, I have observed optical feedback. The optical feedback was removed by placing another optical isolator. The gain fiber must be angle-cut. In a perpendicular-cut DCF, a part of the light travels back and forth in the fiber to form a resonant mode. One can easily observe this resonant mode using a Fabry-Perot interferometer.

Bibliography

- [1] O. Stern, *Der Weg zur experimentellen Prüfung der Richtungsquantelung im Magnetfeld*, Z. Phy **7**, 249 (1921)
- [2] W. Gerlach and O. Stern, *Der experimentelle Nachweis des magnetischen Moments des Silberatoms*, Z. Phy **8**, 110 (1921)
- [3] O. Frisch, *Experimenteller Nachweis des Einsteinschen Strahlungsrückstoßes*, Z. Physik **86**, 42 (1933)
- [4] T. W. Hänsch and A. Schawlow, *Cooling of gases by laser radiation*, Opt. Commun. **13**, 68 (1975).
- [5] E. L. Raab, M. Prentiss, A. Cable, S. Chu, and D. E. Pritchard, *Trapping of neutral Sodium atoms with radiation pressure*, Phys. Rev. Lett. **59**, 2631 (1987).
- [6] P. D. Lett, R. N. Watts, C. I. Westbrook, W. D. Phillips, P. L. Gould, and H. J. Metcalf, *Observation of atoms laser cooled below the Doppler limit*, Phys. Rev. Lett. **61**, 169 (1988).
- [7] D. Meschede and H. Metcalf, *Atomic nanofabrication: atomic deposition and lithography by laser and magnetic forces*, J. Phys. D **36**, R17 (2003).
- [8] M. Mützel, S. Tandler, D. Haubrich, D. Meschede, K. Peithmann, M. Flaspöhler, and K. Buse, *Atom lithography with a holographic light mask*, Phys. Rev. Lett. **88**, 83601 (2002).
- [9] G. Timp, R. E. Behringer, D. M. Tennant, J. E. Cunningham, M. Prentiss, and K. K. Berggren, *Using light as a lens for submicron, neutral atom lithography*, Phys. Rev. Lett. **69**, 1636 (1992)
- [10] F. Lison, H. J. Adams, D. Haubrich, M. Kreis, S. Nowak and D. Meschede, *Nanoscale atomic lithography with a cesium atom beam*, Appl. Phys. B: Lasers Opt. **65**, 419 (1997)
- [11] J.J. McClelland, R.E. Scholten, E.C. Palm, and R.J. Celotta, *Laser-focused atomic deposition*, Science **262**, 877 (1993)

-
- [12] U. Drodofsky, J. Stuhler, Th. Schulze, M. Drewsen, B. Brezger, T. Pfau, and J. Mlynek, *Hexagonal nanostructures generated by light masks for neutral atoms*, Appl. Phys. B **65**, 755 (1997)
- [13] R. Ohmukai, S. Urabe, M. Watanabe, *Atom lithography with ytterbium beam*, Appl. Phys. B **77**, 415 (2003)
- [14] E. Sligte, B. Smeets, K. M. R. van der Stam, R. W. Herfst, P. van der Straten, H. C. W. Beijerinck, and K. A. H. van Leeuwen, *Atom lithography of Fe*, Appl. Phys. Lett. **85**, 4493 (2004)
- [15] Th. Schulze, T. Mütter, D. Jürgens, B. Brezger, M. K. Oberthaler, T. Pfau, and J. Mlynek, *Structured doping with light forces*, Appl. Phys. Lett. **78**, 1781 (2001).
- [16] R. W. McGowan, D. M. Giltner, and S. A. Lee, *Light force cooling, focusing, and nanometer-scale deposition of aluminum atoms*, Opt. Lett. **20**, 2535 (1995).
- [17] S. J. Rehse, K. M. Bockel, and S. A. Lee, *Laser collimation of an atomic gallium beam*, Phys. Rev. A **69**, 063404 (2004).
- [18] B. Klöter, C. Weber, D. Haubrich, D. Meschede, and H. Metcalf, *Laser cooling of an Indium atomic beam enabled by magnetic fields*, Phys. Rev. A **77**, 033402 (2008).
- [19] S. Padua, C. Xie, R. Gupta, H. Batelaan, and H. Metcalf, *Transient laser cooling*, Phys. Rev. Lett. **70**, 3217 (1993).
- [20] A. Nesmeyanov, *Vapor pressure of the chemical elements*, Elsevier Publishing Company, Amsterdam (1963)
- [21] M. O. Scully and M. S. Zubairy, *Quantum Optics*, Cambridge University Press (1997)
- [22] S. E. Sklarz and D. J. Jannor, and N. Khaneja, Phys. Rev. A **69**, 053408(2004)
- [23] D. Budker, D. F. Kimball, and D. P. DeMille, *Atomic physics: an exploration through problems and solutions*, Oxford University Press (2004)
- [24] V. Wong, R. W. Boyd, C. R. Stroud, Jr., R. S. Bennink, D. L. Aronstein, and Q. H. Park, Phys. Rev. A **65**, 013810 (2001)
- [25] D. Sarkisyan, U. Hinze, L. Meyer, and B. Wellegehausen, Appl. Phys. B **70**, 351 (2000)
- [26] U. Rasbach, J. Wang, R. dela Torre, V. Leung, B. Klöter, D. Meschede, T. Varzhapetyan, and D. Sarkisyan, *One- and Two-Color Spectroscopy on an Indium All-Sapphire Cell*, Phys. Rev. A **70**, 33810, (2004)
- [27] P. R. Berman, P. F. Liao, and J. E. Bjorkholm, *Theory of saturation spectroscopy including collision effects*, Phys. Rev. A **20**, 2389 (1979)

- [28] P. R. Berman, in *Trends in Atomic Physics*, edited by R. Stora (1982)
- [29] S. Stenholm, *Foundation of Laser Spectroscopy* (John Wiley and Sons, 1984)
- [30] P. R. Berman, in *Advances in Atomic and Molecular*, edited by D. R. Bates and B. Bederson (Academic, New York, 1977), Vol. 13, p. 57.
- [31] Y. Q. Li and M. Xiao, *Electromagnetically induced transparency in a three-level Λ -type system in rubidium atoms*, Phys. Rev. A **51**, R2703 (1995)
- [32] J. I. Kim, C. Y. Park, J. Y. Yeom, E. B. Kim, and T. H. Yoon, *Frequency-stabilized high-power violet laser diode with an ytterbium hollow-cathode lamp*, Opt. Lett. **28**, 245 (2003)
- [33] C. Y. Park and T. H. Yoon, *Frequency stabilization of injection-locked violet laser diode with Doppler-free absorption signal of Ytterbium*, Jpn. J. Appl. Phys. **42**, L754 (2003)
- [34] B. Smeets, R. C. M. Bosch, P. van der Straten, E. te Sligte, R. E. Scholten, H. C. W. Beijerinck, and K. A. H. van Leeuwen, *Laser frequency stabilization using an Fe-Ar hollow cathode discharge cell*, Appl. Phys. B **76**, 815 (2003)
- [35] O. M. Maragò, B. Fazio, P. G. Gucciardi, and E. Arimondo, *Atomic gallium laser spectroscopy with violet/blue diode lasers*, Appl. Phys. B **77**, 809 (2003)
- [36] E. Snitzer, *Optical maser action of Nd^{+3} in a barium crown glass*, Phys. Rev. Lett. **7**, 444 (1961)
- [37] S. B. Poole, L. Reekie, R. J. Mears, and D. N. Payne, *Neodymium doped silica single-mode fiber laser*, Electron. Lett. **21**, 738 (1985)
- [38] Y. Jeong, J. K. Sahu, D. N. Payne, and J. Nilsson, *Ytterbium-doped large-core fiber laser with 1.36 kW continuous-wave output power*, Opt. Express **12**, 6088 (2004)
- [39] H. M. Pask, R. J. Carman, D. C. Hanna, A. C. Tropper, C. J. MacKechnie, P. R. Barber, and J. M. Dawes, *Ytterbium-doped silica fiber lasers - versatile sources for the 1 - 1.2 μ m region*, IEEE J. Sel. Top. Quantum Electron., **1**, 2 (1995)
- [40] R. Paschotta, J. Nilsson, A. C. Tropper, and D. C. Hanna, *Ytterbium-doped fiber amplifiers*, IEEE J. Quantum Electron., **33**, 1049 (1997)
- [41] J. Nilsson, J. D. Minelly, R. Paschotta, A. C. Tropper, and D. C. Hanna, *Ring-doped cladding-pumped single mode three-level fiber laser*, Opt. Lett. **23**, 355 (1997)
- [42] A. Bertoni and G. C. Reali, *A model for the optimization of double-clad fiber laser operation*, Appl. Phys. B, **66**, 547 (1998)
- [43] R. Selvas, J. K. Sahu, L. B. Fu, J. N. Jang, J. Nilsson, A. B. Grudinin, K. H. Ylä-Jarkko, S. A. Alam, P. W. Turner, and J. Moore, *High-power, low-noise, Yb-doped, cladding-pumped, three-level fiber sources at 980 nm*, Opt. Lett. **28**, 1093 (2003)

-
- [44] S. Jetschke, S. Unger, U. Röpke, and J. Kirchhof, *Photodarkening in Yb doped fibers: experimental evidence of equilibrium states depending on the pump power*, Opt. Express. **15**, 14838 (2007)
- [45] C. Barnard, P. Myslinski, J. Chrostowski, and M. Kavehrad, *Analytical model for rare-earth-doped fiber amplifiers and lasers*, IEEE J. Quantum Electron., **30**, 1817 (1994)
- [46] K. Schorstein, *Design und Aufbau eines Faserverstärkers*, Diplomarbeit, Fachbereich Physik der TU Darmstadt (2004)
- [47] J. I. Kim and D. Meschede, *Continuous-wave coherent ultraviolet source at 326 nm based on frequency tripling of fiber amplifiers*, Opt. Express. **16**, 10803 (2008)
- [48] G. D. Boyd and D. A. Kleinman, *Parametric interaction of focused Gaussian light beams*, J. Appl. Phys. **39**, 3597 (1968).
- [49] J. Friebe, *Effiziente Erzeugung von ultraviolettem Licht mit neuartigen Kristallstrukturen*, Diplomarbeit, Fachbereich Physik der Universität Hannover (2005)
- [50] J.-J. Zondy, *Type-II frequency doubling at $\lambda = 1.30 \mu\text{m}$ and $\lambda = 2.53 \mu\text{m}$ in flux-grown potassium titanyl phosphate*, J. Opt. Soc. Am. B **11**, 10 (1994).
- [51] A. E. Siegman, *Lasers*, University science books, Mill Valley, California (1986).
- [52] J. Hald, *Second harmonic generation in an external ring cavity with a Brewster-cut nonlinear crystal: theoretical considerations*, Opt. Commun. **197**, 169 (2001).
- [53] T. W. Hänsch and B. Couillaud, *Laser frequency stabilization by polarization spectroscopy of a reflecting reference cavity*, Opt. Commun. **35**, 441 (1980).
- [54] E. S. Polzik and H. J. Kimble, *Frequency doubling with KNbO_3 in an external cavity*, Opt. Lett. **16**, 1400 (1991).
- [55] Y. Kaneda, and S. Kubota, *Theoretical treatment, simulation, and experiments of doubly resonant sum-frequency mixing in an external resonator*, Appl. Opt. **36**, 7766 (1997).
- [56] S. Sayama and M. Ohtsu, *Tunable UV CW generation by frequency tripling of a Ti:sapphire laser*, Opt. Commun. **137**, 295 (1997).
- [57] J. Mes, E. J. van Duijn, R. Zinkstok, S. Witte, and W. Hogervorst, *Third-harmonic generation of a continuous-wave Ti:Sapphire laser in external resonant cavities*, Appl. Phys. Lett. **82**, 4423 (2003).
- [58] C. Weber, *Ein lasergekühlter Atomstrahl zur atomaren Nanostrukturierung*, Diplomarbeit, Mathematisch-Naturwissenschaftliche Fakultät der Rheinischen Friedrich-Wilhelms-Universität Bonn (2005)

-
- [59] H. Metcalf and P. van der Straten, *Laser Cooling and Trapping*, Springer, New York (1999)
- [60] J. Dalibard and C. Cohen-Tannoudji, *Laser Cooling below the Doppler limit by polarization gradients: simple theoretical models*, J. Opt. Soc. Am. B **6**, 2023 (1989)
- [61] S. Stenholm, *The semiclassical theory of laser cooling*, Rev. Mod. Phys. **58**, 699 (1986)
- [62] J. I. Kim, D. Haubrich, and D. Meschede, *Transverse laser cooling of an Indium atomic beam*, in preparation (2009)
- [63] F. Röser, C. Jauregui, J. Limpert, and A. Tünnermann, *94 W 980 nm high brightness Yb-doped fiber*, Opt. Express. **16**, 17310 (2008)
- [64] H. Metcalf and P. van der Straten, *Laser Cooling and Trapping*, Springer, New York (1999)
- [65] R. J. Rafac, C. E. Tanner, A. E. Livingston, and K. W. Kukla, *Precision lifetime measurements of the $6p\ ^2P_{1/2,3/2}$ states in atomic cesium.*, Phys. Rev. A, **50**, R1976 (1994).
- [66] Igor I Sobelman, *Atomic Spectra and Radiative Transitions*, Springer Series on Atoms and Plasmas 12. Springer Verlag, 2 edition (1996)

Acknowledgment

First of all, I would like to thank to Prof. Dr. Dieter Meschede for allowing me a great opportunity to pursue the Ph. D at a unique Bonner Indium Laboratory in the world. Without your great patience and careful considerations my promotion must not be able to be successfully accomplished. For five years, you have told me “*Catch me if you can*”, and I have done my best to catch you for discussions. And special thanks should be extended to Prof. Dr. Karl Maier, Prof. Dr. Hans Kroha, and Prof. Dr. Moritz Sokolowski for accepting the request as referees of my thesis.

Indium has been finally laser-cooled since a decade. Especially I would like to thank Dr. Dietmar Haubrich for all his invaluable advices and guidings for the experiments. Without your support, I could never observe laser-cooled Indium atoms, and thank for so-called “*Dietmar Physics*”. Also I would like to share such a great joy with all former Indium crews and thank to them for all their former achievements. For Claudia Weber, a previous Indium crew, thank you for discussions on the experiment as well as life, and for editing a part of my thesis. For Dr. Ulrich Rasbach, Dr. Jiayu Wang, Dr. Ruby dela Torre, Dr. Bernhard Klöter, thank all of you for your previous contributions.

I extend my appreciations to nice Postdocs in our group. For Dr. Jai-Min Choi, thank you for the all discussions on physics and life. Frequent coffee time has been very helpful to get intuitions of physics. For Dr. Lingbo Kong, thank you for kind discussions on life and physics. For Dr. Wolfgang Alt and Dr. Arthur Widera, thank both of you for fruitful discussions and counsel for my future career. I thank to all administration staffs, e.g. Annelise and Fien.

Special thanks goes to Prof. Tai-Hyun Yoon at Korea University. Your enthusiasm for research has always encouraged me to pursue independently the experiment in Center for Optical Frequency Control providing me a motivative power to start Ph. D in Bonn. I appreciate Prof. Kyuman Cho in Sogang University, Prof. C. S. Jung and other professors in Chongju University for educating me well.

I would like to thank peoples in Bonn Church Community, e.g. Pastor Jongwon Choi and other precious peoples for their religious encouragement enabling me to overcome depression in German life. In addition to Bonn Church Community, I appreciate invaluable financial support from Miadong Methodist Church.

I would like to sincerely thank my parent, Jung-Bong Kim and Byung-Ryul An, for their everlasting support and trust to me. Thank you for giving my birth. I would like to thank my father- and mother-in-law for their support.

Finally, with my whole heart I am grateful to my wife, Seung-Hee Jang, for her eternal love, support and trust to me. I love you.